

PONTIFICIA UNIVERSIDAD CATÓLICA DEL PERÚ

FACULTAD DE CIENCIAS E INGENIERÍA



**Morphological and tribological evaluation of the use of Ti_2AlC
and Ti_3AlC_2 MAX Phases as a surgical AISI 304 stainless steel
coating for a future hip replacement femoral head coating**

Tesis para obtener el título profesional de Ingeniera Biomédica

AUTORA

Gianella Alexandra Ccama Castro

ASESOR

Dr.-Ing. Rolf Grieseler

Lima, Diciembre, 2023

Informe de Similitud

Yo, Prof. Dr.-Ing. Rolf Grieseler, docente de la Facultad de Ciencias e Ingeniería de la Pontificia Universidad Católica del Perú, asesor(a) de la tesis/el trabajo de investigación titulado

Morphological and tribological evaluation of the use of Ti_2AlC and Ti_3AlC_2 MAX Phases as a surgical AISI 304 stainless steel coating for a future hip replacement femoral head coating


de la autora):

Gianella Alexandra Ccama Castro

El mencionado documento tiene un índice de puntuación de similitud de 14%. Así lo consigna el reporte de similitud emitido por el software *Turnitin* el 22/11/2023.

- He revisado con detalle dicho reporte y la Tesis o Trabajo de Suficiencia Profesional, y no se advierte indicios de plagio.
- Las citas a otros autores y sus respectivas referencias cumplen con las pautas académicas.

Lugar y fecha: Lima, 22/11/2023

Apellidos y nombres del asesor <u>Grieseler, Rolf</u>	
CE: 001660902	Firma 
ORCID: 0000-0001-5307-7755	

Resumen

La cadera es una de las articulaciones esféricas más conocidas, y está formada por la cabeza del fémur asentada en la pelvis (acetábulo). En las últimas dos décadas, el reemplazo total de cadera (RTC o THR en inglés) ha sido una intervención quirúrgica de gran éxito. Lamentablemente, el Perú no cuenta con un registro nacional como el de la Academia Americana de Cirujanos Ortopédicos. Sin embargo, en base a los registros de los 5 años anteriores al 2020, se reporta un ingreso anual promedio de entre 20-70 pacientes por hospital de nivel II-2 o III-1. La revisión del implante de la articulación de la cadera indica el fin de la cirugía de sustitución con éxito y anuncia una reaparición de los síntomas que, con frecuencia, superan con creces los de la afección inicial. Los principales motivos registrados fueron: infección e inflamación (20,1%), inestabilidad (18,3%), aflojamiento aséptico (15,9%), complicaciones mecánicas (14,9%), entre otras.

En este contexto, la biotribología estudia las interacciones de las superficies en contacto bajo movimiento relativo en sistemas biológicos. Para reducir la pérdida de material, se puede aplicar una capa de lubricante que evite el contacto directo. Debido al aumento de pacientes menores de 30 años, que requieren implantes que no limiten sus actividades y duren más de 10 años, se sigue investigando en nuevos recubrimientos de implantes metálicos o cerámicos seguros bajo las evaluaciones de comportamiento tribológico y corrosivo para reducir la posibilidad de una revisión a corto plazo que retrase la rehabilitación del paciente. En este contexto, esta tesis presenta una alternativa para los lubricantes sólidos como recubrimientos en la cabeza femoral de los implantes de cadera.

Esta tesis tiene dos objetivos principales. En primer lugar, es una revisión de los avances actuales en la tecnología de recubrimientos para mejoras tribológicas en materiales de prótesis de cadera. Para ello, se revisan los resultados obtenidos en diferentes tribómetros. En segundo lugar, se presenta el primer intento con éxito de crear un recubrimiento de Ti_2AlC y Ti_3AlC_2 sobre un sustrato de acero inoxidable. La caracterización estructural y morfológica de estos recubrimientos se realizó mediante técnicas como la microscopía electrónica de barrido, la difracción

de rayos X y la espectroscopia Raman. Los resultados evidencian una formación significativa de fases MAX sobre un sustrato de acero inoxidable AISI 304 con una barrera de difusión de Si_xN_y .

Estas muestras se probaron posteriormente con un tribómetro "bola sobre plano" para estudiar si el coeficiente de fricción (COF) se veía afectado. Las 6 configuraciones trabajadas fueron una combinación de 3 fuerzas (0.16 N, 0.8 N y 1.6 N) con 2 velocidades (2 mms^{-1} y 10 mms^{-1}) contra una bola de 4 mm de diámetro de AISI 52100 durante 15 minutos. Los resultados fueron prometedores, ya que en todas las condiciones probadas, el Ti_3AlC_2 tenía un COF en torno a 0,13. El revestimiento de Ti_2AlC sobre AISI 304 presentaba valores similares al AISI 304 sin revestimiento a altas fuerzas (COF entre 0.7 y 0.75), pero al aumentar la velocidad y, por tanto, el recorrido, el Ti_2AlC tenía un COF más estable en torno a 0,72 para todas las fuerzas. En general, el COF se vió reducido a largo plazo en las muestras con recubrimientos de Ti_2AlC y Ti_3AlC_2 , en comparación al AISI 304 sin recubrimiento.

Para la caracterización de las huellas dejadas tras la prueba tribológica, se utilizó SEM-EDX para un escaneo lineal de la composición de una sección transversal de huellas y un análisis puntual de puntos alrededor del borde de la huella (donde la bola cambia de dirección). También se utilizó la espectroscopia Raman para caracterizar los subproductos alrededor de las pistas con mayores fuerzas aplicadas (1.6 N). El Ti_2AlC tenía marcas visibles y un alto desgaste del revestimiento, con la única excepción de la pista a 2 mms^{-1} y 0,16 N. El Ti_3AlC_2 tenía las marcas menos visibles, y solo a baja velocidad y alta fuerza (2 mms^{-1} y 1,6 N) había desgaste del revestimiento. En general, la mayoría de los restos en los resultados del análisis elemental provenían de la bola homóloga de AISI 52100.

En conclusión, se obtuvieron resultados prometedores en la reducción de los valores de COF de los recubrimientos de Ti_2AlC y Ti_3AlC_2 . Especialmente de Ti_3AlC_2 , ya que tuvo la menor formación de partículas y desgaste de recubrimiento con un COF inferior a los materiales comerciales de prótesis de cadera incluso sin lubricación. En el trabajo futuro, el uso de Ti_2AlC y Ti_3AlC_2 recubrimientos debe ser seguido por el estudio de estos recubrimientos biocompatibilidad comportamiento y osteointegración. Para verificar su uso en aplicaciones clínicas, deberá realizarse un análisis sobre un implante de cadera comercial y un ensayo de tribocorrosión.

Abstract

The hip is one of the most known ball-and-socket joint is formed by the head of the femur, seated in the pelvis (acetabulum). In the last couple of decades, total hip replacement (THR) has been a highly successful surgical intervention. Unfortunately, Peru does not have a national registry like the American Academy of Orthopaedic Surgeons. However, based on record from the 5 years prior to 2020, in average an anual admission of between 20-70 patient per hospital level II-2 or III-1 are reported. The revision of the hip joint implant indicates the end of the successful replacement surgery and announces a return to symptoms that frequently much outweigh those of the initial condition. The main reasons recorded were: infection and inflammation (20.1%), instability (18.3%), aseptic loosening (15.9%), mechanical complications (14.9%), among others.

In this context, biotribology studies the interactions of surfaces in contact under relative motion in biological systems. To reduce material loss, a layer of lubricant might be applied to prevent direct contact. Due to the increase of patients younger than 30 years, who require implants that do not limit their activities and last longer than 10 years, research continues on new safe metallic or ceramic implant coatings under tribological and corrosive behavior evaluations to reduce the possibility of a short-term revision that sets back the patient rehabilitation. In this context, this thesis submits an alternative for solid lubricants as coatings on the femoral head of hip implants.

This thesis has two main purposes. First, it is a revision of the current advances in coating technology for tribological improvements in hip replacement materials. This is done mostly by reviewing the results on different tribometers set-ups. Secondly, it presents the first successful attempt on creating a coating of Ti_2AlC and Ti_3AlC_2 coatings over a stainless steel substrate. The structural and morphological characterization of these coatings was performed by techniques like Scanning Electron Microscopy, X-Ray diffraction and Raman spectroscopy. The results evidence a significant formation of MAX phases over a AISI 304 stainless steel substrate with a diffusion barrier of Si_xN_y .

These samples were subsequently tested by a tribometer ball-on-flat in to find out if the Coefficient of Friction (COF) was affected. The 6 configurations worked were a combination of 3 forces (0.16 N, 0.8 N and 1.6 N) with 2 speeds (2 mm s^{-1} and 10 mm s^{-1}) against a 4 mm diameter ball of AISI 52100 for 15 minutes. The results were promising, as in all conditions tested, Ti_3AlC_2 had a COF around 0.13. The Ti_2AlC coating on AISI 304 had similar values to uncoated AISI 304 at high forces (COF between 0.7 and 0.75), but as the speed and thus the stroke increased, the Ti_2AlC had a more stable COF around 0.72 for all forces. In general, the COF was reduced in the long term for the specimens with Ti_2AlC and Ti_3AlC_2 coatings compared to uncoated AISI 304.

For the characterization of the tracks left after the tribological test, SEM-EDX was used for a linescan of the composition of a cross-section of tracks and point analysis of points around the border of the track (where the ball changes its direction). Also Raman spectroscopy was used to characterize the by products around the tracks with higher forces applied (1.6 N). The Ti_2AlC had visible marks and high wear of the coating, with the only exception of the track at 2 mm s^{-1} and 0.16 N. The Ti_3AlC_2 had the least visible marks, and only at low speed and high force (2 mm s^{-1} and 1.6 N) there was wear of the coating. In general, most of the debris in the results of the elemental analysis came from from the ball counterpart of AISI 52100.

In conclusion, there were promising results on the reduction of COF values from both Ti_2AlC and Ti_3AlC_2 coatings. Specially of Ti_3AlC_2 , since it had the least particles formation and coating wear with a COF lower than commercial hip replacement materials even without lubrication. In the future work, the used of Ti_2AlC and Ti_3AlC_2 coatings must be follow up by the studied of these coating biocompatibility behavior and osteointegration. To verified is used in clinical application, an analysis over a commercial hip implant and tribocorrosive test should be carried out.

Acknowledgements

First of all I want to acknowledge my supervisor Prof. Dr.-Ing. Rolf Grieseler. Without him and his patience, this work would not have been possible. I will be always be grateful for the opportunity of experience hours in the lab and for allowing me to discover how incredible the world of tribology is. I have no words to express my gratitude as most of the things I have learned in the last 2 years are from him. I am grateful that you let me join the research team "Materials Science and Renewable Energies". And of course, thanks to the rest of the group who helped me during during my training, for always being available to help.

My two *Alma mater*, "Universidad Peruana Cayetano Heredia"(UPCH) and "Pontificia Universidad Católica del Perú"(PUCP). This study expenses were sponsored by two projects funded by PUCP: CAP PI0643 "New two-dimensional materials: synthesis of 2D 'MXenos' carbides with tunable properties for energy and environmental applications." and CAP PI0732 "Synthesis and characterization of Ti_2AlC and Ti_3AlC_2 MAX phase materials as electrical conductive, anticorrosive and anti-wear protective coatings". I am deeply grateful to "Pontificia Universidad Católica del Perú", I owe to you all. To Centro de Caracterización de Materiales"(CAM-PUCP), for allowing me to use their facilities during the development of this work.

To my supervisor in Chile, Prof. Dr.-Ing. Andreas Rosenkranz, for accepting me in his research facilities and supplis. To Dr. Jose Y. Aguilar Hurtado, for giving me the opportunity to discuss ideas, be willing to educate others how to operate the devices without any limitation and offer me full support during my stay in Chile. For the open doors and access to top facilities, to the Department of Chemical Engineering, Biotechnology and Materials, FCFM, University of Chile. And again, to my supervisor Prof. Dr.-Ing. Rolf Grieseler, who made contact between me and the group in Chile, enabling me to discover how fascinating the world of research is.

To my close friends, for your words of support and the hours spent in laboratories together. I am sure that no matter what research or work follows, you will do well.

Last but not least, I would like to dedicate this work to my family for their unwavering

support in my life. To my parents and my sister, always relying on me and teaching me to do my best. To my grandparents, always by my side.



Contents

Resumen	I
Abstract	III
Acknowledgements	V
Contents	VII
List of Tables	IX
List of Figures	X
Introduction	1
1. Theoretical framework and state-of-the-art	5
1.1. Tribology and biotribology of human joints	5
1.2. Tribology of biomaterials in hip implants	10
1.3. Characterization techniques for hip replacement coatings	15
1.3.1. Tribometers	15
1.3.2. Scanning Electron Microscopy (SEM)	17
1.3.3. X-ray diffraction	18
1.3.4. Raman spectroscopy	19
1.4. Corrosion of biomaterials in hip implants	19
1.5. Friction and Wear of MAX phase coatings	20
2. Experimental methodology of morphological analysis and tribological evaluation in pin-on-flat tribometer of MAX phases as a coating of 304 surgical steel.	23
2.1. 304 Surgical Steel and MAX Phase Coating Samples	24

2.2. Tribological characterization	25
2.3. Morphological characterization	28
2.3.1. Scanning Electron Microscope	28
2.3.2. X-Ray Diffraction	28
2.3.3. Raman Spectroscopy	29
3. Results and discussion	30
3.1. Morphological characterization prior to the tribological testing	30
3.2. Tribological test of coefficient of friction by variations of normal force and speed	36
3.2.1. Results at 2 mm s ⁻¹	36
3.2.2. Results at 10 mm s ⁻¹	51
Conclusions and Recommendations	64



List of Tables

1.1. Friction and wear of biomaterials used in hip implants. MCP: Mean contact pressure. COF: coefficient of friction. F_n : Normal force applied.	14
1.2. Friction and Wear of MAX Phases.	21
2.1. The hertzian contact pressure for the contact between the AISI 52100 steel ball and a samples plane	27
3.1. High intensity peaks location found for Ti_2AlC , Ti_3AlC_2 , Fe-Austenite and aluminum oxide. Adapted from:(Zandrahimi et al. 2007; Ansari and Husain 2011; Karunakaran, Anilkumar, and Gomathisankar 2011; L. Wang and Sun 2013; Quan and He 2015; Sanati, Raeissi, and Edris 2017; Abdo et al. 2021; Torres et al. 2021; Naeem et al. 2022; Quispe et al. 2022)	32
3.2. High intensity peaks location in Raman spectrum of Ti_2AlC , Ti_3AlC_2 , aluminum oxide and graphite. Adapted from: (Presser et al. 2012; Rao, Pierce, and Dasgupta 2014; Torres et al. 2021)	34
3.3. Coefficients of friction of Ti_2AlC , Ti_3AlC_2 and AISI 304 at combinations of the normal forces (0.16 N, 0.8 N, and 1.6 N) and speed (2 mm s^{-1} and 10 mm s^{-1}).	36

List of Figures

1.	Data on hip replacements and hip revisions in ESSALUD between 2012-2021. Based on data provided by ESSALUD	2
1.1.	Graphical representation of the tribological interactions between two surfaces in contact with each other (Vakis et al. 2018)	6
1.2.	Graphical representation of parameters coefficient of friction and Wear Rate (<i>Tribology Laboratory at Lehigh University: 2012</i>)	8
1.3.	Representation of the Stribeck curve and its regimes developed in Origin. Adapted from (Kretzer 2013)	10
1.4.	Timeline of problems with metal-on-metal hip implants with cobalt and chromium. Adapted from (Cohen 2012)	12
1.5.	Schematic of a ball on flat tribometer.	16
2.1.	Workflow synthesis of the project: 1) To determine if the coatings were produced, the surface must first be characterized. 2) The tribological test simulate joint movement and its wear. 3) An evaluation of the final surface characterisation enables a comparison to determine if the coatings were damaged and how the byproducts are distributed.	24
2.2.	Ball-on-flat tribometer schematic and distribution of tracks in each sample.	26
3.1.	Atomic Concentration comparison of standard AISI 304 and the steel substrate used for coated samples. Based on (AlHazaa and Haneklaus 2020; Borba et al. 2020)	31
3.2.	Atomic Concentration of selected elements found in the MAX phase coated samples.	32
3.3.	Bragg Brentano configuration-X-Ray diffraction patterns of AISI 304 stainless steel, MAX Ti_2AlC at $700^\circ C$ MAX and Ti_3AlC_2 at $950^\circ C$	33

3.4. Raman spectrums of AISI 304 stainless steel, MAX Ti_2AlC at 700°C MAX and Ti_3AlC_2 at 950°C	35
3.5. COF analysis for Steel, Ti_2AlC and Ti_3AlC_2 at 2 mm s ⁻¹ and 0.16 N.	37
3.6. Scanning electron microscope-energy dispersive X-Ray detector (SEM-EDX) analysis of Ti_2AlC at 15 kV. SEM micrographs of the wear track at 2 mm s ⁻¹ and 0.16 N. The orange dashed line shows the position of the wear track.	38
3.7. EDX points analysis on the scanning electron microscopy (SEM) images of Ti_2AlC wear particles around a wear track at 2 mm s ⁻¹ and 0.16 N.	39
3.8. Scanning electron microscope-energy dispersive X-Ray detector (SEM-EDX) analysis of Ti_3AlC_2 at 15 kV. SEM micrographs of the wear track at 2 mm s ⁻¹ and 0.16 N. The orange dashed line shows the position of the wear track.	39
3.9. EDX points analysis on the scanning electron microscopy (SEM) images of Ti_3AlC_2 wear particles around a wear track at 2 mm s ⁻¹ and 0.16 N.	40
3.10. COF analysis for Steel, Ti_2AlC and Ti_3AlC_2 at 2 mm s ⁻¹ and 0.8 N.	41
3.11. Scanning electron microscope-energy dispersive X-Ray detector (SEM-EDX) analysis of Ti_2AlC at 15 kV. SEM micrographs of the wear track at 2 mm s ⁻¹ and 0.8 N. The orange dashed line shows the position of the wear track.	42
3.12. EDX points analysis on the scanning electron microscopy (SEM) images of Ti_2AlC wear particles around a wear track at 2 mm s ⁻¹ and 0.8 N.	43
3.13. Scanning electron microscope-energy dispersive X-Ray detector (SEM-EDX) analysis of Ti_3AlC_2 at 15 kV. SEM micrographs of the wear track at 2 mm s ⁻¹ and 0.8 N. The orange dashed line shows the position of the wear track.	44
3.14. EDX points analysis on the scanning electron microscopy (SEM) images of Ti_3AlC_2 wear particles around a wear track at 2 mm s ⁻¹ and 0.8 N.	45
3.15. COF analysis for Steel, Ti_2AlC and Ti_3AlC_2 at 2 mm s ⁻¹ and 1.6 N.	46
3.16. Raman spectrums of Ti_2AlC at 700°C MAX at 2 mm s ⁻¹ and 1.6N, where the wear was maximum.	47
3.17. Scanning electron microscope-energy dispersive X-Ray detector (SEM-EDX) analysis of Ti_2AlC at 15 kV. SEM micrographs of the wear track at 2 mm s ⁻¹ and 1.6 N. The orange dashed line shows the position of the wear track.	48
3.18. EDX points analysis on the scanning electron microscopy (SEM) images of Ti_2AlC wear particles around a wear track at 2 mm s ⁻¹ and 1.6 N.	48
3.19. Raman spectrums of Ti_3AlC_2 at 950°C MAX at 2 mm s ⁻¹ and 1.6N, where the wear was maximum	49

3.20. Scanning electron microscope-energy dispersive X-Ray detector (SEM-EDX) analysis of Ti_3AlC_2 at 15 kV. SEM micrographs of the wear track at 2 mm s^{-1} and 1.6 N. The orange dashed line shows the position of the wear track.	50
3.21. EDX points analysis on the scanning electron microscopy (SEM) images of Ti_3AlC_2 wear particles around a wear track at 2 mm s^{-1} and 1.6 N.	50
3.22. COF analysis for Steel, Ti_2AlC and Ti_3AlC_2 at 10 mm s^{-1} and 0.16 N.	51
3.23. Scanning electron microscope-energy dispersive X-Ray detector (SEM-EDX) analysis of Ti_2AlC at 15 kV. SEM micrographs of the wear track at 10 mm s^{-1} and 0.16 N. The orange dashed line shows the position of the wear track.	52
3.24. EDX points analysis on the scanning electron microscopy (SEM) images of Ti_2AlC wear particles around a wear track at 10 mm s^{-1} and 0.16 N.	52
3.25. Scanning electron microscope-energy dispersive X-Ray detector (SEM-EDX) analysis of Ti_3AlC_2 at 15 kV. SEM micrographs of the wear track at 10 mm s^{-1} and 0.16 N. The orange dashed line shows the position of the wear track.	53
3.26. EDX points analysis on the scanning electron microscopy (SEM) images of Ti_3AlC_2 wear particles around a wear track at 10 mm s^{-1} and 0.16 N.	54
3.27. COF analysis for Steel, Ti_2AlC and Ti_3AlC_2 at 10 mm s^{-1} and 0.8 N.	54
3.28. Scanning electron microscope-energy dispersive X-Ray detector (SEM-EDX) analysis of Ti_2AlC at 15 kV. SEM micrographs of the wear track at 10 mm s^{-1} and 0.8 N. The orange dashed line shows the position of the wear track.	55
3.29. EDX points analysis on the scanning electron microscopy (SEM) images of Ti_2AlC wear particles around a wear track at 10 mm s^{-1} and 0.8 N.	56
3.30. Scanning electron microscope-energy dispersive X-Ray detector (SEM-EDX) analysis of Ti_3AlC_2 at 15 kV. SEM micrographs of the wear track at 10 mm s^{-1} and 0.8 N. The orange dashed line shows the position of the wear track.	57
3.31. EDX points analysis on the scanning electron microscopy (SEM) images of Ti_3AlC_2 wear particles around a wear track at 10 mm s^{-1} and 0.8 N.	57
3.32. COF analysis for Steel, Ti_2AlC and Ti_3AlC_2 at 10 mm s^{-1} and 1.6 N.	58
3.33. Raman spectrums of Ti_2AlC at 700°C MAX at 10 mm s^{-1} and 1.6N, where the wear was maximum	59
3.34. Scanning electron microscope-energy dispersive X-Ray detector (SEM-EDX) analysis of Ti_2AlC at 15 kV. SEM micrographs of the wear track at 10 mm s^{-1} and 1.6 N. The orange dashed line shows the position of the wear track.	60

3.35. EDX points analysis on the scanning electron microscopy (SEM) images of Ti_2AlC wear particles around a wear track at 10 mms^{-1} and 1.6 N	60
3.36. Raman spectrums of Ti_3AlC_2 at 950°C MAX at 10 mms^{-1} and 1.6N , where the wear was maximum	61
3.37. Scanning electron microscope-energy dispersive X-Ray detector (SEM-EDX) analysis of Ti_3AlC_2 at 15 kV . SEM micrographs of the wear track at 10 mms^{-1} and 1.6 N . The orange dashed line shows the position of the wear track.	62
3.38. EDX points analysis on the scanning electron microscopy (SEM) images of Ti_3AlC_2 wear particles around a wear track at 10 mms^{-1} and 1.6 N	63
3.39. Comparison of COFs analysis for Steel, Ti_2AlC and Ti_3AlC_2 at each speed and force combination.	65



Introduction

Justification and problem

The American Academy of Orthopaedic Surgeons defines the hip as a ball-and-socket joint formed by the head of the femur, seated in the pelvis (acetabulum). (Ferguson et al. 2018) describes hip arthroplasty or total hip replacement (THR) as a highly successful surgical intervention, where pieces of bone are removed and replaced with metal, plastic or ceramic implants (AAOS 2021). In this context, biotribology studies the interactions of surfaces in contact under relative motion in biological systems (Kretzer 2013; Hutchings and Shipway 2017a; Menezes et al. 2013). Joint and implant surfaces experience friction and produce particles (through wear) that are released into the underlying tissue. To reduce material loss, a layer of lubricant might be applied to prevent direct contact (Ren et al. 2010; Hutchings and Shipway 2017a; Mang and Dresel 2007). In the hip, implants generate damage to adjacent tissues during activities of high duration and load, impaired lubrication loosens the implant (Bergmann et al. 2001). Due to the increase of patients younger than 30 years old, who require implants that do not limit their activities and last longer than 10 years, research continues on new safe metallic or ceramic implant coatings under previously mentioned tribological and corrosive behavior evaluations to reduce the possibility of a short-term revision that sets back the patient rehabilitation.

At present, Peru does not have a national registry, but based on theses in the 5 years prior to 2020, in average an annual admission of between 20-70 patient per hospital level II-2 or III-1 are reported (Zanabria 2020; Palomino et al. 2016; Goodman 2021; Vento 2016). The information is provided by the Central Operations Management of ESSALUD in Letter N°111-GCOP-ESSALUD-2022, on the number of hip replacements and revisions in the 22 hospitals in the ESSALUD networks between the years 2012-2021 (Figure 1). It can be evidenced how the hip replacement procedure was increasing until 2019 (1,704 THR) and showed a reduction to 704 cases during the first year of the pandemic. In 2021, major networks reported increasing

numbers, particularly among women over the age of 60. In the United States, 2.2 million THR were recorded between 2012-2020 (AAOS 2021). But during the waves in the COVID-19 pandemic, it dropped from 25,000 per month to 3,000. The “Organization for Economic Cooperation and Development” (OECD) reports (Pabinger et al. 2018) that Germany leads in the number of hip replacements with 309 surgeries per 100,000 inhabitants in 2017, similar to the 307 cases in Switzerland. In Latin American nations, 11,601 THR were done in Mexico in 2017 and 8,795 in Chile.

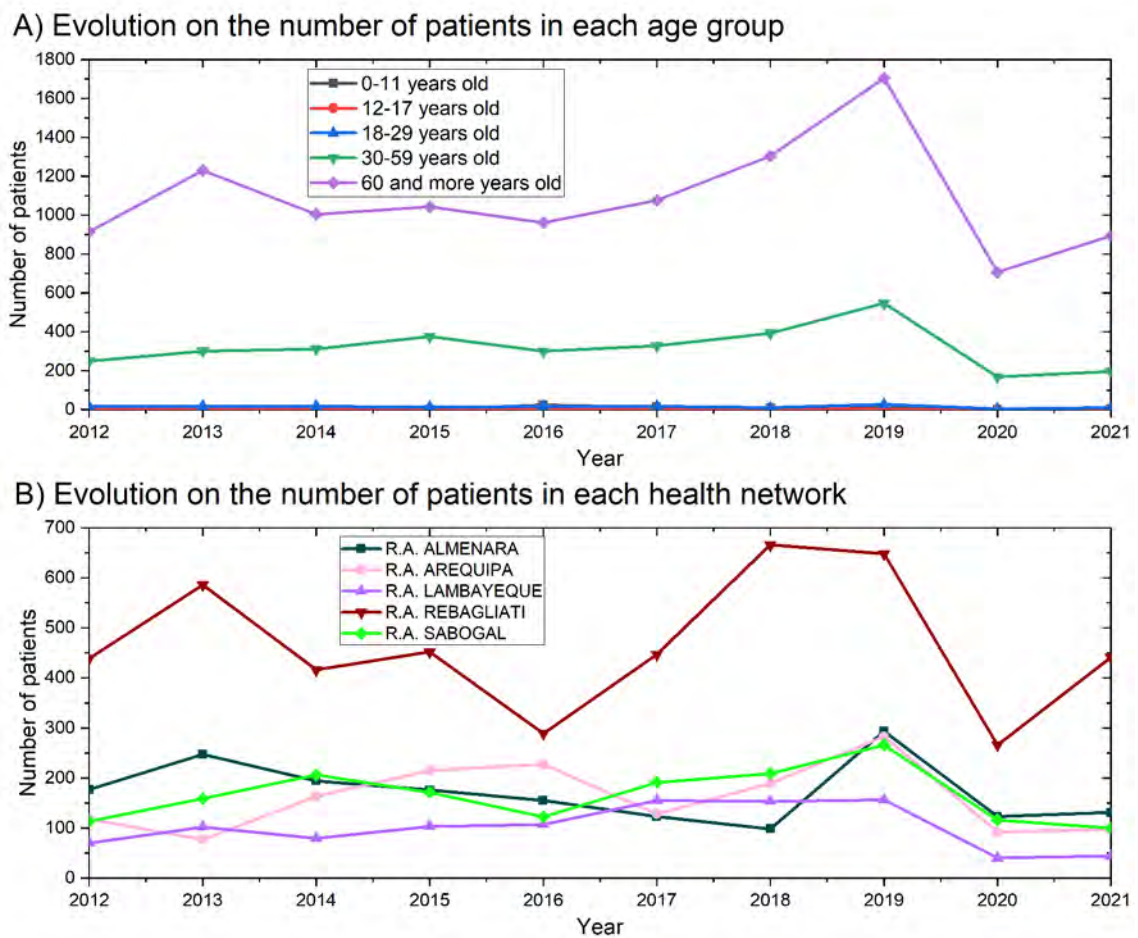


Figure 1: Data on hip replacements and hip revisions in ESSALUD between 2012-2021. Based on data provided by ESSALUD

Between 2012-2020, a AAOS recorded 61,214 THR revisions out of a total of 927,375 hip arthroscopies (AAOS 2021). The main reasons recorded were: infection and inflammation (20.10%), instability (18.30%), aseptic loosening (15.90%), mechanical complications

(14.90%), among others. The majority of revisions (52.80%) are done during the first three months, with diagnoses linked with mechanical problems and wear accounting for 62.80%. Based on evidence of rising population and lifespan, the OECD predicts that the number of annual THRs will reach 2.8 million by 2050 (Pabinger et al. 2018).

The revision of the hip joint implant indicates the end of the successful replacement surgery and announces a return to symptoms that frequently much outweigh those of the initial condition. As a result, the starting state of a revision procedure cannot be compared to that of an original implant. Because revision surgery entails not only surgery, but also continual risks and follow-ups, as well as a special attention to the patient evolution (Volkman 2009; Bayliss et al. 2017). Considering that the risk from hip implant use doubles every 5 years (Hughes, Batra, and Hallstrom 2017), the OECD recommends increasing the quality of procedures to improve implant lifespan and reduce complications (Pabinger et al. 2018). Currently, the use of biomaterials or coatings is being investigated. Despite an improvement in patient survival (80% after 20 years), implant loosening has been noted, particularly in more active patients (Bozic et al. 2009; Karachalios, Komnos, and Koutalos 2018). The aforementioned points make it clear that there are still issues with coatings that might cause an inflammatory reaction following THR. Therefore, there is still a need to develop a novel coating for metallic implants that enables patients to avoid difficulties right away after implantation and hence reintegrate into their life more rapidly.

Objectives

General Objective

The main goal of this thesis is to evaluate the tribological behavior of Ti_3AlC_2 and Ti_2AlC MAX phases coating on surgical stainless steel 304, as well as to assess its potential usage as a solid lubricant for future use as a hip prosthesis femoral head coating.

Specific Objectives

The first aim of this thesis is the evaluation of the state of the art of solid lubrication and hip implants. The properties of the Ti_3AlC_2 and Ti_2AlC MAX phases as a coating of surgical steel 304 are also described in this thesis, together with the tribological characteristics of AISI 304 stainless steel. This study was conducted with the intention of contrasting surgical steel that has

been coated with Ti_3AlC_2 and Ti_2AlC MAX phases with surgical steel that has not been coated.

Thesis Outline

The first chapter of this thesis is focused on reviewing the background and general literature on the tribological and corrosive properties of current biomaterials in hip replacements and MAX phases. On the other hand, the same chapter reviews and describes the most commonly used techniques to characterize the tribological behavior of biomaterials. With the information found, a detailed description of the work methodology during the research of this thesis is found in Chapter 2. Chapter 3 focuses on describing the results of each stage of the thesis and it explains the behaviors evidenced to finish with the presentation of Conclusions and Recommendations.



Chapter 1

Theoretical framework and state-of-the-art

The topics of tribology and biomaterials are explained in detail in this chapter in order to prepare the reader for the material to follow in the thesis. The introduction of MAX phases and a demonstration of their tribological characteristics will also be covered. The tables that will be shown will provide an overview of tribology and corrosion research on biomaterials for orthopedic implants as well as MAX phases in industrial applications. MAX phases as a biomaterial haven not received much attention, thus traits resembling those investigated in biomaterials are discussed.

1.1. Tribology and biotribology of human joints

Tribology is defined as the branch of science and technology that studies the interactions of surfaces in contact and under relative motion between them. It includes the study of friction, wear and lubrication (Hutchings and Shipway 2017a). When two surfaces are in contact frictional forces are generated between the bodies, this contact Figure 1.1 causes the surfaces to

experience wear that could eventually lead to premature failure. To reduce the frictional force, lubricants are used to prevent rough contact between the surfaces (Mang and Dresel 2007). All tribological phenomena are produced by some atomic interaction between the surfaces in contact or with the lubricant, with the most important phenomena being mechanical (material removal or deterioration where the softer material tends to be removed by the harder material (Roy 2017)) and thermal (contact heat transfer and generation (Hutchings and Shipway 2017a)).

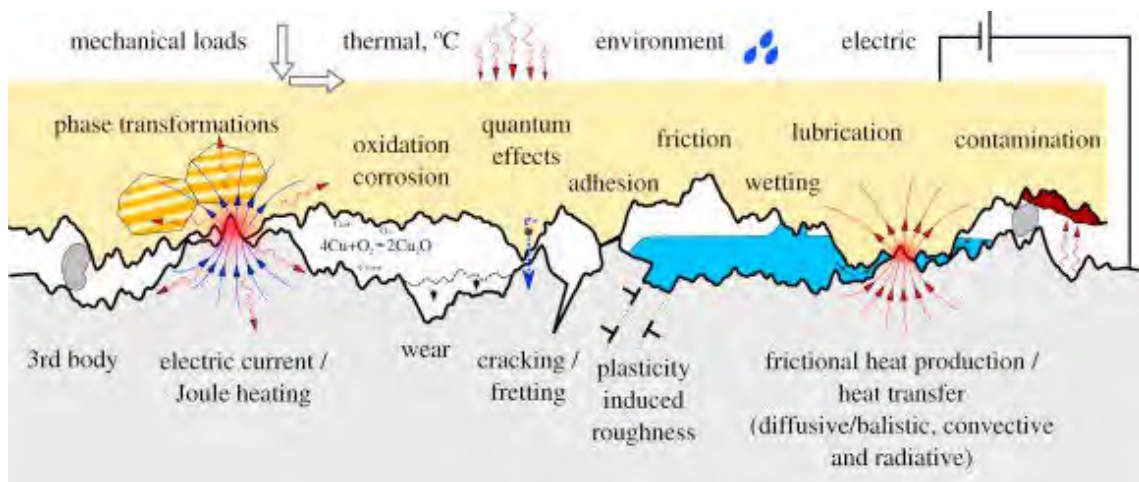


Figure 1.1: Graphical representation of the tribological interactions between two surfaces in contact with each other (Vakis et al. 2018)

Wear occurs through various material removal mechanisms, these mechanisms include abrasion, adhesion, cohesion, erosion, corrosion, etc. (Roy 2017). In most cases, wear is detrimental, causing increased clearance between moving components, unwanted freedom of movement, and loss of accuracy (Hutchings and Shipway 2017a). High coefficient of friction values in engineering applications would result in high frictional forces causing frictional energy losses, wear and possible overheating.

To reduce such losses, a layer of lubricant is applied between the surfaces, thus avoiding direct contact between solid surfaces (Hutchings and Shipway 2017a; Hutchings and Shipway 2017a; Mang and Dresel 2007). A variety of materials are used as solid and liquid lubricants

(Scharf and Prasad 2013). However, in some engineering applications, it is not practical to apply lubricants; as a result, these surfaces contact without lubrication, causing dry sliding wear. If the surfaces are not self-lubricating, the presence of hard particles may induce abrasive wear (Hutchings and Shipway 2017a). On the other hand, there are circumstances in which solid lubricants are the only workable option, such as in sanitary equipment where contamination by a liquid lubricant must be avoided, or in space (or any other high vacuum environment) where a liquid lubricant would evaporate. Additionally, at high temperatures, liquid lubricants breakdown or oxidize (Nowak, Kucharska, and Kamiński 2019), which is why solid lubricants are preferred. To minimize wear, coatings with good adhesion to the substrate are often used, where the elastic and plastic properties of the coating may differ from those of the underlying material, these coatings have the function of protecting and extending the life of the components (Wood 2006).

The friction and wear behavior of all materials is affected by several characteristics and environmental variables, including: material pairing (known as tribopair), applied normal load, sliding speed, surface topography and roughness, environment, chemical interactions, and sliding configuration (determined by the tribometer). The most known tribological parameter is the COF (μ), a dimensionless number based on Amontons' first law of friction, which states that the friction force (F_r) is directly proportional to the normal load as shown in Figure 1.2. Themistius (317-390 CE) conducted the first recorded study of friction and discovered that the friction for sliding is larger than that for rolling (Menezes et al. 2013). Centuries later, more systematic experimental investigations were conducted by Leonardo da Vinci in the 1500s and later by Amontons in 1699, verified by Euler in 1750 and Coulomb in 1781. Their empirical laws were: the friction force is directly proportional to the normal load, the friction force is independent of the apparent area of contact and it is almost independent of the sliding velocity. In order to comply with the above-mentioned, it is usually assumed that the friction force is proportional

to the real area of contact (A) and A is proportional to the normal load (F_n).

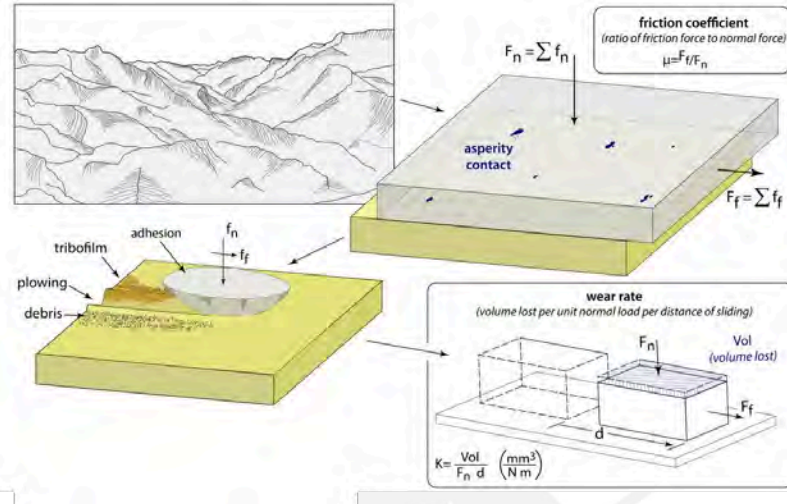


Figure 1.2: Graphical representation of parameters coefficient of friction and Wear Rate (*Tri-bology Laboratory at Lehigh University: 2012*)

$$\mu = \frac{F_r}{F_n} \quad (1.1)$$

$$W_r = \frac{V}{dF_n} \quad \left[\frac{\text{mm}^3}{\text{N} \cdot \text{m}} \right] \quad (1.2)$$

A friction coefficient can then be defined by this: Wear, as is mentioned before, is a process that occurs when two surfaces are sliding against one another, resulting in gradual removal of one or both materials, depending of the roughness of each material. Archard and Holm suggested that the total volume of material removed during sliding (the wear volume V) is proportional to the normal force applied multiplied by the sliding distance by the proportionality constant known as a wear factor or K .

This wear factor can be a property of the material set, sliding conditions, among other things. One remarkable observation is that wear can vary more than eight orders of magnitude across material systems. It can also vary just by changing the environment or the counter-material that

the material is sliding against. Wear is commonly used as an indicator of a material's status during its life time.

Lubricants comply with four lubrication regimes (hydrodynamic, elastohydrodynamic, mixed and boundary) Figure 1.3, where behavior of the coefficient of friction depending on the lubricant thickness (according to the Hersey number) is plotted on the Stribeck curve. The friction coefficient depends on the Hersey number such that it is equal to the product of the dynamic viscosity times the rotational speed (v) divided by the average load (F) (Y. Wang and Q. J. Wang 2013). In the regime for boundary lubrication, the surfaces are covered with a thin film of lubricant where friction and wear are determined primarily by the properties of the contact surfaces and secondarily by the properties of the lubricant. In the case of mixed film lubrication there is a space partially covered by a lubricant film where the load is supported by both the lubricant film and the spray forces, a decrease in coefficient of friction can be observed. The elastohydrodynamic lubrication regime is often confused as part of the mixed film regime, but this is characterized by having a continuous and uninterrupted lubricant film between the contact surface and the dynamic viscosity of the lubricant alone controls the friction properties, since the surfaces do not show wear. Finally, there is hydrodynamic lubrication which is characterized by a relatively thick lubricant film where surfaces do not wear and rigid body geometries are assumed, as well as the constant viscosity of the lubricants (Dowson 2012; Scharf and Prasad 2013; Y. Wang and Q. J. Wang 2013; Wäsche and Woydt 2014; Z. Xu et al. 2015).

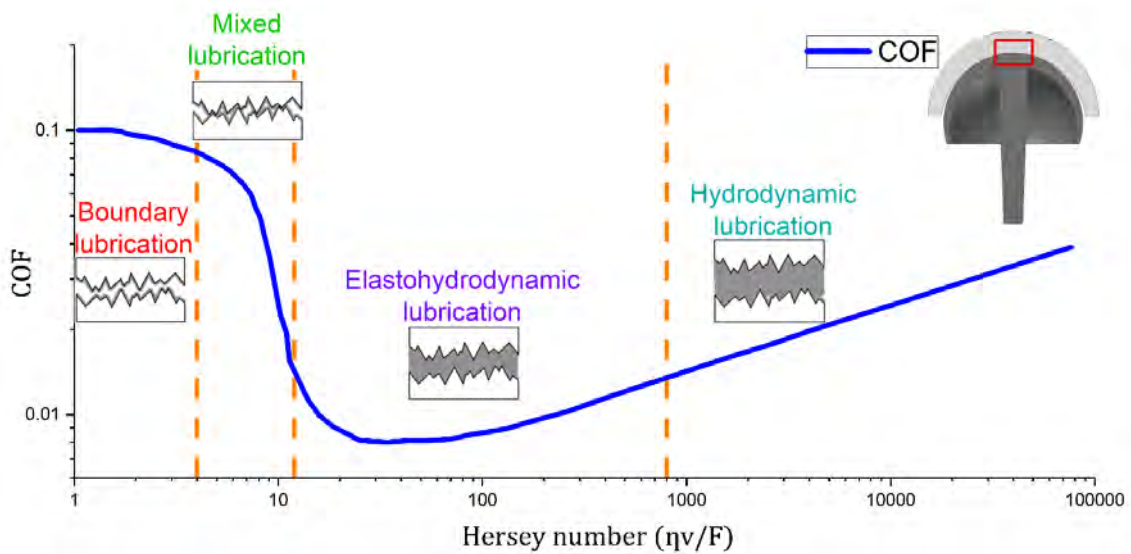


Figure 1.3: Representation of the Stribeck curve and its regimes developed in Origin. Adapted from (Kretzer 2013)

1.2. Tribology of biomaterials in hip implants

The main goal of a biocompatibility test is to study the effects of the interaction between implant materials and patient tissues. The mechanical test aims to simulate real biomechanical environment and loading conditions in order to compare the proposed system or new variations (Boutrand 2019). Since humans have started to investigate the human locomotion system, static and active models have been developed to simulate implants interactions. The most common biomaterials used in orthopedic prosthesis are metals, polymers, ceramics, composites and apatite (Aherwar et al. 2015).

Biotribology is the study of tribology in biological systems and illnesses caused by tribological wear and tear, as well as the optimization of therapies and medical equipment (Zhou and Jin 2015). All structures in the human body eventually age to some extent. Despite the fact that a healthy human joint may be anticipated to live for more than 70 years with low friction and wear (Kretzer 2013), an accident in the cartilage in joints can cause considerable wear and tear,

needing replacement. It is critical to investigate the tribology of these joints, particularly prostheses, because the surfaces in continual contact create particles (due to wear) that are released into the underlying tissue. In the case of an artificial hip joint, the materials and components of the joint must meet both biological and mechanical requirements. As a result, components must be produced with accuracy and congruent surfaces to provide reduced friction during hip functions.

In light of the recent rise in demand for medical devices, particularly orthopedic implants, the issue of their efficacy has been researched and, as a result, developed into a complex regulatory framework to guarantee their performance, safety, and quality. The study of wear debris and its interactions with surrounding tissue have become a key component of hip implant biotribology in recent years. (Wadhwa, Talegaonkar, and Popli 2019) investigated the regulation of hip and knee joint replacement medical devices. They investigated the Johnson & Johnson ASR Implant as a result of considerable reforms brought about by the failure of its hip implants. This case study is documented in Figure 1.4. The case shows that since the start of the use of a metal in hip replacement there were concerns of their effect on patients. In general, biomaterials continue to increase the quality and endurance of human prostheses. The development of new materials has an impact, starting with the selection of the biomaterial, which should consider its compatibility with the human body as well as its behavior while sustaining the load-bearing function of human bones (Aherwar et al. 2015). |

Despite the growing knowledge of how the loads variate and act on implants, mechanical failure is still a common clinical failure in hip replacements (AAOS 2021). The main reason is the underestimation of the complexity of the interactions between implant design (materials) and biological system. A recent series of metal-on-metal hip implant failures has revealed the lack of sufficient preclinical testing for certain types of design (Boutrand 2019). And not only mechanical studies are needed to last a 15-years lifelong service with no possibility of routine

maintenance, implants are also subjected to aggressive chemical environmental conditions during the multidirectional loads. In order to avoid those clinical failures, standardized tests have been developed for common implants such as hip and knee joint replacement.

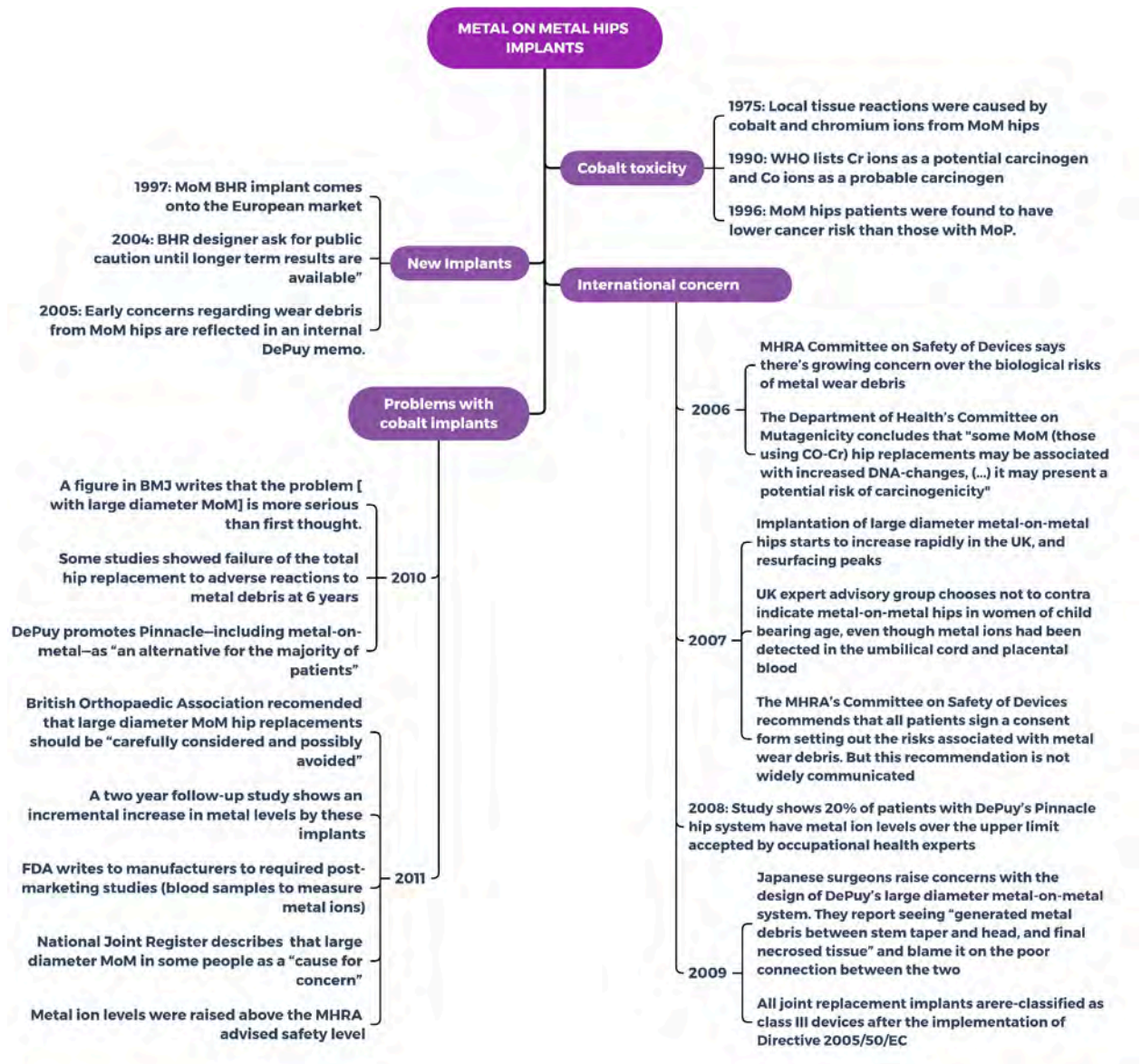


Figure 1.4: Timeline of problems with metal-on-metal hip implants with cobalt and chromium. Adapted from (Cohen 2012)

The femur bears the full weight of the body, so the hip implant in contact with the cortical bone is intended to ensure a stable fixation. When an implant is placed in the body, there

is a bi-directional biological interaction between the body and the implant material (Revell 2021). In the early 1960s, a stainless steel stem with polytetrafluoroethylene (PTFE) was used. However, its low wear resistance led to its replacement with a Co-Cr-Mo alloy and ultra-high molecular weight polyethylene (UHMWPE). (Borjali, Monson, and Raeymaekers 2019) used a Pin-on-Disc (PoD) tribometer to quantify and classify polyethylene wear in hip implants, the results described in the Table 1.1 were the basis of a model that allows the prediction of polyethylene wear. (Çelebi Efe et al. 2021) applied a UHMWPE film on the surface of Ti-6Al-4V for tribological testing against an alumina ball in Ball on Disc (BoD) tribometer. The wear results revealed that the coating has an ultra-low coefficient of friction compared to that of the Ti-6Al-4V alloy and favorable wear resistance (84% higher than oxide coatings).

(Platon, Fournier, and Rouxel 2001) studied the wear and friction of different combinations of 316L stainless steel, UHMWPE and Diamond-like carbon (DLC) coating. The tests sought to describe the tribological behavior of the materials, without performing tests on a hip simulator because of its high cost and duration. They used BoD and PoD tribometers, which revealed that DLC reduced wear due to its dry friction behavior. Another study analyzed the mechanical properties of cobalt-chromium-molybdenum alloys as (Cuao-Moreu et al. 2020) coating. To prevent the release of metal ions, an aluminum-chromium oxynitride coating was applied on an ASTM F-75 cobalt alloy. Using a BoD tribometer, they recorded a 7-fold increase in wear resistance over the untreated sample. The results of these studies and other biomaterials are shown in the Table 1.1.

In general, hip replacement is a successful procedure but excessive use of all-metal components can lead to an immune reaction, especially in patients with metal hypersensitivity (10% of the total population) (Haider et al. 2017). Given the popularity of metal-on-metal implants, a suitable possibility to extend an implant's lifespan is to modify the metal surfaces by adding surface coatings that reduce metal wear and ionic debris.

Table 1.1: Friction and wear of biomaterials used in hip implants. MCP: Mean contact pressure. COF: coefficient of friction. F_n : Normal force applied.

Tribometer	Biomaterial	Coating	Counter part	Radius (mm)	MCP (MPa)	Normal Force (N)	COF	References			
Ball-on-disk	CoCrMo	-	Al2O3	11	1.7	40	0.3	(Cuao-Moreu et al. 2020)			
		borided			1.9		0.25-0.45				
		AlCrON					0.6				
	Ti-6Al-4V	-	Al2O3	6	-	2	0.8	(Çelebi Efe et al. 2021)			
		UHMWPE	Al2O3				0.08				
		UHMWPE-Hap	Al2O3				0.06				
	316L	DLC	316L	10	-	-	483	<0.1			
	Ti-6Al-4V	DLC	Ti-6Al-4V				343	0.13-0.3			
	Al2O3	-	Al2O3				668	0.09-0.32			
	316L	DLC	UHMWPE				23	0.12-0.3			
	316L	-					23	0.15-0.3			
	Ti-6Al-4V	DLC					23	0.1-0.2			
	Al2O3	-					23	0.05-0.4			
	ZrO2	-					23	0.02-0.22			
	316L	DLC					316L	256	0.1-0.3		
	Ti-6Al-4V	DLC	Ti-6Al-4V				181	0.1-0.8			
	Al2O3	-	Al2O3	395	0.35-0.4						
	316L	DLC	UHMWPE	26	-	-	12	0.15-0.17			
	316L	-					12	0.1-0.28			
	Ti-6Al-4V	DLC					12	0.22-0.32			
Al2O3	-	14					0.48-0.51				
ZrO2	-	12					0.25-0.32				
316L	DLC	316L					12	0.2-0.45			
Ti-6Al-4V	DLC	Ti-6Al-4V	6	1	-	0.1-0.23					
Al2O3	-	Al2O3				0.1-0.22					
316L	DLC	UHMWPE				0.2-0.25					
316L	-					0.15-0.25					
Ti-6Al-4V	DLC					0.2-0.23					
Al2O3	-					0.18-0.27					
ZrO2	-		0.11-0.25								
Pin-on-disk	316L	DLC/CrN	Ti-6Al-4V	8	-	10	0.2	(Patnaik, Ranjan Maity, and Kumar 2021)			
		AlCrN/CrN					0.4				
	CoCrMo	-	UHMWPE GUR1050	9	-	-	1	0.09-0.1			
		SM 1					0.04-0.05				
		-					0.06-0.075				
		SM 1		2	0.075						
	Si3N4-TiN	-	Si3N4-TiN	1.14	-	10	0.8	(D'Andrea et al. 2021)			
Pin-on-flat	3Y-TZP	-	UHMWPE	3	3.54	25	0.35	(Smirnov et al. 2018)			
	3Y-TZP/Ta						0.26				
	UHMWPE	-	-	AISI420C	6	-	-	23.8	10	0.12	
									27.2	15	0.11
				Ti-6Al-4V					29.9	20	0.12
									-	10	-
									27.1	15	0.14
			299	20	0.13						
	UHMWPE	-	-	Ti-6Al-4V	3	1.01	1	0.134	(Ruggiero, D'Amato, Gómez, and Merola 2016)		
					6	4.02	4	0.141			
				AISI316L	3	1.02	1	0.137			
					6	1.06	4	0.132			
					10	11.23	11	0.145			
				Al2O3	3	1.01	1	0.187			
6					4.04	4	0.158				
10					11.18	11	0.143				

There is a trend of using Metal-on-Metal implants (Mihalko et al. 2020). Theoretically, these adjustments ought to decrease friction and adhesive wear while increasing hardness to reduce scratching and abrasive wear. They ought to also increase wettability to enhance lubrication.

An example of clinical success is Smith and Nephew's "Oxinium" zirconium alloy (Haider et al. 2017). Diamond-like carbon (DLC) coatings tested in vitro were also developed to evaluate their biocompatibility, corrosion resistance, superior tribological and mechanical properties (Haider et al. 2017). Aesculap Inc. patented a Zirconium nitride (ZrN) multilayer solution to dissipate forces (Haider et al. 2017). Although (Herbster et al. 2020) compared current knee replacement procedures and discovered that these strategies still had manufacturing and delamination concerns, currently Ti-6Al-4V alloy is the most widely used material as a femoral stem and femoral head (Boutrand 2019). This alloy resists metallic corrosion, which generates a release of metal ions (Mozafari 2020), through the formation of a self-protective TiO_2 surface film (Virtanen 2012). But despite this coating, the release of *Ti* ions has effects on adaptive immune cells and, if micrometer-sized, renders them ineffective for proliferation and IL-2 production in lymphocytes (Mozafari 2020). In general, titanium ions suppress lymphocyte activation and are cytotoxic at high concentrations (Mozafari 2020).

1.3. Characterization techniques for hip replacement coatings

1.3.1. Tribometers

Tribometers are devices used in most tribological investigations that aim to measure the tribological properties of two materials rubbing against each other and the effectiveness of lubricants between them. The purpose of a tribometer is to simulate friction and wear under controlled and monitored conditions without the difficulties associated to experimentation because friction and wear are altered by various factors such as variations in temperature, load, or moisture (Link et al. 2019). There are many different configurations of tribometers throughout

engineering, but the most popular is "ball-on-disk". In this configuration, the ball slides in constant contact with the disk while both can be driven independently, the disk can be large enough for several wear tests to be performed on the same disk at different radii. It is frequently used for greased lubricants due to the ball rotation that permits contact with the lubricant, however the parameters vary according to the differences in track radii (Kilgour and Elfick 2008; Seyfert 2014; Hutchings and Shipway 2017b).

Therefore, this configuration can be used as a model test for mechanical component surfaces that are subjected to high loads. Its wear debris can be pushed in front of the top sample and remain in contact for a long time (Stavlid 2020).



Figure 1.5: Schematic of a ball on flat tribometer.

A similar configuration is "ball on flat" where the disk is replaced by a plane that cannot rotate Figure 1.5. The "ball on flat" tribometer can test the tribological function of both the hip and knee joints. However, pin/ball-on-plate simulators are basic devices that do not accurately recreate the motion and stress profile experienced by human joints (Scholes and Unsworth

2009). The motion condition between the femoral head and acetabular cup may be reduced into a model where a flat surface (ball) slides against another flat surface due to the great conformity of hip joint bearing surfaces (flat). As a result, pin/ball-on-plate tribometers testing are a low-cost and straightforward method. In general, hip and knee simulators are better at mimicking realistic and complicated loading and motion profiles, but pin-on-plate machines are a superior way to perform the friction test (Shen, Fang, and Kang 2018).

1.3.2. Scanning Electron Microscopy (SEM)

SEM uses an electron beam (because of its shorter wavelength) to resolve the finer features/details of materials (Ul-Hamid 2018). The electron gun generates the electron beam and the beam is modified by apertures (control the passage of scattered electrons reaching the lenses), electromagnetic lenses (reduce the size of the beam crossing point) and coils (track the probe over the sample surface) located inside the column that focus the beam on a small (a few nanometers in diameter) probe (Dunlap and J.E. Adaskaveg 1997). The barrel, column, and sample chamber are kept in high vacuum ($< 10^{-4} Pa$) to minimize unwanted scattering (Goldstein et al. 2018). The final lateral resolution of the image corresponds to the diameter of the electron probe.

The beam generates a variety of signals. Backscattered electrons (BSEs) are beam electrons that emerge from the sample with a large fraction of their incident energy intact. Secondary electrons (SEs) are electrons that escape from the sample surface after the beam electrons have ejected them. X-rays are emitted when electrons break away from specific orbitals of an atom in the sample (Dunlap and J.E. Adaskaveg 1997). Incident electrons may also enter the sample with BSEs and SEs, causing the emission of X-rays atoms located deep inside the specimen. Additionally, the main electron beam promotes X-ray emission (Dunlap and J.E. Adaskaveg 1997; Ratner 2013).

Energy-dispersive X-ray analysis, or EDS, is a method that uses these X-rays to detect elements (Ratner 2013). The basic foundation of EDS begins with the photoelectric absorption of an X-ray photon in a semiconductor, where the energy of the photon is transferred to a bound inner shell atomic electron that is expelled. Free electrons may move in response to an applied potential, resulting in the accumulation of electrons at the anode on the back surface of the EDS detector (Goldstein et al. 2018). The interaction of an X-ray photon with a group of electrons results in the spectrum, which quantifies the photon energy that can give elemental composition mapping across the object (Dunlap and J.E. Adaskaveg 1997; Goldstein et al. 2018). The EDS spectrum is created by measuring the charge that was deposited in the detector. EDS performs site-specific elemental analysis in predetermined sections.

1.3.3. X-ray diffraction

The X-rays are the electromagnetic radiation at a wavelength range of 10^{-3} nm to 10 nm, and they are widely used from taking image of the inside of objects to reveal information on the materials such as crystal structure, phase transition, crystalline quality, orientation, and internal stress (Lee 2016). This measurements are a consequence of the interaction between X-rays and matter. First, hard X-rays penetrate into all substances at different depths (more optically opaque objects may be translucent to the hard X-rays). Secondly, X-rays have shorter wavelengths than visible light, close to the size of atoms, that allows them to be diffracted by a periodic and thus crystalline atom structure.

The X-rays are generated when electrons accelerated at a high speed, rapidly decelerate in an X-ray tube. This source contains two metal electrodes: a cathode at negative voltage (source of electrons) and an anode at ground potential (metal target). The electrons are accelerated toward the metal target by a tungsten filament within the cathode, which has an electric potential between 20 and 60 kV. When the electrons collide, they lose energy, which is then released as

X-rays.

A study comparison of the corrosion behavior of Ti-6Al-4V and 316L stainless steel for biomedical implants found that the XRD patterns of 316L stainless steel and Ti-6Al-4V were used to confirm the presence of calcium phosphate used by (Gnanavel et al. 2018) to enhanced osseointegration.

1.3.4. Raman spectroscopy

Raman spectroscopy was discovered in 1928 by using filtered sunlight; when a bright light (electromagnetic radiation) is focused on a specimen, most of the light scatters back at the same frequency as the incident beam. However, a fraction of this light excites vibrations in the specimen and can lose (stokes) or gain (anti-stokes) energy (Ratner 2013; Vandenabeele 2013). This shift in frequency correlates to vibrational bands indicative of the specimen's molecular structure and is referred to as Raman scattering. Raman scattering is a technique that uses vibrational transitions to gain information about the structure and characteristics of molecules.

The Raman spectroscopic technique has been severely limited for surface studies due to its low signal level. Raman spectroscopy will be used to examine the structural and vibrational properties of the thin films.

1.4. Corrosion of biomaterials in hip implants

Humans have been using artificial materials to repair tissues or organs for thousands of years, vanadium steel was among the first metals developed for bone fracture fixation. Unfortunately, it was discarded due to its low corrosion resistance, mechanical failures and poor biocompatibility (Eliaz 2019). Metallic corrosion is an electrochemical RedOx process (oxidation and reduction reactions) that depends on the environment (Mozafari 2020; Eliaz 2019).

In implants, corrosion is evidenced as metal degradation where surface metal ions are released into the body (Boutrand 2019) and can be assisted by mechanical movement. When corrosion is evident cracks usually occur at the junction of the parts and, after implantation, the amount of metal ions is usually the highest with a decrease over time (Mozafari 2020).

As previously stated, while selecting metals, chemical resistance and the ability to apply protective methods like as passivation or surface treatments are considered (Pruitt and Chakravartula 2011; Sin, Hu, and Emami 2013). (Swaminathan and Gilbert 2012) developed an electrochemical and fretting corrosion test system. To validate the model, they performed experiments on combinations of Ti-6Al-4V and *CoCrMo* materials. They discovered that the Ti-6Al-4V combination needed less effort to induce deterioration. (Royhman et al. 2016) developed a methodology to study this mechanical corrosion in a device using a Ti-6Al-4V stem against a *CoCrMo* femoral head. They were able to find a relationship between pH and amplitude of motion, with corrosion wear of the surfaces.

1.5. Friction and Wear of MAX phase coatings

A new material used as a solid lubricant is the $M_{n+1}AX_n$ or MAX phase. This is a class of ternary carbide and nitride with a lamellar crystalline structure; where $n = 1, 2$ or 3 , “M” is a transition metal (Ti, Cr, Hf, Zr), “A” a group IIIA and IVA element (Al, Si, Sn), and “X” is carbon or nitrogen (Eklund et al. 2010; Naguib et al. 2011). Applications of MAX phases include coatings, structural elements for applications in corrosive media, conductive thin films for micro-electronic systems.

The tribology of the MAX phases started with the study of the tribological behavior of the Ti_3SiC_2 (Myhra, Summers, and Kisi 1999) phase. They reported a coefficient of friction value of ($\mu \leq 5 \times 10^{-3}$), the lowest value found in the literature. Subsequently, there was more interest in MAX phase tribology because of its good behavior (low coefficient of friction and low

wear rate). In 2000, (El-Raghy, Blau, and Barsoum 2000) investigated Ti_3SiC_2 , where the μ increases linearly from 0.15 to 0.45 (first 5 seconds). It reaches up to 0.83 in the steady state, this could be due to the accumulation of particles between the MAX phase and the counterpart. In the following years, several tribology-related studies were reported with different counterparts such as Ti_3SiC_2 vs. bearing steel (AISI 52100) (Sarkar et al. 2005), Ti_3SiC_2 against low carbon steel (Souchet et al. 2005), Ti_3SiC_2 against steel and Si_3N_4 (Myhra, Summers, and Kisi 1999). Relevant tribological investigations that used Ti_3AlC_2 or Ti_2AlC are highlighted in the Table 1.2. Both MAX phases Ti_3AlC_2 and Ti_2AlC are used in this thesis as AISI 304 stainless steel. Tribology of MAX phases is a field where more testing is needed to better understand the tribological behavior of thin films of MAX phases.

Table 1.2: Friction and Wear of MAX Phases.

MAX phase	Tribometer	Counterpart	COF	Wear rate ($mm^3/(N \cdot m)^{-1}$)	Source
Ti_3AlC_2	Ball on flat	316L	0.53-0.56	9.89×10^{-5}	(S. Wang et al. 2016)
Ti_2AlC	Ball on flat	AISI 51200 steel	0.2-0.45	-	(Quispe et al. 2022)
Ti_3AlC_2	Ball on flat	AISI 51200 steel	0.65-0.85	-	(Quispe et al. 2022)
Ti_3SiC_2 annealed	Ball on flat	bearing steel 1.3505	0.2-0.3	-	(Hopfeld et al. 2014)
Cr_2AlC as deposited	Ball on flat	bearing steel 1.3505	0.15-0.4	-	(Hopfeld et al. 2014)
Ti_2AlN annealed	Ball on flat	bearing steel 1.3505	0.15-0.5	-	(Hopfeld et al. 2014)
Ti_3AlC_2	Ball on Disc	Al_2O_3	-	$10^{-7} - 10^{-4}$	(Jiang et al. 2011)
Ti_2AlC	Block on Disc	Low carbon steel	0.3-0.345	1.64×10^{-6}	(Cai et al. 2017)
Ti_3AlC_2	Ball on Disc	Al_2O_3	1.22	1.2×10^{-3}	(Ma et al. 2013)
Ti_2AlC	Pin on Disc	Al_2O_3	0.62	$\leq 1 \times 10^{-6}$	(Gupta et al. 2008)
$TiAl$ Composite	Ball on Disc	AISI 52100	0.55	3.98×10^{-4}	(Z. Xu et al. 2015)
Ti_3AlC_2	Block on Disc	Low carbon steel	0.13-0.33	2.5×10^{-6}	(Huang, H. Xu, et al. 2015)
Ti_3AlC_2	Ball on flat	AISI 52100	0.35-0.82	4×10^{-5}	(Wu et al. 2009)
Ti_2AlC coating	Ball on Disc	Stainless steel	0.32-0.38	-	(Cao et al. 2018)
Ti_2AlC coating	Ball on Disc	Al_2O_3	0.766	4.7×10^{-7}	(Loganathan et al. 2018)
Ti_3AlC_2	Block on Disc	Low carbon steel	0.4-0.8	2.2×10^{-6}	(Huang, Zhai, et al. 2014)



Chapter 2

Experimental methodology of morphological analysis and tribological evaluation in pin-on-flat tribometer of MAX phases as a coating of 304 surgical steel.

In this work, AISI 304 stainless steel (AISI 304 SS) was selected to be used as representative substrate of medical grade materials used in implants. Due to its properties of minimizing metal ion dissolution and preventing local corrosion, medical grade stainless steel has stricter standards on chemical composition than industrial stainless steel. For example, impurity elements like S and P have limited levels, while elements like Ni and Cr have higher presence than in regular stainless steel. Despite the massive use of AISI 316L in implants, AISI 304 is still found in dental applications and medical instruments for surgery (Zardiackas 2006). Despite having a different composition, AISI 304 has a number of benefits over AISI 316L or even AISI 304, the most significant of which being AISI 304's resistance to corrosion in simulated bodily fluids and ability to maintain biocompatibility (Tang et al. 2006; Paul and Mandal 2013).

AISI 304 stainless steel samples without coating as reference (n=1), and AISI 304 stainless steel samples with Si_xN_y coating (100 nm) and a Ti-Al-C multilayer according to (Torres et al.

2021) methodology (n=2) were used in this thesis work. The Si_xN_y layer works as a diffusion barrier to avoid the diffusion of the Ti-Al-C layers deposited over the AISI 304 substrate. The samples with multilayer underwent a heat treatment described by (Torres et al. 2021) for the formation of MAX phase coatings Ti_2AlC at $700^\circ C$ (n=1) and Ti_3AlC_2 at $950^\circ C$ (n=2). The methodology framework is described in Figure 2.1 as and overview, but each step is explained detailed in this chapter.

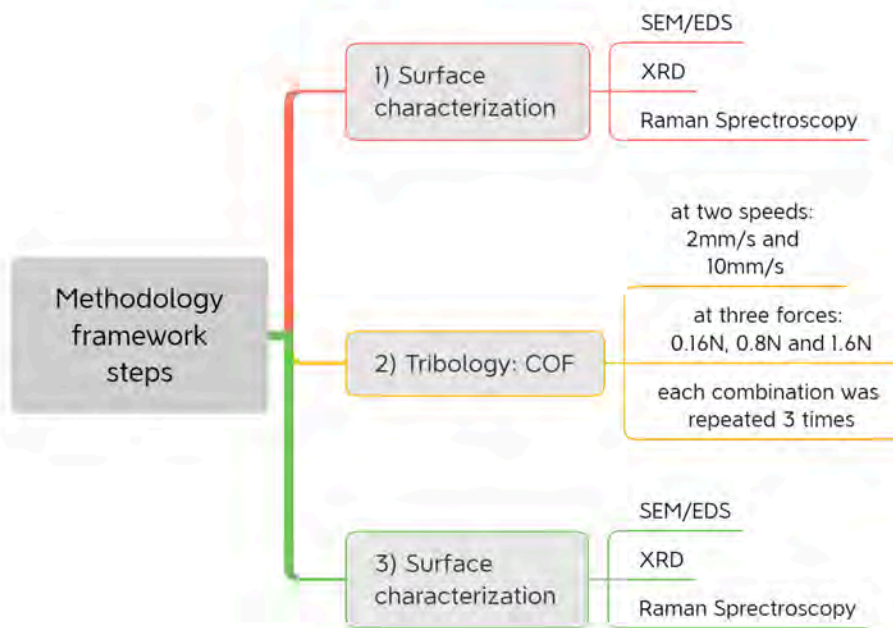


Figure 2.1: Workflow synthesis of the project: 1) To determine if the coatings were produced, the surface must first be characterized. 2) The tribological test simulate joint movement and its wear. 3) An evaluation of the final surface characterisation enables a comparison to determine if the coatings were damaged and how the byproducts are distributed.

2.1. 304 Surgical Steel and MAX Phase Coating Samples

The Center of Micro- and Nanotechnologies at Technische Universität Ilmenau used the Mid-frequency magnetron sputtering method to produce MAX-phase thin films in two steps following (Torres et al. 2021). As substrate, AISI 304 polished using electropolishing technique

with electrolytic solution of 55% H_3PO_4 , 14% H_2SO_4 and 31% H_2O was used (Awad et al. 2012; Doche et al. 2022). Subsequently, a 100 nm Si_xN_y coating, which worked as a diffusion barrier, was deposited by chemical vapor deposition (LP-CVD). Subsequently, a multilayer system was deposited using targets of titanium, aluminum and carbon that were sputtered in CS400ES magnetron sputtering system (VON ARDENEN Anlagentechnik) with a power of 200 W for Ti and Al and 500 W for C. These targets purities were 99.6% for Ti, 99.95% for Al, and 99.9% for C. The deposition of titanium (Ti), aluminum (Al), and carbon (C) multilayers was done in 22 sets, with each set consisting of layers of Ti, Al, and C with thicknesses of 14 nm, 6 nm, and 3.5 nm, respectively. The layers were deposited in a high purity argon (Ar, 5.0) atmosphere with a working pressure of $5 \cdot 10^{-3} mbar$ and a flow rate of 30 sccm.

The samples were repeatedly evacuated to reduce oxidation (Jet First, Joint Industrial Processors for Electronics), and then they were heated in the second stage using rapid thermal processing (RTP) in an environment of Ar and hydrogen. The sample was then heated to 200 °C and kept there for 300 s, allowing the water that might be adsorbed at the surface of the sample as moisture to evaporate. The samples were then heated, according on the sample, to temperatures between 700 °C and 950 °C in stages of 50 °C with a holding duration of 300 s.

2.2. Tribological characterization

Tribometer Setup

In the labs of the Department of Chemical Engineering, Biotechnology, and Materials of the University of Chile, tribology experiments were carried out on the tribometer MFT-5000 Multi Function Tribometer. Each sample was cleaned with isopropyl alcohol to remove particles and grease from the surface (Fellah et al. 2014). Commonly, according to ISO 7148-1:2012 and ASTM G99-17, hip implant materials are tested on a tribometer with pin-on-disk configurations. Nevertheless, due to the device availability, a ball on flat configuration was used (Figure 2.2)

according to ASTM G133-05 at room temperature, to find the friction coefficient.

Each test lasted 15 minutes, had a 2.5 mm stroke length, and was conducted with two sliding velocities in the hip joint's typical range (2 mm s^{-1} and 10 mm s^{-1}) while varying the normal loads (0.16, 0.8, and 1.6 N). A AISI 52100 steel ball (radius of 4 mm) served as the counterpart in all experiments, and it was changed for each sample. Each velocity and normal force were mixed in 6 different combinations (Figure 2.1), then repeated three times in a row. Each sample included 18 tracks. (Figure 2.2).

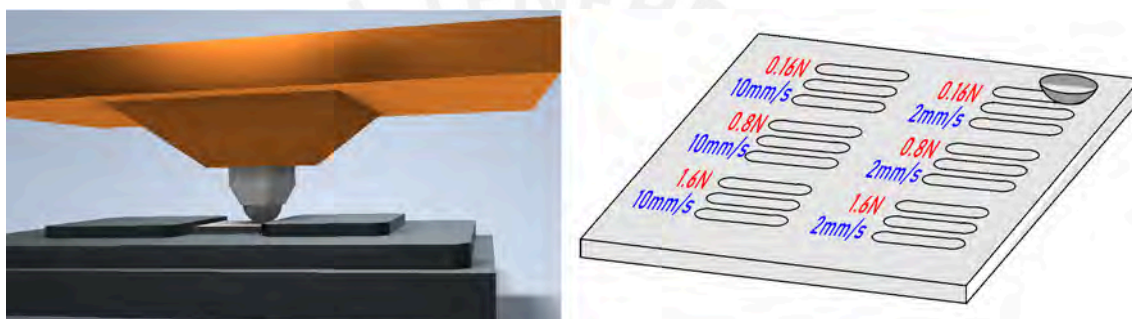


Figure 2.2: Ball-on-flat tribometer schematic and distribution of tracks in each sample.

Depending on the triaxial forces exerted in a walk, an average hip might endure over 2000 N throughout the gait cycle (Ruggiero and Sicilia 2020; Jamari et al. 2022). Based on the Hertzian elasticity contact theory and hip collected gait data *in vivo*, Wang et al. offer a realistic stress level and peak stress analysis at the human hip joint (maximum of 11.89 MPa) (X. Wang et al. 2005). In (Sanders and Brannon 2011), Hertzian contact theory was applied for concentric hip contacts in abnormal states and multiple material couples assuming:

1. The materials are homogeneous, linear elastic, and isotropic.
2. The surfaces are perfectly smooth and frictionless.
3. The surfaces are nonconforming.

4. The contact dimensions are much smaller than the surface radii at the contact point (Hertz, 1882; Johnson, 1985).

The work by Sandres et al. shown that the accuracy of Hertzian contact theory for forecasting contact dimensions in edge loading is dependent on the bearing materials and contact location. Their measures were frequently greater than their expectations in their outcomes. They discovered that contact would press some of the grease slightly past the contact boundary; also, powder particles may attach to the edge of the transfer film. A mean contact pressure of 5.7 GPa for ceramic on ceramic implants.

A hertzian contact pressure analysis in Table 2.1 is used to determine the average contact stress based on values of contact load and probe radius (Chandra et al. 2011). This analysis depends on the normal force (0.16, 0.8 and 1.6 N), radius of the AISI 52100 steel ball (4 mm). Also the the elastic modulus and Poisson's ratio of the steel ball ($E_{ball} = 200GPa$ and $\nu_{ball} = 0.3$), AISI 304 steel ($E_{steel} = 193GPa$ and $\nu_{steel} = 0.29$), Ti_3AlC_2 ($E_{Ti_3AlC_2} = 297GPa$ and $\nu_{Ti_3AlC_2} = 0.2$) and Ti_2AlC ($E_{Ti_2AlC} = 277GPa$ and $\nu_{Ti_2AlC} = 0.19$). The mathematical procedure followed here is described in Quispe et al. 2022 and the results are shown in Table 2.1.

Table 2.1: The hertzian contact pressure for the contact between the AISI 52100 steel ball and a samples plane

Hertzian contact pressure (MPa)	0.16 N	0.8 N	1.6 N
Steel AISI 304	447	765	964
Steel + Si_xN_y + Ti_2AlC	493	843	1062
Steel + Si_xN_y + Ti_3AlC_2	503	861	1085

Coefficient of Friction: Data processing

Due to the presence of noise during changes of direction in the track path, the application of a "Moving Average" filter was proposed. This filter selects a window of values and averages them in order to eliminate the values that move away from the surrounding values. The filter

was used in MatLab and applied on Origin for this thesis work to facilitate the representation of results. The value of the window of values used was 150 because 90,020 measuring points were obtained per COF measurement in each track Figure 2.2.

2.3. Morphological characterization

The coated (AISI 304 steel with Ti-Al-C based MAX phase) and uncoated (steel) samples were characterized at the Materials Characterization Center at Pontificia Universidad Católica del Perú (CAM-PUCP) before and after the tribological.

2.3.1. Scanning Electron Microscope

The Scanning Electron Microscope (SEM) equipment FEI Quanta 650 was used to take images to identify the surface morphological change at an accelerating voltages of 15 kV and a spot of 5. The spot size d50 with this parameters is 170.6 nm. Energy dispersive X-ray spectroscopy (EDX) was carried out on the samples using an EDAX Octane Pro EDX detector installed on the SEM to determine their elemental composition.

The measures before the tribological test were at randoms points (n=2) on the sample surface. After the test, an image of each track (subsubsection 2.2) was taken, and a linescan EDX orthogonal to the track were conducted. Additionally, a collection of points close to the boundaries were measured to identify the wear particles and debris.

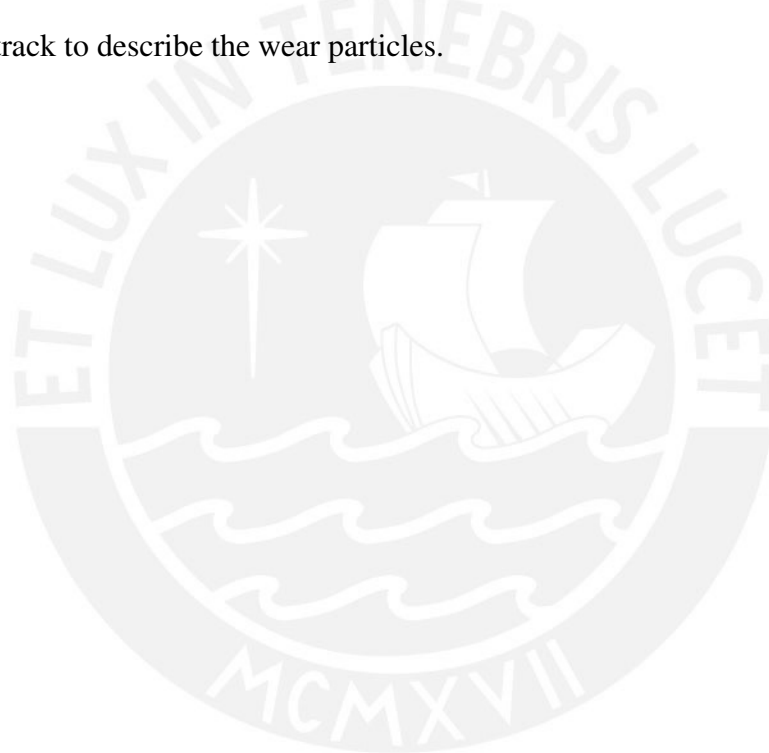
2.3.2. X-Ray Diffraction

X-ray diffraction was performed with a Bruker D8 Discover diffractometer with Cu $K\alpha$ radiation ($\lambda = 1.5406 \text{ \AA}$), an accelerating voltage of 40 kV and a filament current of 40 mA. The patterns were obtained in two configurations: Bragg-Brentano (BB) and Grazing incidence (GI). The GI measurements were performed at a fixed incidence angle of 2° (2θ between 5° - 80°) and a Goebel mirror to obtain a parallel beam. In the BB configuration, measurements

were performed in the 2θ range of 5° - 65° .

2.3.3. Raman Spectroscopy

Raman spectroscopy was performed using a Renishaw inViaT™ Qontor™ micro-Raman inViaT™ confocal microscope. The excitation wavelength was 633 nm (He-Ne laser). The measures before the tribological test were at random points ($n=2$) on the sample surface. Following the test, measurements were taken at the lateral and superior edges of the track as well as inside the track to describe the wear particles.



Chapter 3

Results and discussion

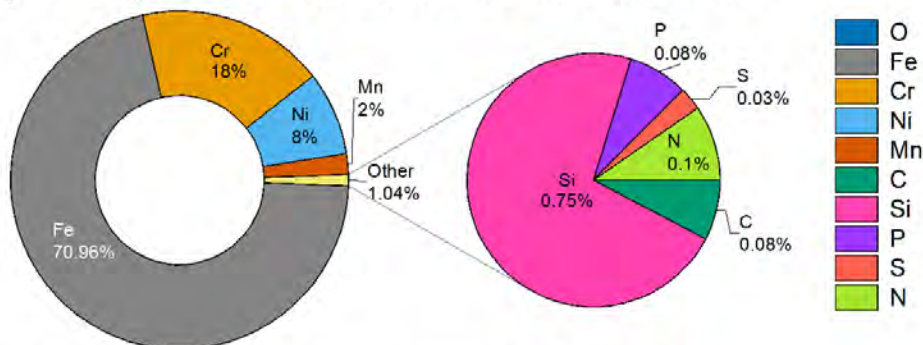
3.1. Morphological characterization prior to the tribological testing

In order to understand the particles composition formed after the wear test by the tribometer contact, all samples were measured by SEM/EDX, XRD and Raman spectroscopy. All techniques provide data on the MAX phase coating and if the steel substrate has been sufficiently penetrated. The use of the Torres et al. preparation method to deposit the Ti_2AlC or Ti_3AlC_2 MAX phase coatings as a solid lubricant on an AISI 304 stainless steel substrate has not before been documented in literature (Torres et al. 2021).

To understand the chemical composition, the EDX data is more useful. In Figure 3.1, to confirm that the steel used was AISI 304, the percentage of chemical elements in the steel sample is displayed and compared to commercial AISI 304. The concentrations of Fe, Cr, Ni, Mn, S, Si, and N are within the predicted limits (AlHazaa and Haneklaus 2020; Borba et al. 2020). The electrolytic solution in the electropolishing (H_3PO_4 , H_2SO_4 and H_2O) might explain the elevated P concentration, as well as the presence of O. Due to self-absorption, low x-ray

fluorescence yields, and detector inefficiency or contamination, the high levels of carbon seem to be present (Buck 2017). The composition is more closely aligned with what is anticipated in AISI 304 overall.

A) Composition of commercial AISI 304



B) Composition of the AISI 304 used

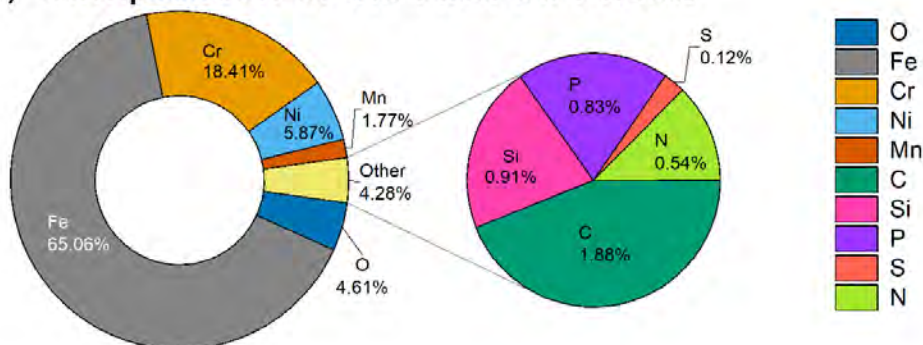


Figure 3.1: Atomic Concentration comparison of standard AISI 304 and the steel substrate used for coated samples. Based on (AlHaza and Haneklaus 2020; Borba et al. 2020)

In the Figure 3.2, the composition of the coated samples is shown. To be able to attribute the chemical composition to the corresponding MAX phases, in Figure 3.2, the ratio of Ti:Al and C:Al of the samples is compared. According to the stoichiometry of the MAX phases a Ti:Al ratio of 2:1 for Ti_2AlC and 3:1 for Ti_3AlC_2 is expected whereas the C:Al ratio is 1:1 or 2:1, respectively. The Ti-Al-C relation is around 2.41:1:1.23 at 700°C, showing an slightly increased Ti and C concentrations. This might indicate that Ti_2AlC is partially formed. Additionally, since the high acceleration voltage employed in EDS makes it difficult to detect nitrogen, the high Si

concentration supports the creation of the diffusion barrier Si_xN_y . (15 KV).

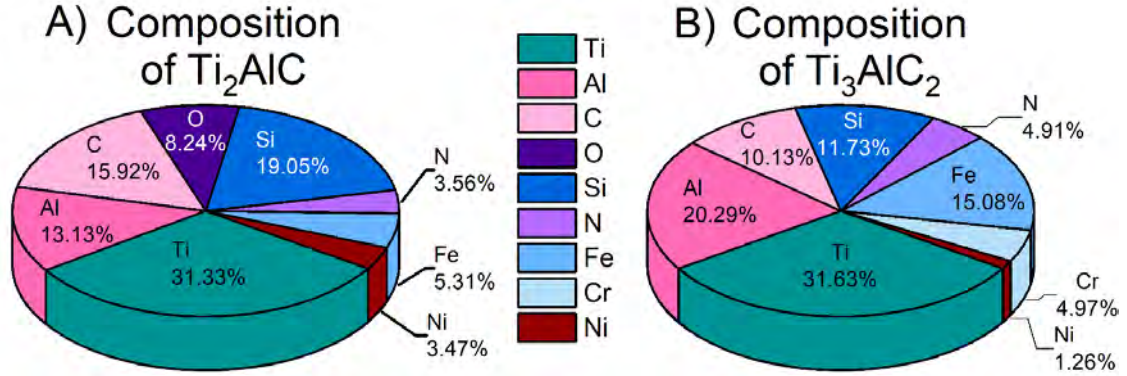


Figure 3.2: Atomic Concentration of selected elements found in the MAX phase coated samples.

In the case of 950 °C, the Ti-Al-C relation is around 1.56:1:0.50. This shows a significant presence of Ti and Al in comparison to C. And it might evidence the formation of Ti_3AlC_2 with co-products like Al_2O_3 or TiO_2 when oxygen is present (the absent of oxygen in Figure 3.2 could have avoid retention of Ti and Al), that avoids the interaction of C with Ti or Al. Also, the present of Cr, Ni and mainly Fe evidence that the substrate is the steel previously described.

Table 3.1: High intensity peaks location found for Ti_2AlC , Ti_3AlC_2 , Fe-Austenite and aluminum oxide. Adapted from:(Zandrahimi et al. 2007; Ansari and Husain 2011; Karunakaran, Anilkumar, and Gomathisankar 2011; L. Wang and Sun 2013; Quan and He 2015; Sanati, Raeissi, and Edris 2017; Abdo et al. 2021; Torres et al. 2021; Naeem et al. 2022; Quispe et al. 2022)

Peaks positions [°]			
Ti_2AlC	Ti_3AlC_2	Fe-Austenite	Al_2O_3
13.32	9.59	43.33	27.20
34.50	19.30	50.50	29.20
39.48	36.50	74.43	
53.50	38.50	90.45	
71.80	83.50		
85.50	42.00		

The XRD results in Figure 3.3 were used as a reference to identify whether the coatings were MAX phases and to verify if the substrate was AISI 304. Table 3.1 includes a list of

the expected peaks to be identified (without their corresponding Miller indices of the crystallographic planes). First the identification of the AISI 304 in the steel sample are noted with black lines (γ). These peaks refer to the presence of Fe-austenite, which is typical for AISI 304 (Zandrahimi et al. 2007; L. Wang and Sun 2013; Quan and He 2015; Sanati, Raeissi, and Edris 2017; Abdo et al. 2021; Naeem et al. 2022). In this thesis, the presence of austenitic iron is used as a steel fingerprint in samples with MAX phase coatings. These last 4 peaks of the XRD diffractogram are similar to the steel fingerprint of the reference in black in all samples.

X-Ray Diffraction previous to Tribological tests

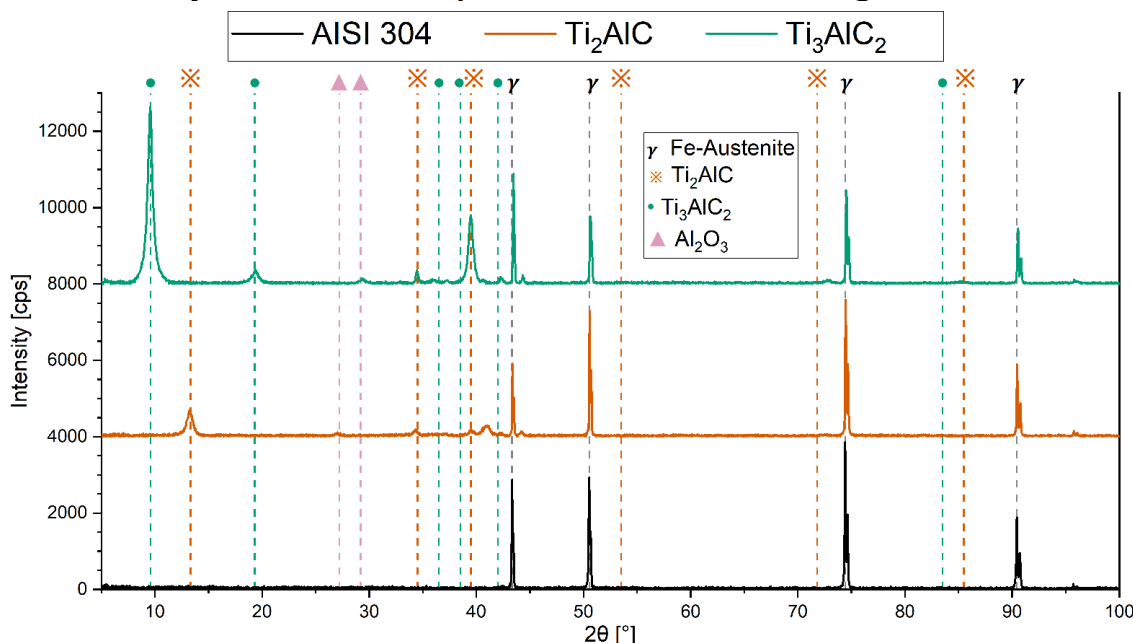


Figure 3.3: Bragg Brentano configuration-X-Ray diffraction patterns of AISI 304 stainless steel, MAX Ti_2AlC at 700°C MAX and Ti_3AlC_2 at 950°C

In (Quispe et al. 2022), the peaks found for the Ti_2AlC coating over Si_xN_y (as substrate) using the technique elaborated in (Torres et al. 2021) were at $2\theta = 13.30^\circ$ and $2\theta = 34.50^\circ$ (marked with orange lines). These peaks, along with $2\theta = 39.48^\circ$, shown in the sample diffractogram corroborate the formation of a Ti_2AlC coating in Figure 3.3 (after being heated at

700°C). The remaining peak over $2\theta = 40^\circ$ may be a consequence of a shifting due to different expansion/contraction of the coating and substrate.

For the sample heated at 950°C (Ti_3AlC_2), the peaks found at $2\theta = 9.59^\circ$ and $2\theta = 19.30^\circ$ had the positions as expected for Ti_3AlC_2 (marked with green lines). The peaks at $2\theta = 34.50^\circ$ and $2\theta = 39.48^\circ$ peak are described in Table 3.1 for Ti_2AlC . Those peaks could be a consequence of shifting to the left for lattice expansion of the diffusion barrier o coating, or the formation of Ti_2AlC due to heat treatment close to 950°C (Lee 2016; Torres et al. 2021).

Finally, the presence of aluminum in the coating together with oxygen results in minor depositions of Al_2O_3 evidence in the peaks about $2\theta = 27^\circ$ and $2\theta = 28^\circ$ (marked with pink lines in Figure 3.3). The oxygen is probably provided during the heating process. This aluminum oxide is frequently present during the synthesis of Ti_2AlC , and it is also needed to enhance the coating's oxidation resistance (Haftani et al. 2016). The full list of high peaks intensity is found in Table 3.1.

Table 3.2: High intensity peaks location in Raman spectrum of Ti_2AlC , Ti_3AlC_2 , aluminum oxide and graphite. Adapted from: (Presser et al. 2012; Rao, Pierce, and Dasgupta 2014; Torres et al. 2021)

Compound	Wavenumbers (in ω cm^{-1})						Reference
Ti_2AlC	153.3	260.9	270.3	358.7			(Presser et al. 2012)
	149.9	262.1	268.1	365.1			(Torres et al. 2021)
Ti_3AlC_2	125.0	183.4	201.5	270.2	623.2	663.3	(Torres et al. 2021)
Al_2O_3	300.0	381.0	567.0	711.0			(Torres et al. 2021)
graphite	1340.0	1590.0		293.0			(Rao, Pierce, and Dasgupta 2014)

According to (Spanier et al. 2005; Presser et al. 2012), the wave numbers (cm^{-1}) expected for bonds of Ti-Al, Al-C and Ti-C in Ti_2AlC are expected at 149.9 cm^{-1} , 262.1 cm^{-1} , 268.1 cm^{-1} and 365.1 cm^{-1} (Table 3.2). The results in Figure 3.4 for the bonds in Ti_2AlC , only have a peak at 270.3 cm^{-1} and 358.7 cm^{-1} which means that the coating had indeed Ti_2AlC , but the peak at 623.2 also proves that there is a notorious presence of Ti_3AlC_2 (both MAX phases in

the same coating). For the sample treated at 950°C which is expected to have Ti_3AlC_2 , have its 3 major peaks where the Ti_3AlC_2 peaks appear (Table 3.2). On the other hand, there is evidence that the presence of oxygen may create small formations of Al_2O_3 , and graphite may be inside the substrate due to the electrolytic solution and posterior temperature treatment.

According to the results, the coatings composition is predicted to conform to the composition of Ti_2AlC or Ti_3AlC_2 MAX phases.

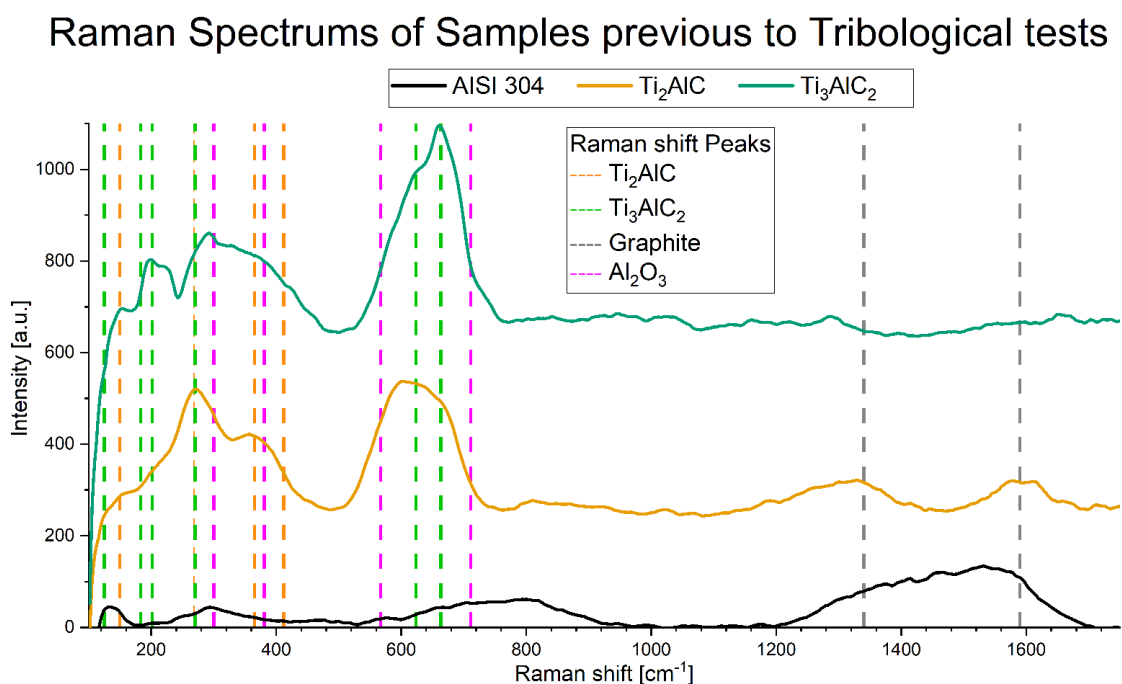


Figure 3.4: Raman spectrums of AISI 304 stainless steel, MAX Ti_2AlC at 700°C MAX and Ti_3AlC_2 at 950°C

3.2. Tribological test of coefficient of friction by variations of normal force and speed

The objective of the tribological testing was to determine how the coefficient of friction changed as a function of the normal forces (0.16 N, 0.8 N, and 1.6 N) and speed (2 mm s^{-1} and 10 mm s^{-1}) at which the ball moved back and forth against the flat surface. The low speed test had a sliding path length of about 1.8 m, while the higher speed test had a sliding path length of 9 m due to the test fixed duration of 15 minutes for each track. According to the literature, the COF for AISI 304 against AISI 52100 is around 0.7-0.8 due to variations in the measure like tribometer set up, normal force and counter part material (Arash et al. 2015; Dogan, Findik, and Oztarhan 2003; Qin et al. 2018; Dib et al. 2020). In Table 3.3, a summary of the values of the tribological test presented in section 3.2.

Table 3.3: Coefficients of friction of Ti_2AlC , Ti_3AlC_2 and AISI 304 at combinations of the normal forces (0.16 N, 0.8 N, and 1.6 N) and speed (2 mm s^{-1} and 10 mm s^{-1}).

	2 mm s^{-1}			10 mm s^{-1}		
	0.16 N	0.8 N	1.6 N	0.16 N	0.8 N	1.6 N
Steel	0.85	0.78	0.77	0.85	0.8	0.65
Ti_2AlC	0.52	0.73	0.68	0.72	0.74	0.72
Ti_3AlC_2	0.15	0.14	0.13	0.14	0.14	0.14

3.2.1. Results at 2 mm s^{-1}

At 2 mm s^{-1} and 0.16 N

The visible wear particles in this test are fewer than what is shown in the upcoming results at the same minimum speed and normal force (Figure 3.5). At the beginning of the tribological experiment the COF of AISI 304 against AISI 52100 was 0.6 due to the running-in, but it

stabilizes around 0.85 (upper 75% quantile), which is the average for this steel. This running-in affects the COF of all AISI 304 tested, but it was previously reported that this AISI 304 have this behavior (Dib et al. 2020). It must be considered that this steel had a high COF, but even the AISI 316L have a COF not lower than 0.75 with running-in behavior (Dogan, Findik, and Oztarhan 2003). The wear particles are not only a combination of the steel and the coating, but also the elements of the AISI 52100 from the ball counterpart, which is known to have more iron and less chromium. The AISI 52100 (against AISI 304) has proven to be that predominant source of wear due to its delamination (Zandrahimi et al. 2007).

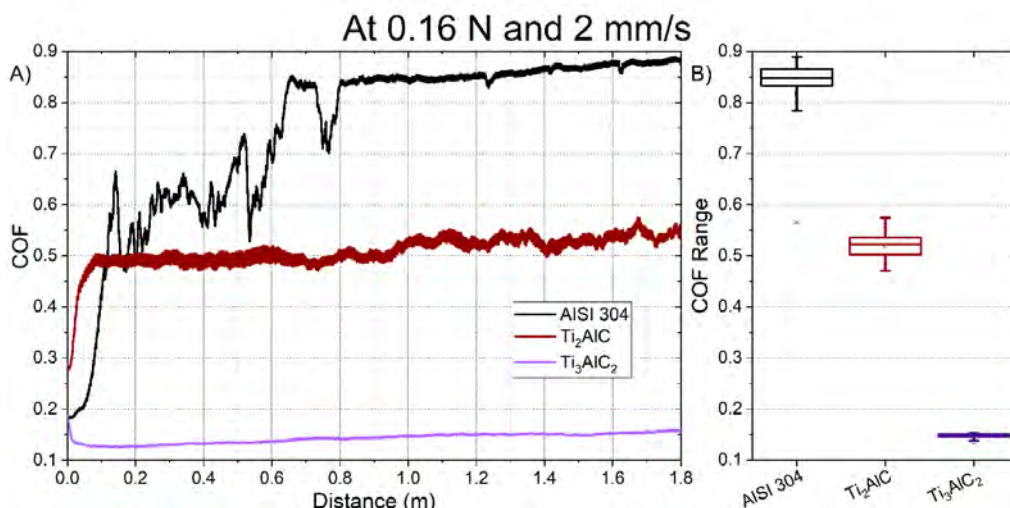


Figure 3.5: COF analysis for Steel, Ti_2AlC and Ti_3AlC_2 at 2 mm s^{-1} and 0.16 N .

The Ti_2AlC coating had a stable COF around 0.52, and it also had running-in behavior as evidenced by the production of wear debris surrounding the track, which served as lubrication in part (due to minor delamination). The image of the track in Figure 3.6 shows a track with a width around $200\ \mu\text{m}$ with a slight formation of wear around. A cross-section linescan demonstrates that friction causes a wear mark in the center of the track (about $135\ \mu\text{m}$), where the wear of the Ti_2AlC coating is demonstrated by a loss of more than half of Ti and the wear of the barrier diffusion by a decrease of Si (from 13% to 7%). Also the dark marks in the SEM image is steel

since its levels duplicate itself where the coating wear was higher (double Fe and Cr). The peak of oxygen at 125 μm is a consequence of the accumulation of oxides at the border, which were removed from the inside of the track (oxygen absent from 125 μm to 165 μm).

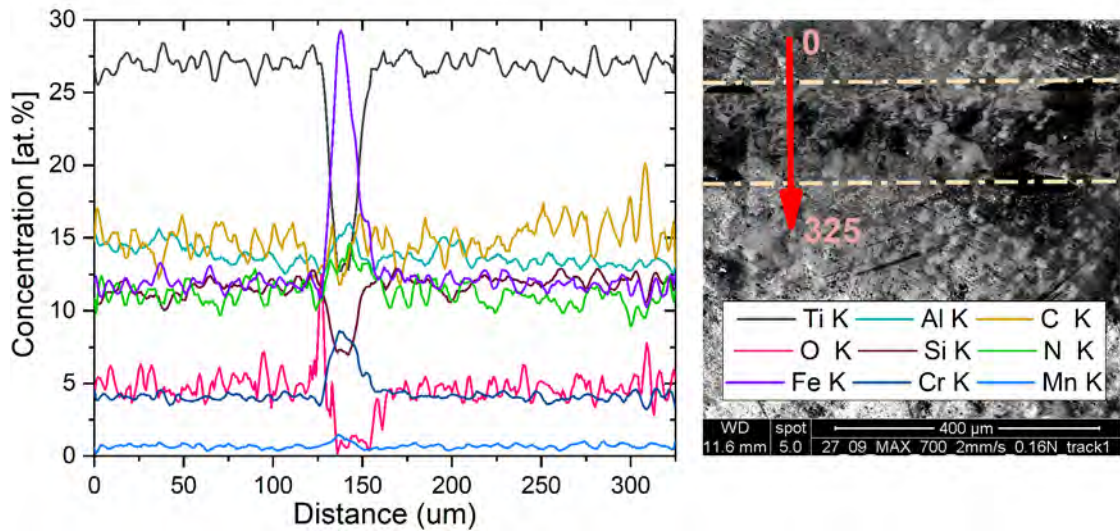


Figure 3.6: Scanning electron microscope-energy dispersive X-Ray detector (SEM-EDX) analysis of Ti_2AlC at 15 kV. SEM micrographs of the wear track at 2 mm s^{-1} and 0.16 N. The orange dashed line shows the position of the wear track.

In Figure 3.7, the wear particles surrounded the borders of the tracks seems to be mainly consequence of steel delamination. The points around the laterals of the track (point 2 and point 3) have slightly lower levels of Ti and Al with higher levels of Fe and C. The presence of Ti_2AlC is probably a consequence of the delamination of the lubrication coating. Not only the MAX phase coating was removed, but also the the AISI 52100 counterpart is the provider of steel traces accumulated at the borders from its own delamination. The points inside the great accumulation of wear particles (points 6 and 7) have a composition similar to the previous mentioned. The points further from the border are marks of visible wear accumulations. Point 1 shows a highly oxidation of steel and Ti with almost no presence of Ti_2AlC . The remain points 4 and 5 have the highest levels of oxides, but much less accumulation of steel in comparison to

other points. In general, most of steel in this track comes from the counterpart with zones of high delamination of the coating that protects the surface from the friction working as a solid lubricant.

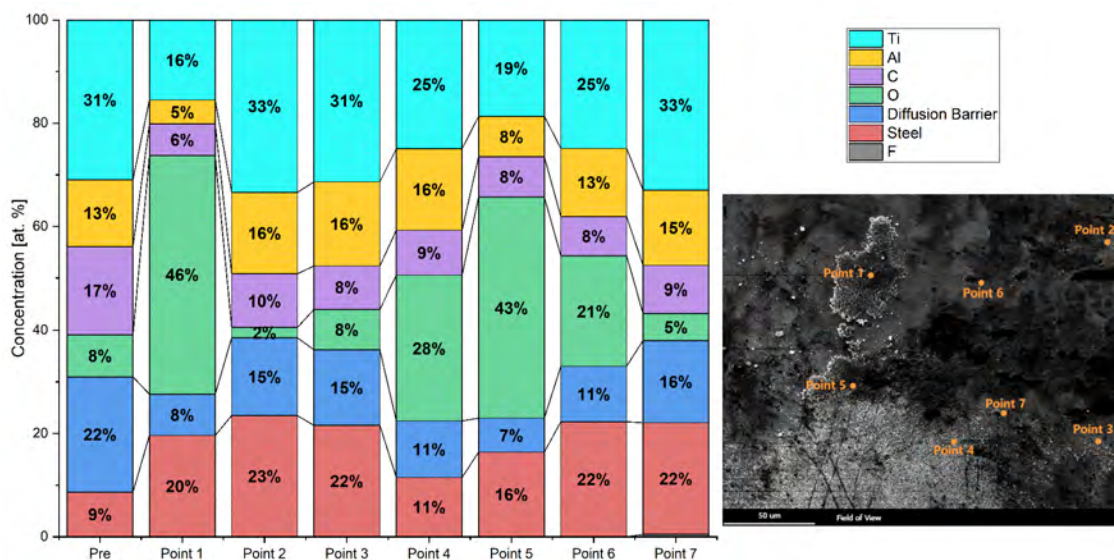


Figure 3.7: EDX points analysis on the scanning electron microscope (SEM) images of Ti_2AlC wear particles around a wear track at 2 mm s^{-1} and 0.16 N .

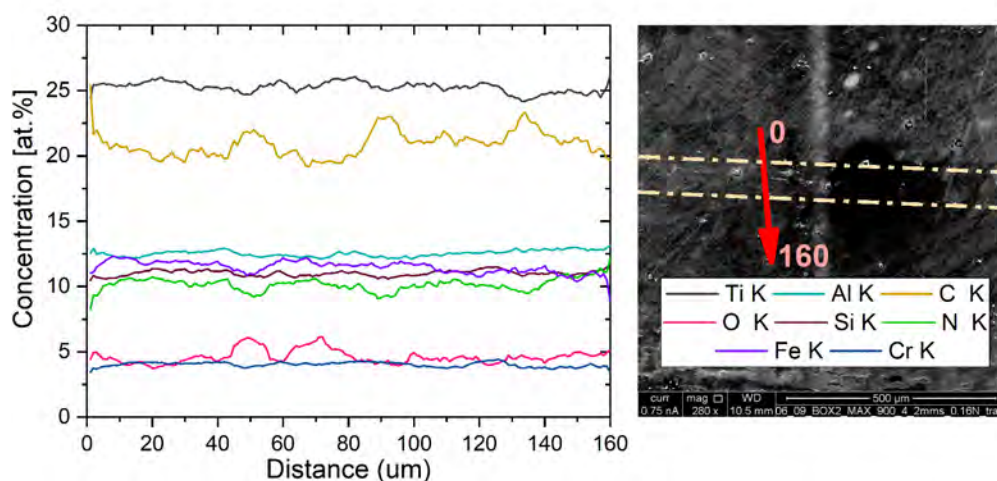


Figure 3.8: Scanning electron microscope-energy dispersive X-Ray detector (SEM-EDX) analysis of Ti_3AlC_2 at 15 kV . SEM micrographs of the wear track at 2 mm s^{-1} and 0.16 N . The orange dashed line shows the position of the wear track.

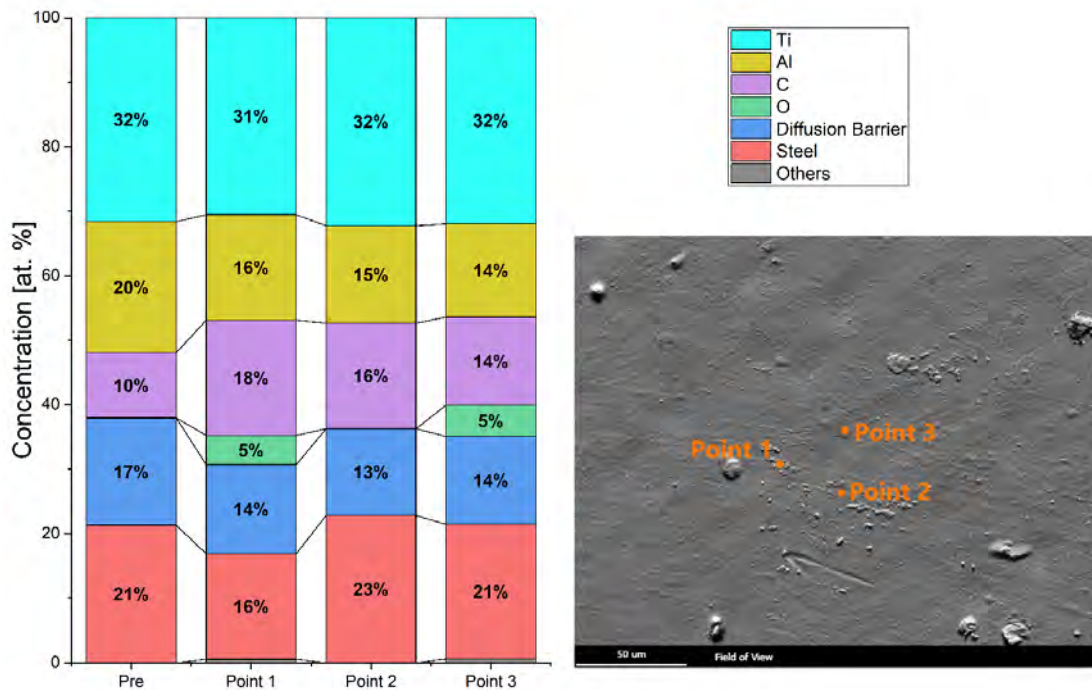


Figure 3.9: EDX points analysis on the scanning electron microscopy (SEM) images of Ti_3AlC_2 wear particles around a wear track at 2 mm s^{-1} and 0.16 N .

Out of what it was expected, Ti_3AlC_2 had different behavior with the lowest COF at 0.15, with a running-in behavior. This running-in behavior may be consequence of a well done delamination, where the wear from the coating is shaped like leaves over the tracks and then it became a protection for this track. The SEM image in Figure 3.8 shows an almost non visible track, where the wear particles are almost unnoticeable, but the track is highlighted by orange lines. The track had an approximated width of $40 \mu\text{m}$. Ti_3AlC_2 was not affected except for the small accumulation of carbon at the borders, probably for the wear of graphite byproducts evidenced in Figure 3.3. Elements from the diffusion barrier (silicon and nitrogen) and steel (iron and chromium) had no important variations in its levels, except the slightly decrease on the levels of nitrogen in the borders. The increasing on oxygen is accumulated at the border ($50 \mu\text{m}$) and inside ($70 \mu\text{m}$) of the track due to oxides formation. The change of no more than 4% in all elements are evidence of the absence of wear of the coating or its delamination.

There is no visible sign of wear particles, even at the edges where the ball changes directions, which is thought to be where the majority of the wear occurs. All 3 points seem to have composition similar to the values measure in the Ti_3AlC_2 coated sample before the wear with some accumulation of oxides due to the friction test. In the steel (red bar), chromium had almost no change, but the levels of iron are the main indicator of variations Figure 3.8.

At 2 mm s^{-1} and 0.8 N

At 0.8 N (Figure 3.10), the steel has an uneven COF behavior where the coefficient of friction reach stability around 0.78 . The AISI 304 started with a running-in behavior as mentioned before and it stabilize at 0.8 m . At this conditions, Ti_2AlC have a smoother COF curve with starting at 0.4 , but the wear particles create a constant increasing of COF due to the delamination of the MAX phase coating and the particles of contaminants inside, the COF was similar to the steel, but smoother probably because of the smaller wear residues.

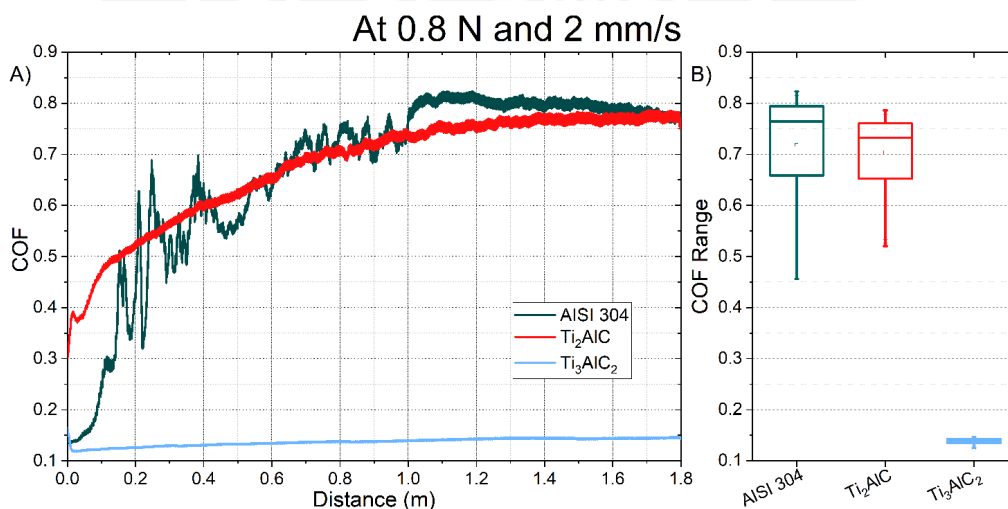


Figure 3.10: COF analysis for Steel, Ti_2AlC and Ti_3AlC_2 at 2 mm s^{-1} and 0.8 N .

The Ti_2AlC coating with COF around 0.78 shows a visible track in the SEM image in Figure 3.11, with a width around $250 \mu\text{m}$ noted with orange lines and also visible wear particles

accumulated in lines. The cross-section linescan highlight two zones: the middle of the track at about $70\ \mu\text{m}$, and the bigger accumulation at the inferior border at about $135\ \mu\text{m}$, where the delamination of Ti_2AlC and AISI 5200 is located. The track is highly oxidized around the center of the track (pink line), but the iron levels rise from 14% to 35% (the Ti levels decrease the same percentage the Fe increases). Carbon has a similar correspondence with Cr as Ti does with Fe at this stage. At $135\ \mu\text{m}$, the values of not only Fe and O increase, but also the presence of Ti. As the chromium level nearly did not grow, the levels of steel from the AISI 5200 are lower than within the track, and yet this zone now contains the majority of the MAX coating and steel wear particles.

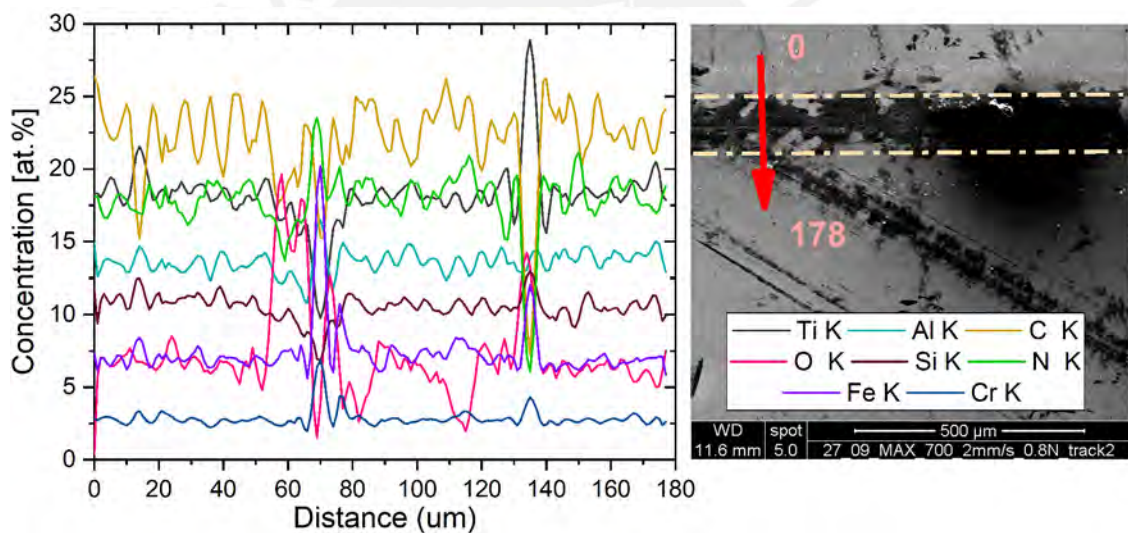


Figure 3.11: Scanning electron microscope-energy dispersive X-Ray detector (SEM-EDX) analysis of Ti_2AlC at 15 kV. SEM micrographs of the wear track at $2\ \text{mm s}^{-1}$ and 0.8 N. The orange dashed line shows the position of the wear track.

Since the wear particles are visible Figure 3.12, the halo of particles formed around all the track is represented by the points 1, 2 and 7. These points are almost similar to the Ti_2AlC before the friction test, but have replaced more than half of the diffusion barrier (Si_xN_y) with residuals of steel particles. They also do not include any oxides. Points 3, 4, 5, and 6 differ from each other because they represent distinct regions of the track. The point 5 is inside the track,

which has values similar to the previous points, but has replaced part of its titanium with oxides (TiO_2 or Al_2O_3). Points 3 and 4 appear to be comparable particles retrieved from the track and have similar compositions with severe oxidation (around 30%). At last, point 6 is a visible wear particles isolated that have less oxidation than point 4. Even when the wear is severe in some points, all still have residual accumulation of Ti_2AlC .

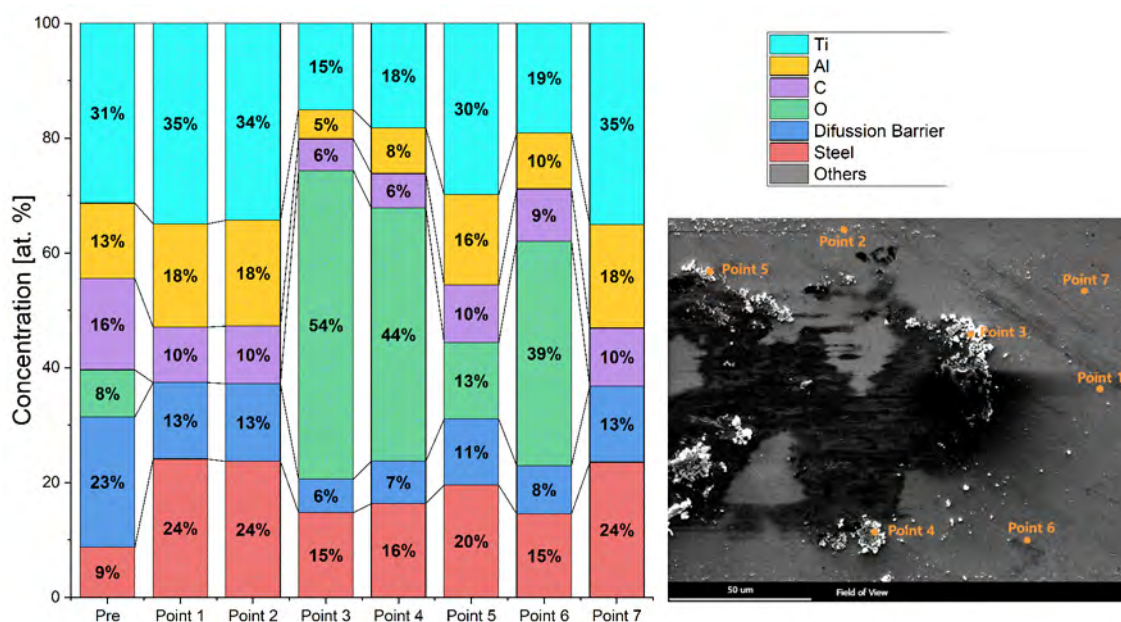


Figure 3.12: EDX points analysis on the scanning electron microscopy (SEM) images of Ti_2AlC wear particles around a wear track at 2 mm s^{-1} and 0.8 N .

Ti_3AlC_2 kept an steady COF of 0.15, which could mean almost no wear formation. Compared to the track at 0.16 N , the track in the SEM image in Figure 3.13 is more visible. However, the linescan quantification does not show noticeable variations in the levels of Ti (black line) or Fe (pink line). In this track, the visible marks are around $45\text{ }\mu\text{m}$ and $85\text{ }\mu\text{m}$. The only variations in that range are a decreasing of carbon and a corresponding increasing in the oxygen levels. The oxides formed are assumed to be Al_2O_3 , or TiO_2 in small amounts.

Even when the linescan does not show a variation in the crosssection, the SEM image in Figure 3.14 shows the wear of the coating and residues of the delamination of both AISI 52100

and Ti_3AlC_2 coating. A point inside the track (point 4) has the same composition as a point outside the track (point 5), and both have the same composition as the measurement before the wear. The most evident sign of wear is border delamination. The coating and diffusion barrier appear to have been torn off of Point 1, leaving only the steel substrate. According to the literature, a tribometer with a reciprocating action wears more at its border than other rotatory possibilities such as a pin-on-disk. This disk layout produces a continuous wear pattern with no wear zones (such as the interior of the track). More pressure and deeper penetration are created when the pin or ball changes direction by changing its speed. Other remnants, such as points 2 and 3, appear to be laminates peeled off of the steel and hence contain intact compositions.

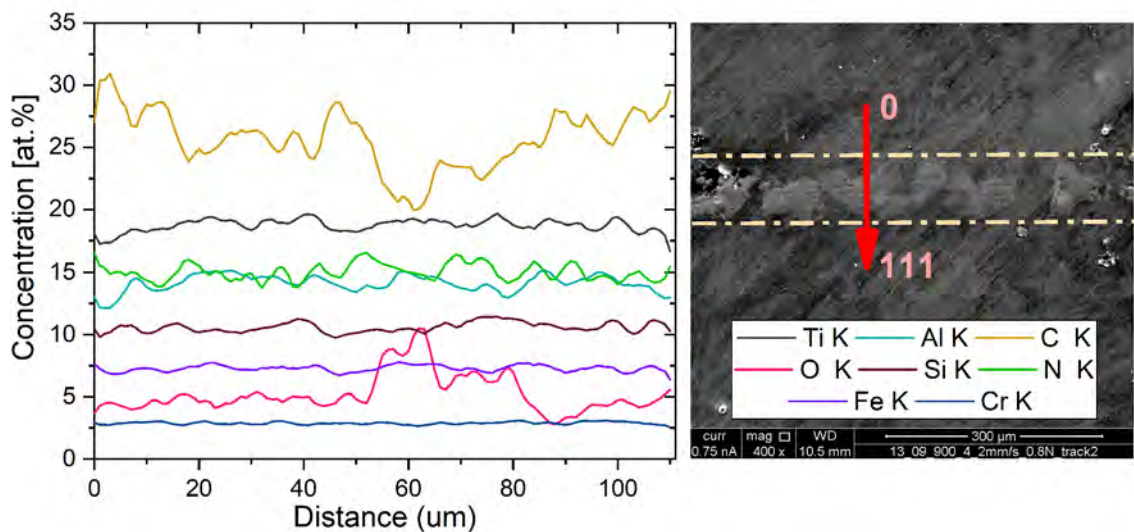


Figure 3.13: Scanning electron microscope-energy dispersive X-Ray detector (SEM-EDX) analysis of Ti_3AlC_2 at 15 kV. SEM micrographs of the wear track at 2 mm s^{-1} and 0.8 N. The orange dashed line shows the position of the wear track.

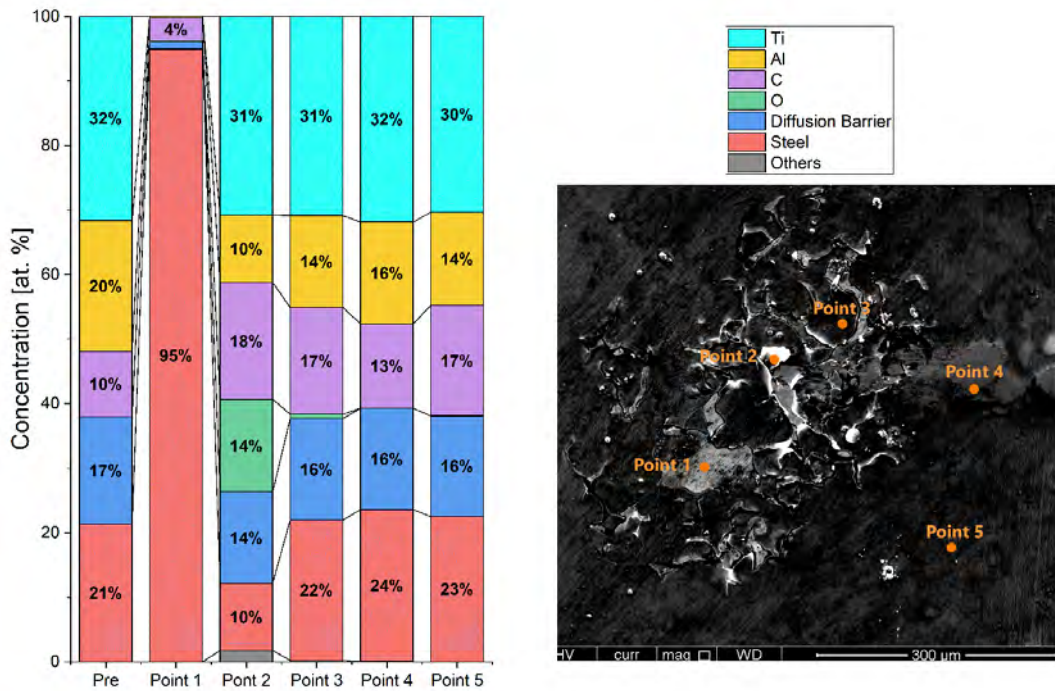


Figure 3.14: EDX points analysis on the scanning electron microscopy (SEM) images of Ti_3AlC_2 wear particles around a wear track at 2 mms^{-1} and 0.8 N .

At 2 mms^{-1} and 1.6 N

At the 2 mms^{-1} speed with the highest normal force used of 1.6 N (Figure 3.15), the steel have a larger running-in behavior, reaching an stable COF of at 1.4 m behavior as in 0.8 N before, but with a maximum COF of 0.77 . At this higher force the coefficient of friction it is expected to decrease like in (Chowdhury et al. 2013), where a pair AISI 304 with mild steel showed an small reduction of its COF by increasing the force at a steady speed. This explains why the steel did not reach a COF closer to 0.8 like in literature, instead it had a slow start near to the constant COF values of Ti_3AlC_2 over AISI 304.

The Ti_2AlC sample had a high COF around 0.68 because it seems that MAX phase coating was broke since the start. In the Raman Spectrum in Figure 3.16, it is shown the analysis of the borders of the track (lateral and superior) and the inside. The shift of the peak near to

663.3 cm^{-1} (peak of a Ti-C bond in Ti_3AlC_2) could mean a perturbation in the expansion rate during the heat treatment at 700°C to produce the MAX phase coating. It is also remarkable that this peak is reduced in the lateral where the accumulation of the Ti_2AlC is minimum. The point inside the track showed small peaks of Ti_2AlC and no sign of graphite, probably only steel is left since here is where the wear of the coating is expected. It must be remarked that the graphite presence is a consequence of using a graphite target (source of the C) (Li et al. 2018).

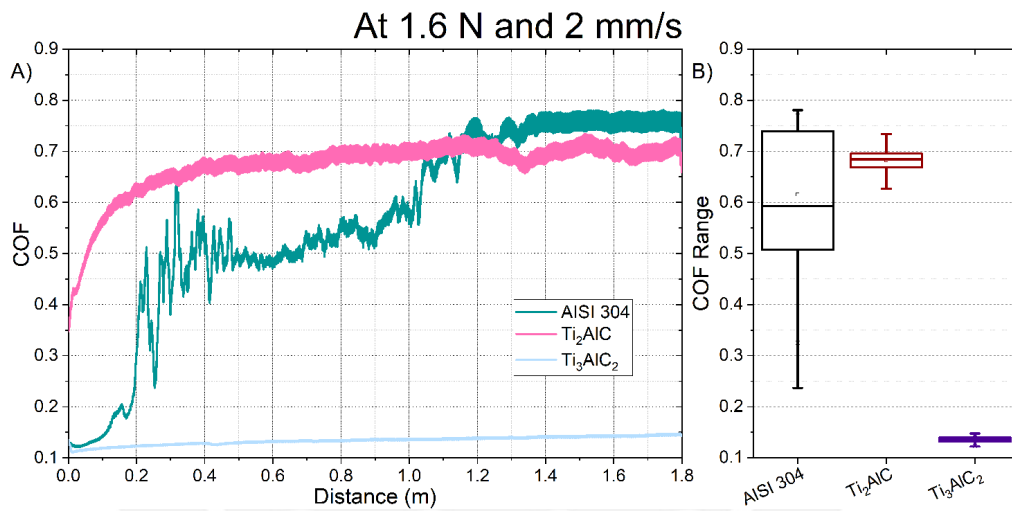


Figure 3.15: COF analysis for Steel, Ti_2AlC and Ti_3AlC_2 at 2 mm s^{-1} and 1.6 N .

To contrast the results in the inside (red Raman spectrum in Figure 3.16, the linescan provides useful complementary information. The SEM image in Figure 3.17 evidence a visible track from $90\ \mu\text{m}$ to $160\ \mu\text{m}$. At $40\ \mu\text{m}$, an oxide presence replaces small amounts of Ti and Cr, but increases presence of C. The fraction of Ti is lowered inside the track without impacting Al or C. Because of the presence of steel, AISI 52100 ball delamination residues remain inside the track without damaging the Si_xN_y diffusion barrier.

To verify the values in the lateral (blue Raman spectrum in Figure 3.16), 10 points were analyzed at the lateral border of the track (Figure 3.18). The bulk of the MAX coating and even the diffusion barrier have been removed from the steel sheet that is visible inside this track

(point 1) and seems to be highly oxidized (steel from the substrate and the ball). Point 8 is on the opposite side of the same wear accumulation. Point 8 has a high quantity of oxides but also contains Ti, Al, C, and a portion of Si_xN_y . The locations closest to the border (points 2, 3, 4, and 5) have lowered Si and N, and replaced them with steel. The particle at point 10 is comparable in composition to the border. Also, the points in the halo of wear around the track (points 5, 6, and 7) have the same composition as the point inside the track. In general all point have high levels of steel (mainly from the AISI 52100 ball) as a consequence of the delamination of the steel ball. Most of the particle of Ti_2AlC seems to still be protecting the surface.

The Ti_3AlC_2 had a steady COF around 0.13. Its Raman spectrum in Figure 3.19 evidence the presence of Ti_3AlC_2 and graphite at the borders (lateral and superior) and inside the track. In contrast to Ti_2AlC (Figure 3.16), the presence of bonds in Ti_3AlC_2 is still strongly evident at all borders. At the superior border, the accumulation of Ti_3AlC_2 seems to be even greater than before the test. Also, all borders have greater accumulation of graphite. The presence of the peak in 365.1 cm^{-1} represents a bond in Ti_2AlC . This peak is sharper in the borders.

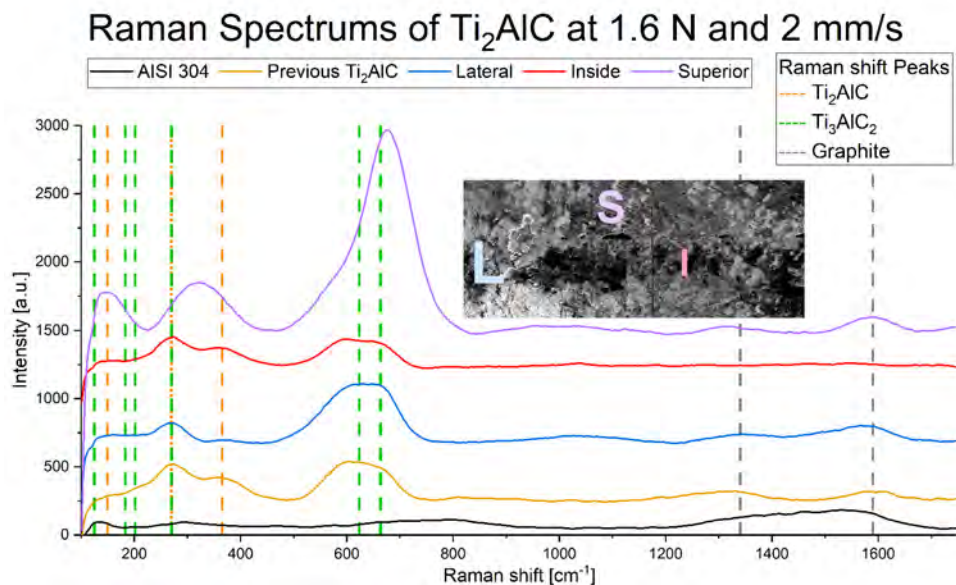


Figure 3.16: Raman spectrums of Ti_2AlC at 700°C MAX at 2 mm s^{-1} and 1.6N , where the wear was maximum.

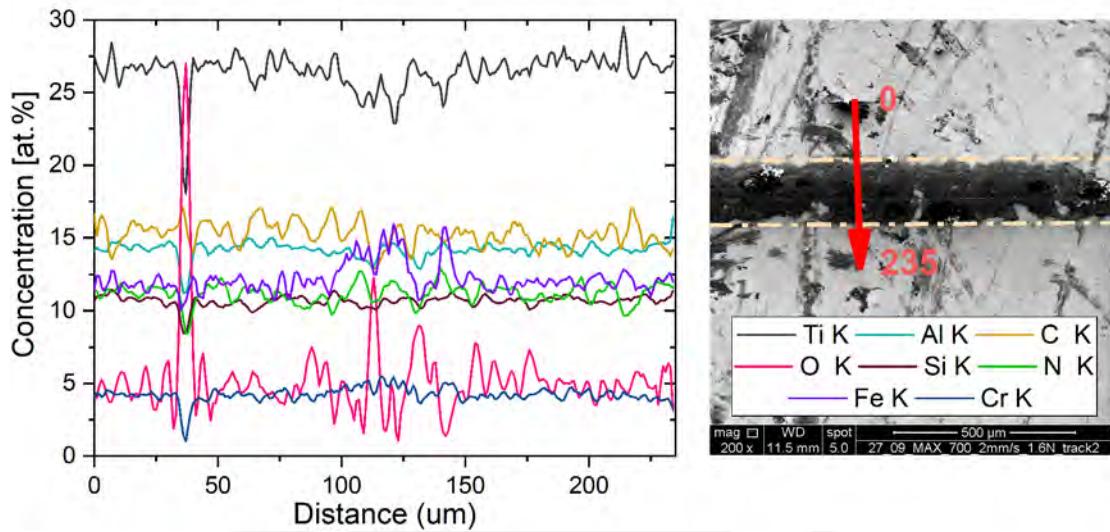


Figure 3.17: Scanning electron microscope-energy dispersive X-Ray detector (SEM-EDX) analysis of Ti_2AlC at 15 kV. SEM micrographs of the wear track at 2 mm s^{-1} and 1.6 N . The orange dashed line shows the position of the wear track.

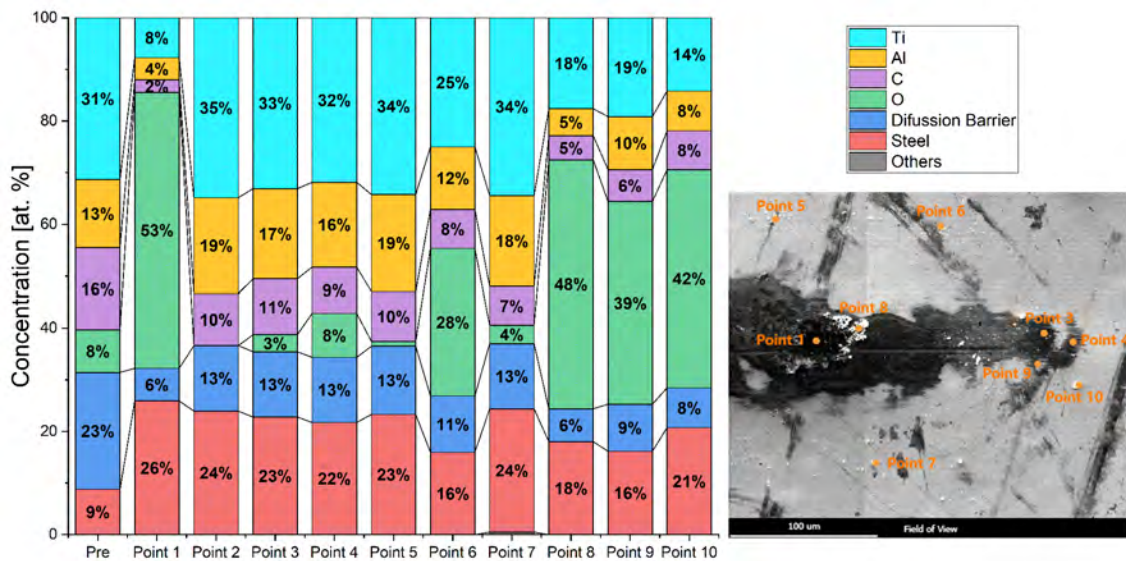


Figure 3.18: EDX points analysis on the scanning electron microscopy (SEM) images of Ti_2AlC wear particles around a wear track at 2 mm s^{-1} and 1.6 N .

The SEM image in Figure 3.20 shows a track with a width of $25\text{ }\mu m$. This track have an reduction of Ti and Si, with a respective complementary increasing of Fe and C. At the

superior border (purple spectrum in Figure 3.19), there is visible particles accumulation but not a noticeable variation of the elements presence besides reduction of C. The MAX phase coating seems to not be destroyed and the steel presence is from the AISI 52100 ball. In the image, it is not easy to notice the wear track marks without the orange lines. The absent of marks of coating wear, except of the zones where the coating was delaminated, are evidence of a protective behavior of the Ti_3AlC_2 coating as a solid lubricant. Its lubrication behavior was described before as a delamination process. In the literature, Ti_2AlC has a lower COF than Ti_3AlC_2 as Silicon coating. In this work, Ti_3AlC_2 has better behavior over a substrate of AISI 304 because it does not peels off as easily as Ti_2AlC .

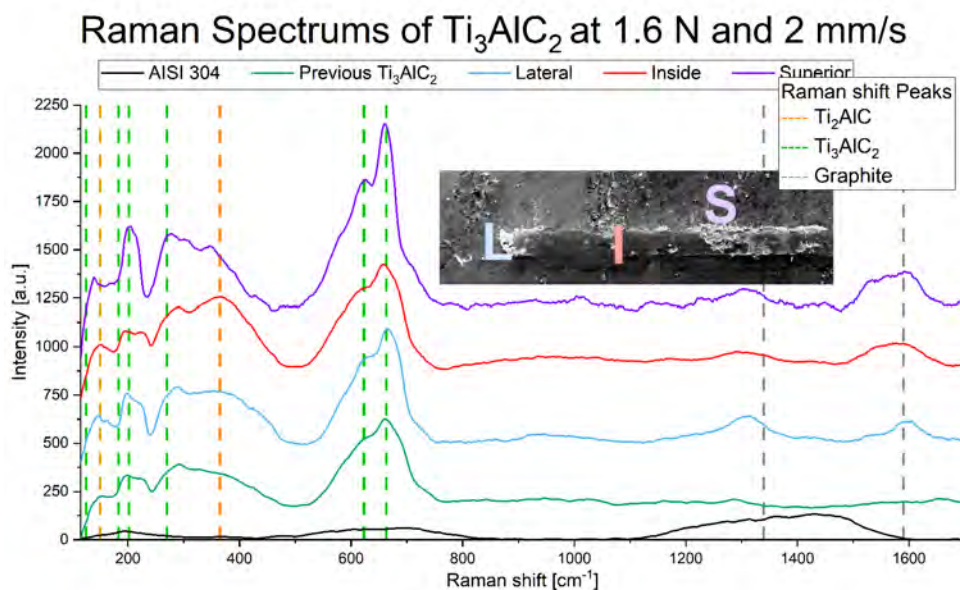


Figure 3.19: Raman spectrums of Ti_3AlC_2 at $950^\circ C$ MAX at 2 mm s^{-1} and 1.6 N , where the wear was maximum

At the border, four point were measure to analyze the wear particles composition (Figure 3.21). The point 1 seems to be the AISI 304 under the coating, the wear in this zones might be a consequence of the change of directions of the AISI 52100 ball. The point 2 is in a wear residues accumulation of Ti_3AlC_2 . Point 3 have residues of K, Na and Cl due to contamination.

Even when point 1 and 4 have high levels of steel, their sources are different since point 4 is a particles from the ball with high oxidation and carbon.

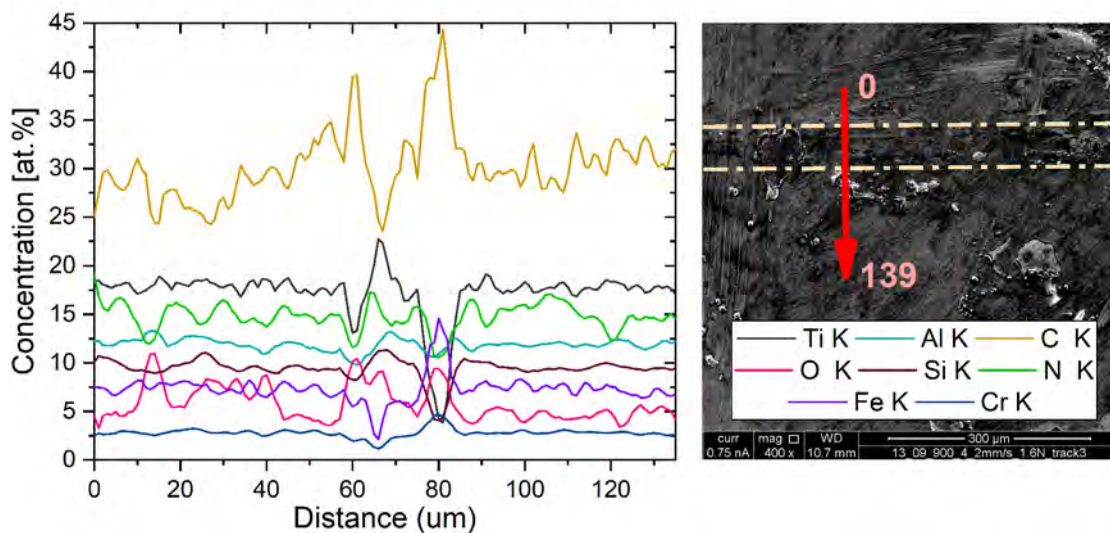


Figure 3.20: Scanning electron microscope-energy dispersive X-Ray detector (SEM-EDX) analysis of Ti_3AlC_2 at 15 kV. SEM micrographs of the wear track at 2 mm s^{-1} and 1.6 N. The orange dashed line shows the position of the wear track.

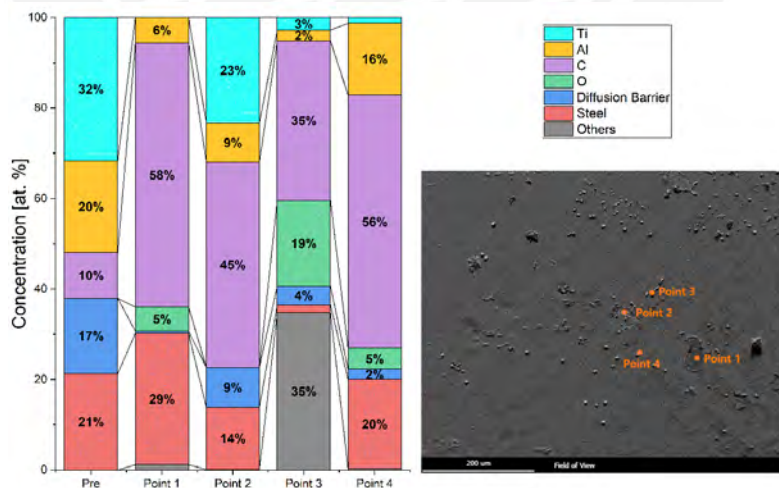


Figure 3.21: EDX points analysis on the scanning electron microscopy (SEM) images of Ti_3AlC_2 wear particles around a wear track at 2 mm s^{-1} and 1.6 N.

3.2.2. Results at 10 mm s^{-1}

At 10 mm s^{-1} and 0.16 N

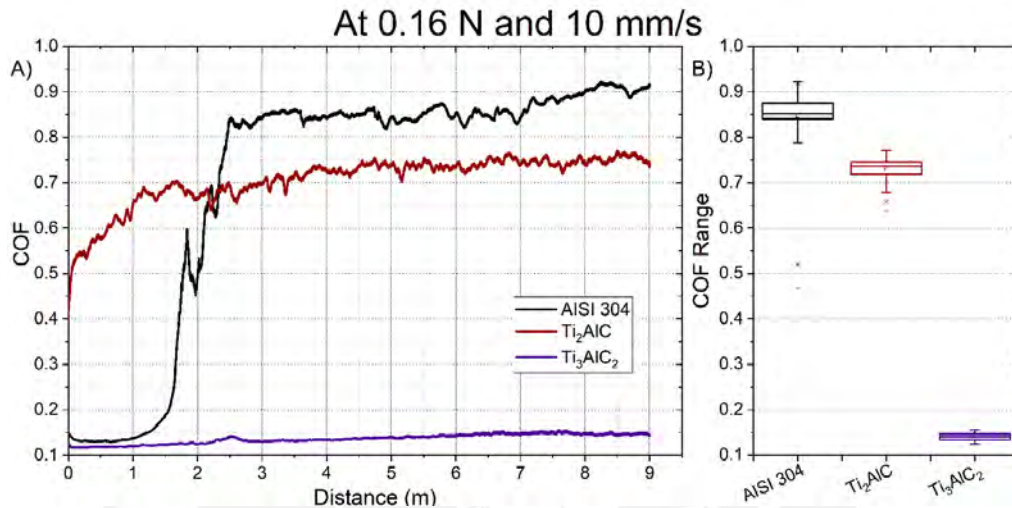


Figure 3.22: COF analysis for Steel, Ti_2AlC and Ti_3AlC_2 at 10 mm s^{-1} and 0.16 N .

The COF of AISI 304 reach is higher value at 10 mm s^{-1} and 0.16 N in Figure 3.22, a COF of 0.85. Now that the distance has increase to 9 m, the running-in phase is only presence for the first 2 m. The BOX graph in Figure 3.22 provides a better vision of the COF curves avoiding the running-in effect of the final COF. All COF have more stable values than at 2 mm s^{-1} .

The track of Ti_2AlC is even more visible than at 2 mm s^{-1} , in Figure 3.23 is shown a track with a width around 100 mm. The previous relation of reduction of Ti and increasing of Fe is also evident. The presence of Fe from the steel, and the reduction of Si from the diffusion barrier, are evidence of a wear of the coating which is why this sample reach a high COF around 0.8. There is also an accumulation of oxides besides the track.

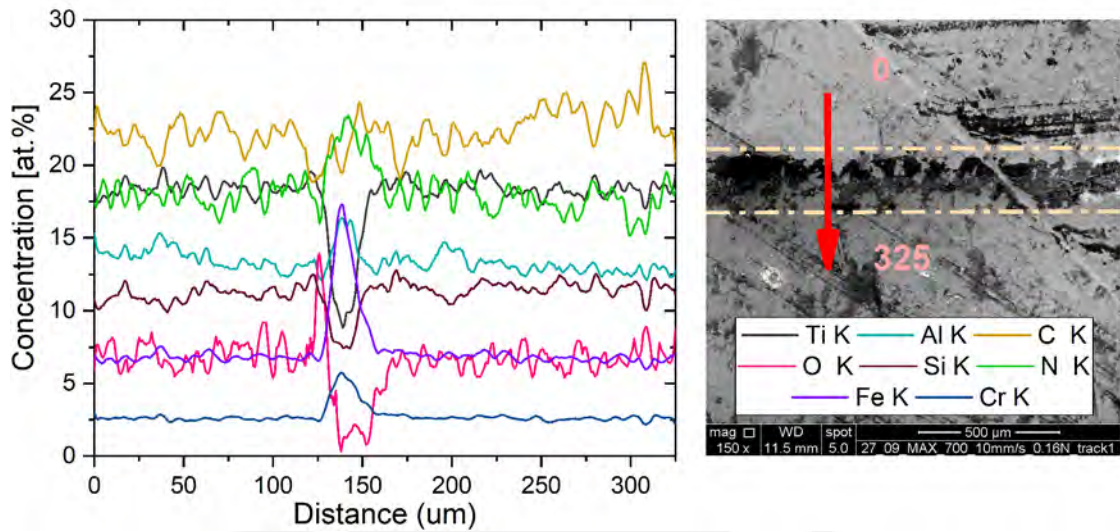


Figure 3.23: Scanning electron microscope-energy dispersive X-Ray detector (SEM-EDX) analysis of Ti_2AlC at 15 kV. SEM micrographs of the wear track at 10 mm s^{-1} and 0.16 N. The orange dashed line shows the position of the wear track.

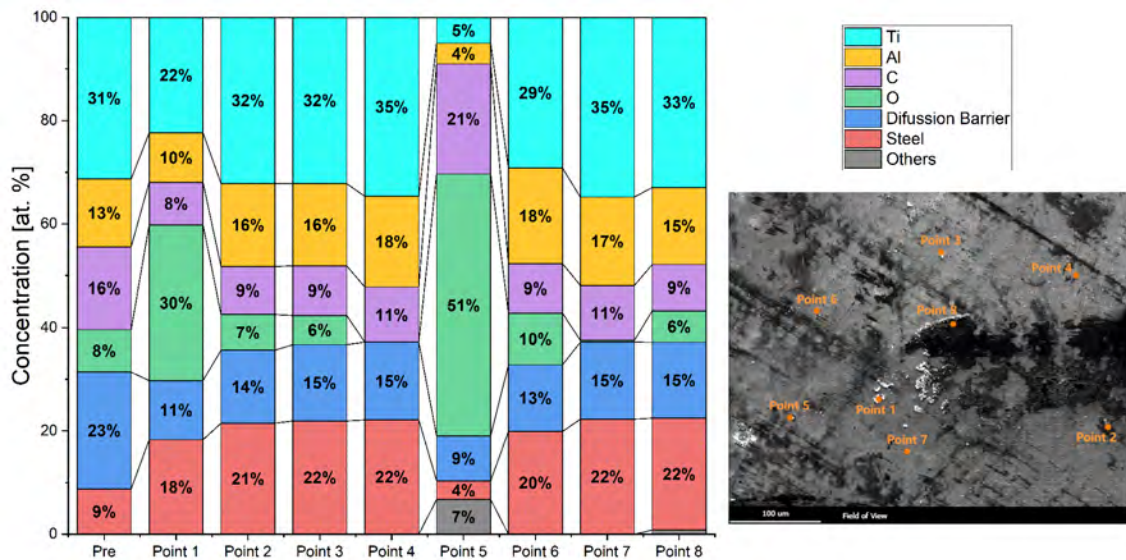


Figure 3.24: EDX points analysis on the scanning electron microscopy (SEM) images of Ti_2AlC wear particles around a wear track at 10 mm s^{-1} and 0.16 N.

To describe the boundaries, eight points were measured in the lateral borders (superior and inferior) and in the wear particles Figure 3.24. The lateral boundaries where particle buildup

was apparent (points 2, 3, 4, 6, and 7) are identical to the inside of the track (point 8). These points have lowered their diffusion barrier and replaced it with AISI 52100 steel. They also had identical Ti, Al, and C concentrations as before the tribological test. Point 1 is located in a large wear particle at the track's edge. It has similar steel levels, but less MAX phase coating and more oxides. On the other hand, point 5 is located further from the track where a group of particles are located. This zone is full of oxides and all the elements in Ti_2AlC are reduce to a fraction of before.

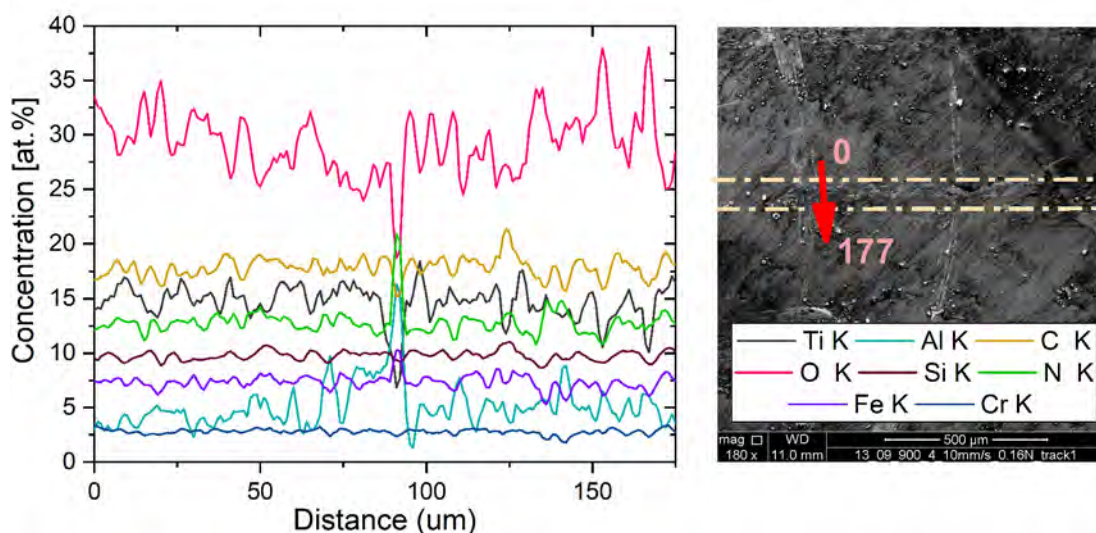


Figure 3.25: Scanning electron microscope-energy dispersive X-Ray detector (SEM-EDX) analysis of Ti_3AlC_2 at 15 kV. SEM micrographs of the wear track at 10 mm s^{-1} and 0.16 N. The orange dashed line shows the position of the wear track.

The Ti_3AlC_2 track is more visible than at 2 mm s^{-1} , but in have a width of no more than $40 \mu\text{m}$. The percentage of Ti in the sample is the lowest yet, hence this track have a almost no visible wear particles. Also, the only complementary variations are with the reduction of C and increasing of N from the diffusion barrier. At the border in Figure 3.26, the points 1 and 4 inside the track are similar to the values before the tribological test. On the other hand, points 2 and 3 seem to be residues from the AISI 52100 ball due to its high levels of steel and oxides.

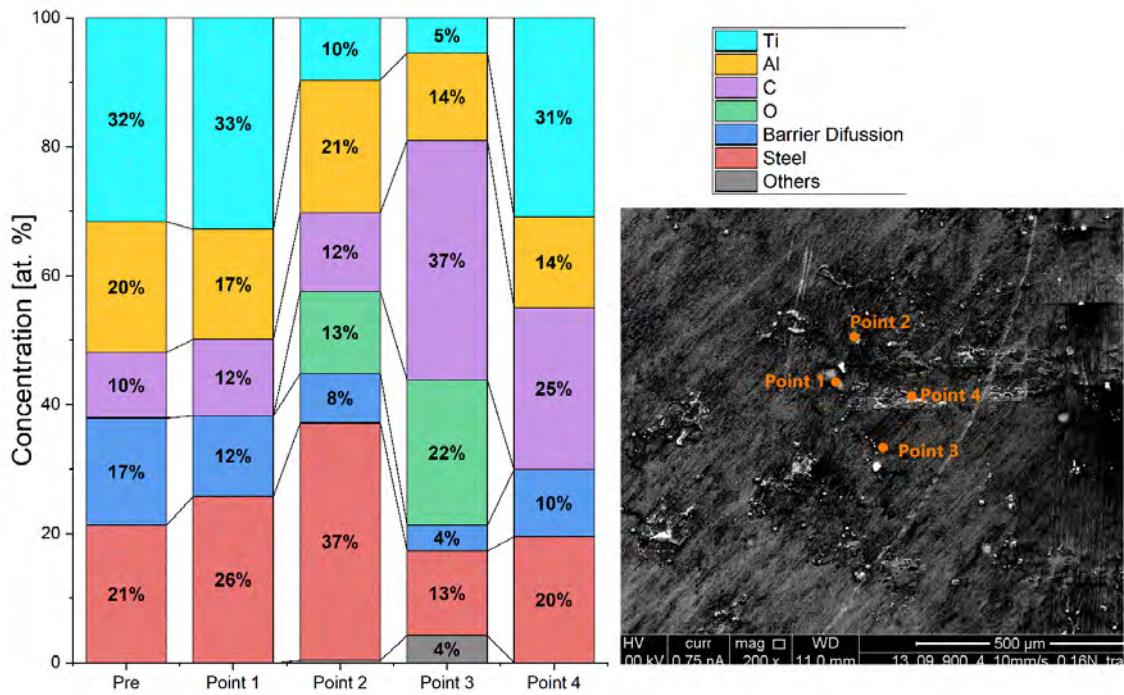


Figure 3.26: EDX points analysis on the scanning electron microscopy (SEM) images of Ti_3AlC_2 wear particles around a wear track at 10 mm s^{-1} and 0.16 N .

At 10 mm s^{-1} and 0.8 N

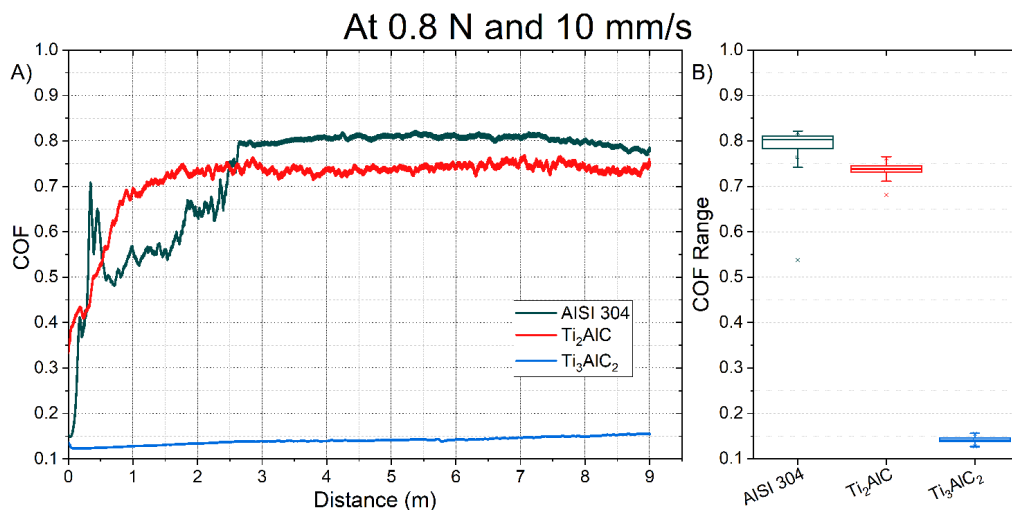


Figure 3.27: COF analysis for Steel, Ti_2AlC and Ti_3AlC_2 at 10 mm s^{-1} and 0.8 N .

At high speed and medium normal force in Figure 3.27, the AISI 304 have a short duration running-in until it reach 0.8 as its COF. The Ti_2AlC sample reach 0.75 after a rupture of the coating at the beginning like in previous results. Meanwhile, the Ti_2AlC stabilize its high COF (at 0.75) probably due to the wear of both MAX phase coating and Si_xN_y coating. The Ti_3AlC_2 sample had a lower COF of with a running in behavior for 3 m reaching 0.14 as before.

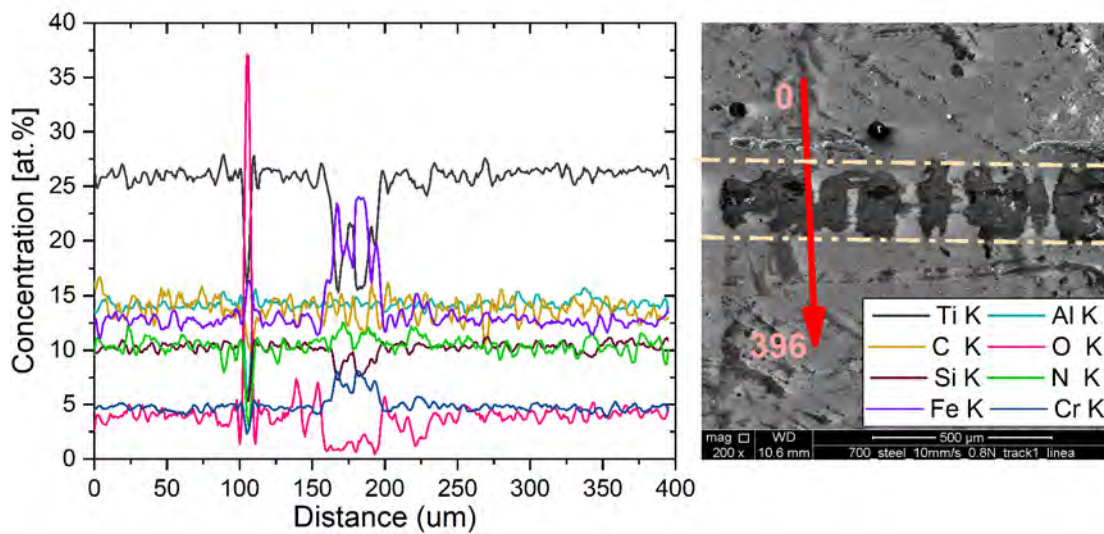


Figure 3.28: Scanning electron microscope-energy dispersive X-Ray detector (SEM-EDX) analysis of Ti_2AlC at 15 kV. SEM micrographs of the wear track at 10 mm s^{-1} and 0.8 N. The orange dashed line shows the position of the wear track.

In Figure 3.28, the SEM image shows an irregular track. The track width of the track was around $50\ \mu\text{m}$ to $75\ \mu\text{m}$. The first peak in oxygen levels is consequence of a accumulation of particles at $100\ \mu\text{m}$. Inside the track there was only a decreasing of less than 10 % of Ti, with its respectively complementary increase on Fe. The levels of chromium increase (2 %) probably came from AISI 52100. To analyze the border, seven points were positioned in 3 zones in Figure 3.29: inside the track (point 2 and 3), lateral of the track (point 1 and 4) and outside the border points 5, 6 and 7). In the first zone, point 2 seems to have not lose its Ti_2AlC coating, but instead had particles from the AISI 52100 (increase in steel) and oxides generated by the heat

from the test (accumulated in point 3). Outside the track, in the second zone, point 1 preserves its coating with small accumulations of oxide. On the other hand, in point 4 there is not only a visible accumulation (see SEM image in Figure 3.29), there is also a high increase of 40 % in levels of oxygen. At last, the third zone had a same behavior of preserve coating in point 5, but particles of oxide in point 6 and 7.

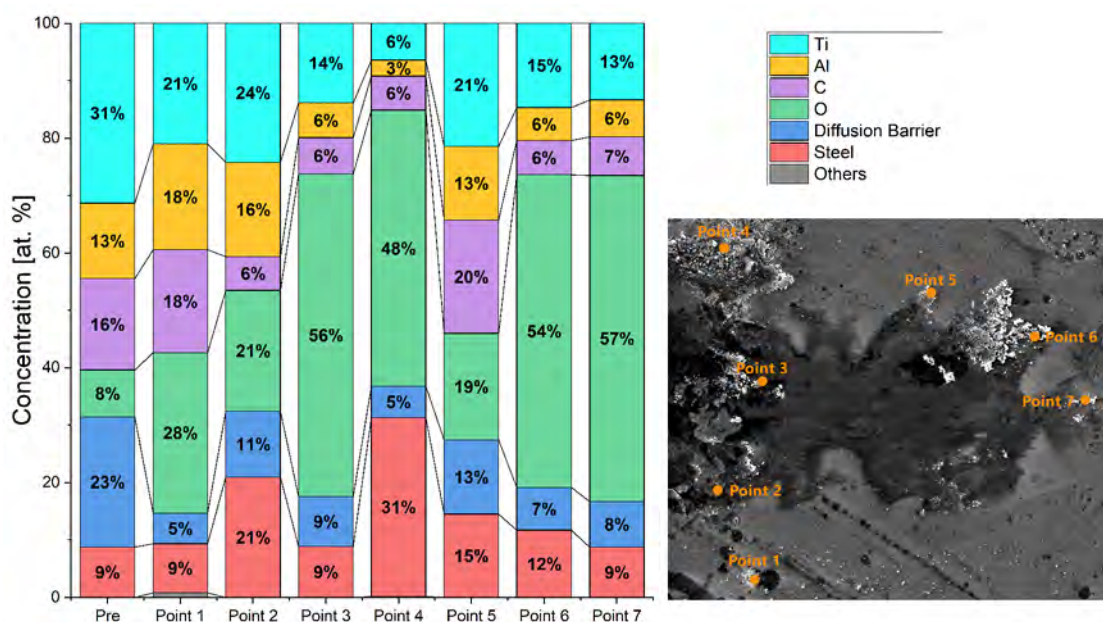


Figure 3.29: EDX points analysis on the scanning electron microscopy (SEM) images of Ti_2AlC wear particles around a wear track at 10 mm s^{-1} and 0.8 N .

With a COF of 0.14, Ti_3AlC_2 had a big track almost no perturbation with a constant COF of 0.15. The SEM image in Figure 3.30 show a track with a width around 50 mm. The only perturbations are at the borders, where the levels of carbon rise and the level of N slightly decrease. The rest of elements does not have significant variations. The points at the border in Figure 3.31 are divided in zones. The first zone has the points closer to the border of the track (point 1, 2 and 4). These points have a similar composition as the samples tested before, this could evidence that the Ti_3AlC_2 coating had only been partially delaminated by the friction. The further the point is (points 5, 6 and 7), it is probable that it has come from the delamination from

inside the track. In contrast, the steel is highly present in the point 3 where seems to be visible the AISI 304 due to the extreme pressure in the border where the ball changes its direction.

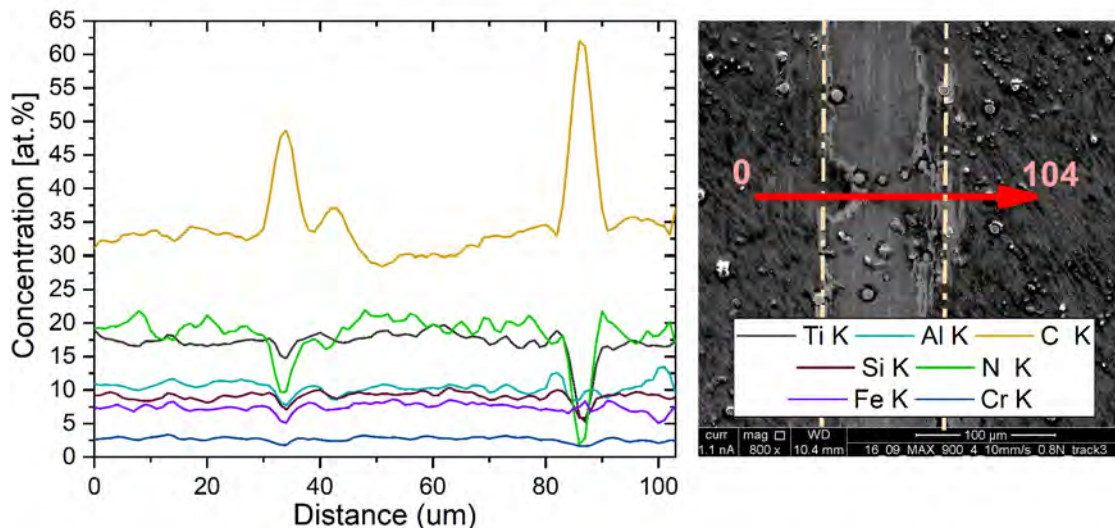


Figure 3.30: Scanning electron microscope-energy dispersive X-Ray detector (SEM-EDX) analysis of Ti_3AlC_2 at 15 kV. SEM micrographs of the wear track at 10 mm s^{-1} and 0.8 N. The orange dashed line shows the position of the wear track.

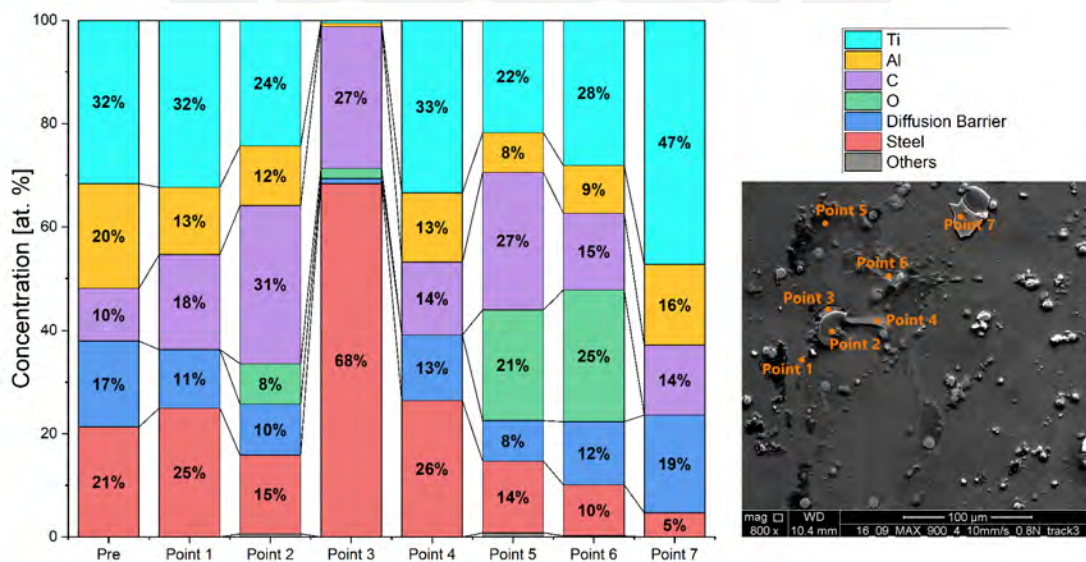


Figure 3.31: EDX points analysis on the scanning electron microscopy (SEM) images of Ti_3AlC_2 wear particles around a wear track at 10 mm s^{-1} and 0.8 N.

At 10 mm s^{-1} and 1.6 N

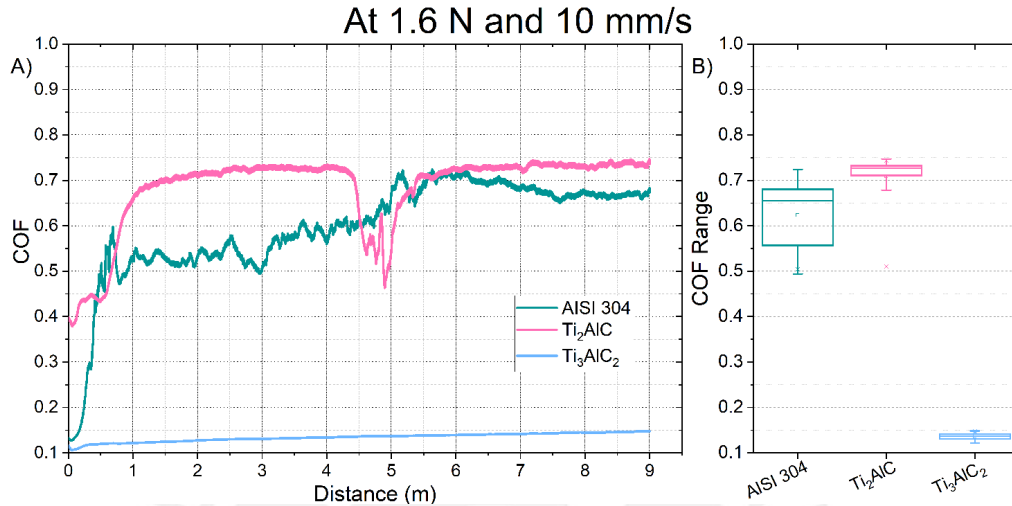


Figure 3.32: COF analysis for Steel, Ti_2AlC and Ti_3AlC_2 at 10 mm s^{-1} and 1.6 N .

At high speed and high normal force in Figure 3.32, the AISI 304 still have a running-in effect until it surpasses 0.9 as its COF. The Ti_2AlC sample reaches 0.75 (as in the previous tests) after a rupture of the coating at the beginning. However, the Ti_2AlC had reach a plateau at 0.75, far from the steel (at 0.92). The Ti_3AlC_2 sample had again a lower COF at 0.14.

The Raman spectrum in Figure 3.33 shows a accumulation of Ti_2AlC particles inside the track, since the SEM image exhibit wear formation. Inside the track there is low levels Ti_2AlC , and no graphite. The graphite, and most of particles, seem to be accumulated at the border where the ball changes its direction (blue curve). In this location, the levels of Ti_2AlC are even 10 times the previously found. And also most of the graphite seems to be located here. At the superior location is an evident presence of Ti_2AlC removed from the inside, with some shift in the location of the peaks for Ti_2AlC .

To better analyze the inside of the track, a cross section from Figure 3.34 was taken. The SEM image exhibit a visible track marks with high accumulation of particles from inside the track. The track had a width of over $100 \mu\text{m}$. Outside the track seems to be a particle accu-

mulation of carbon oxide, since the rest of elements are absent. Inside the track, there is high presence of iron and oxygen in the darker zones of the image. The levels of Ti, Al and C from the Ti_2AlC are almost no existent inside the track, like in the Raman spectrum Figure 3.33.

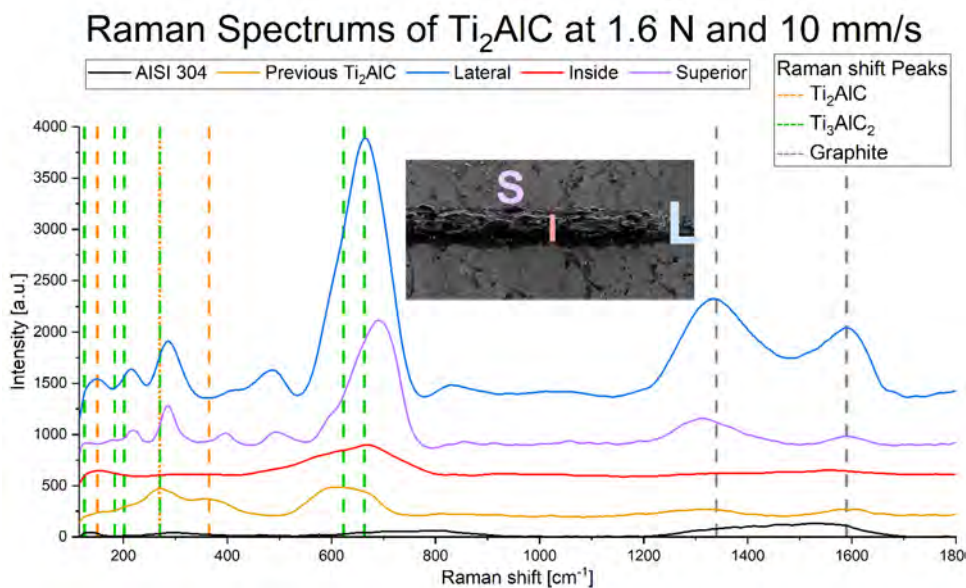


Figure 3.33: Raman spectrums of Ti_2AlC at $700^{\circ}C$ MAX at 10 mm s^{-1} and $1.6N$, where the wear was maximum

At the border were analyzed seven points by EDS, where it seems to be more accumulation of the coating destroyed (Figure 3.33). Those points were located in 3 zones: Inside the track (point 3), at the borders (point 2, 4 and 5) and the rest at different visible wear particles around the track. At point 3, the levels of Ti_2AlC had declined to the half of the levels before the tribo-testing. It seems that the Ti_2AlC was partially removed and the steel presence is partially from the ball since its diffusion barrier is barely evident (a third of before). At the border, points 2 and 4 had a similar proportion of Ti_2AlC as in point 3, with similar formation of oxides in point 2. On contrast, point does not show any Ti_2AlC and it mostly has oxides. Outside the track, point 6 and 7 does not show any Ti_2AlC , but it seems that most has been removed as sheets since point 1 is almost fully Ti_2AlC with Si_xN_y .

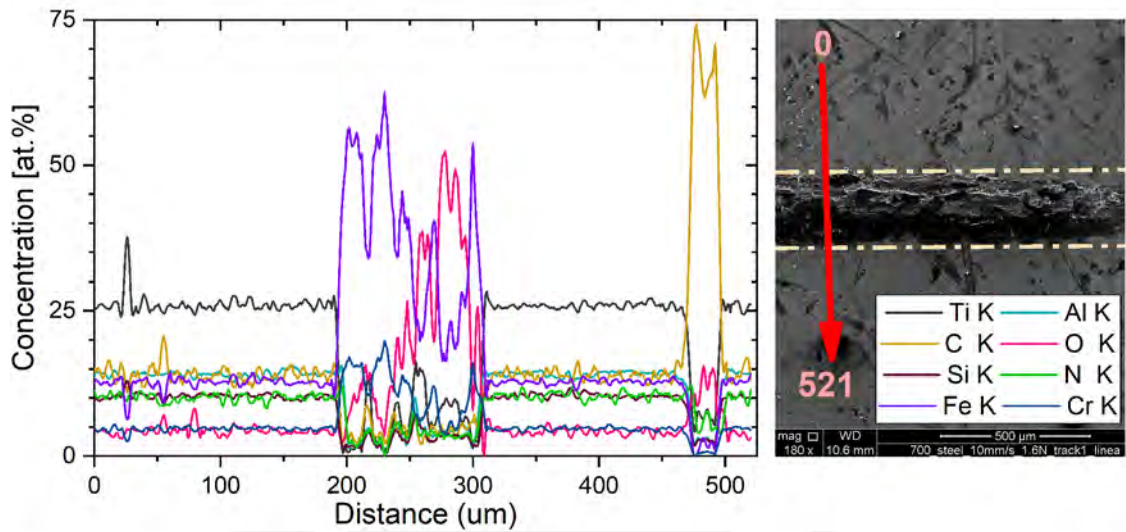


Figure 3.34: Scanning electron microscope-energy dispersive X-Ray detector (SEM-EDX) analysis of Ti_2AlC at 15 kV. SEM micrographs of the wear track at 10 mm s^{-1} and 1.6 N. The orange dashed line shows the position of the wear track.

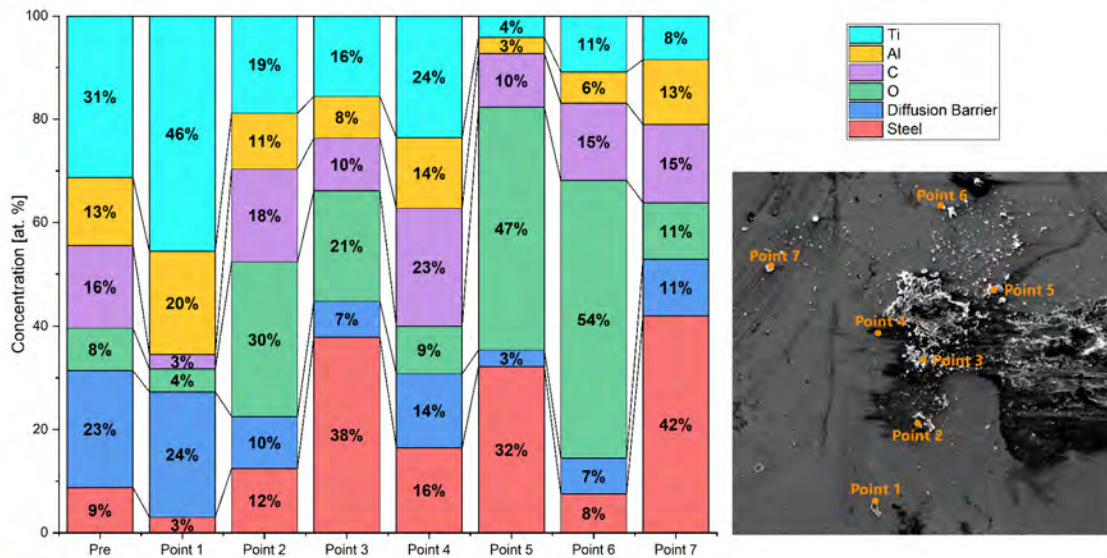


Figure 3.35: EDX points analysis on the scanning electron microscopy (SEM) images of Ti_2AlC wear particles around a wear track at 10 mm s^{-1} and 1.6 N.

The Raman spectrum in Figure 3.36 shows a accumulation of Ti_3AlC_2 particles inside the track, since the SEM image exhibit less wear formation and coating wear than in Ti_2AlC . Inside

the track there is low levels of Ti_3AlC_2 , but the highest levels of graphite. The graphite, and most of particles, seem to be accumulated inside and at the border where the ball changes its direction (blue curve) in less proportion. In this location, the levels of Ti_2AlC are the same as inside and both are higher than the results before the tribometer test. Also at the superior location is an evident presence of small proportion of Ti_2AlC removed from the inside, with no evidence of graphite. There were no peaks with significant shift.

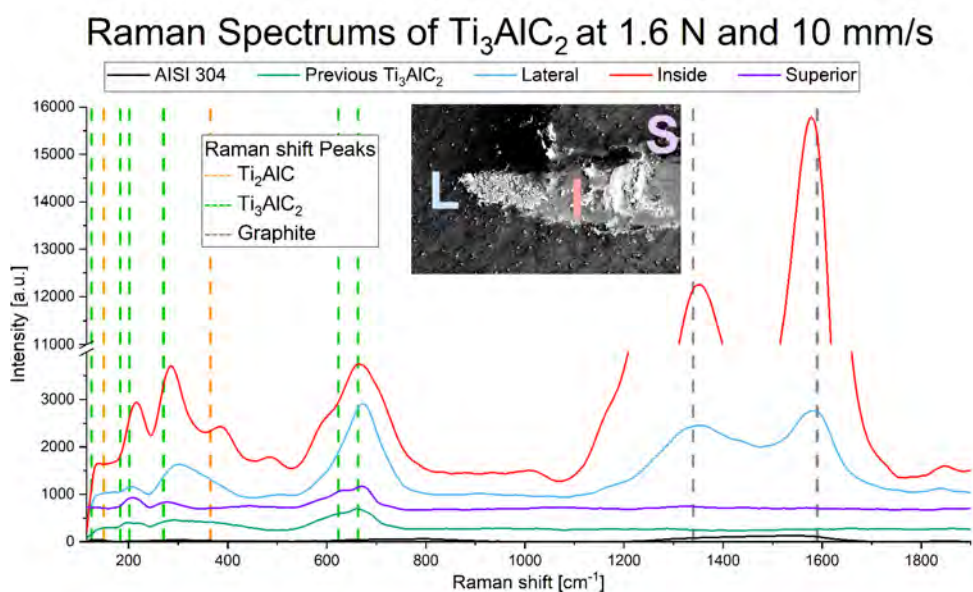


Figure 3.36: Raman spectrums of Ti_3AlC_2 at $950^\circ C$ MAX at 10 mm s^{-1} and $1.6N$, where the wear was maximum

To better analyze the inside of the track, a cross section from Figure 3.37 was taken. The SEM image exhibit a visible track, but no accumulation of particles from inside the track (there is some particles outside the track). The track had a width of less than $80\ \mu m$. Inside the track, there is no noticeable variation on the levels of Ti_3AlC_2 or iron, except a peak of iron at $80\ \mu m$ due to particles from the ball of AISI 52100. The high presence of oxygen in the darker zones of the image is located at the borders of the track. The levels of Ti, Al and C from the Ti_2AlC are not affected, like in the Raman spectrum Figure 3.36. At $20\ \mu m$ seems to be located an

accumulation of graphite remove from the inside of the track.

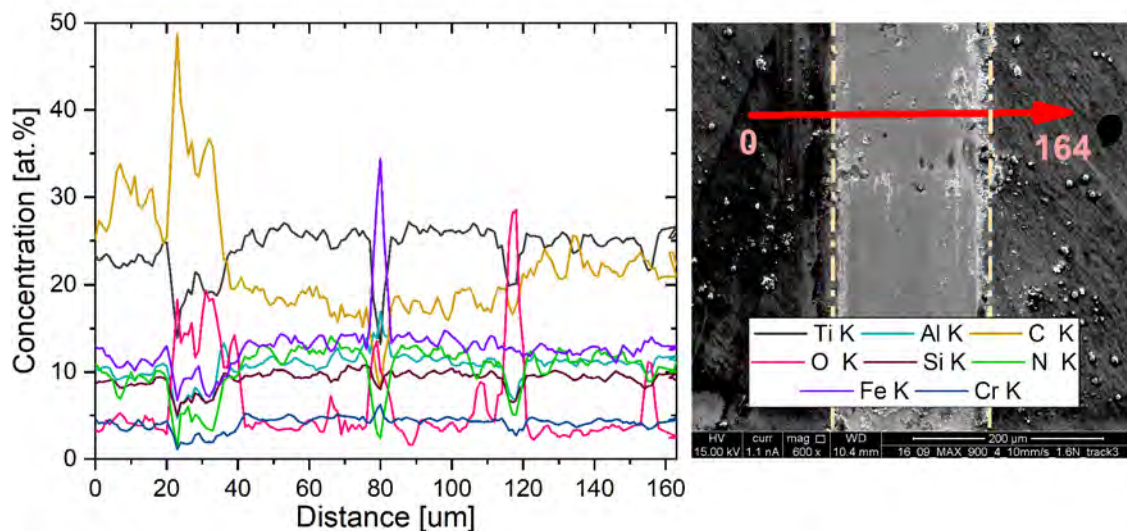


Figure 3.37: Scanning electron microscope-energy dispersive X-Ray detector (SEM-EDX) analysis of Ti_3AlC_2 at 15 kV. SEM micrographs of the wear track at 10 mms^{-1} and 1.6 N. The orange dashed line shows the position of the wear track.

At the border seven points were analyzed by EDS (Figure 3.38), where it seems to be more accumulation of the coating destroyed (Figure 3.36). The point 4 at the inside seems to be almost exactly as before the friction test. However, at point 1 there seems to be accumulation of wear particles even inside the track (as in point 7). This point had the highest level of oxygen, replacing the levels of Ti_3AlC_2 . At the farthest point (point 2), there is the same accumulation of oxides as in point 1. Similarly, but at a lower proportion of Ti_3AlC_2 , points 5 and 6 have only reduced its levels of steel and replaced the absent of Ti_3AlC_2 with oxides. Point 3 on the other hand, had the highest accumulation of what seems to be graphite.

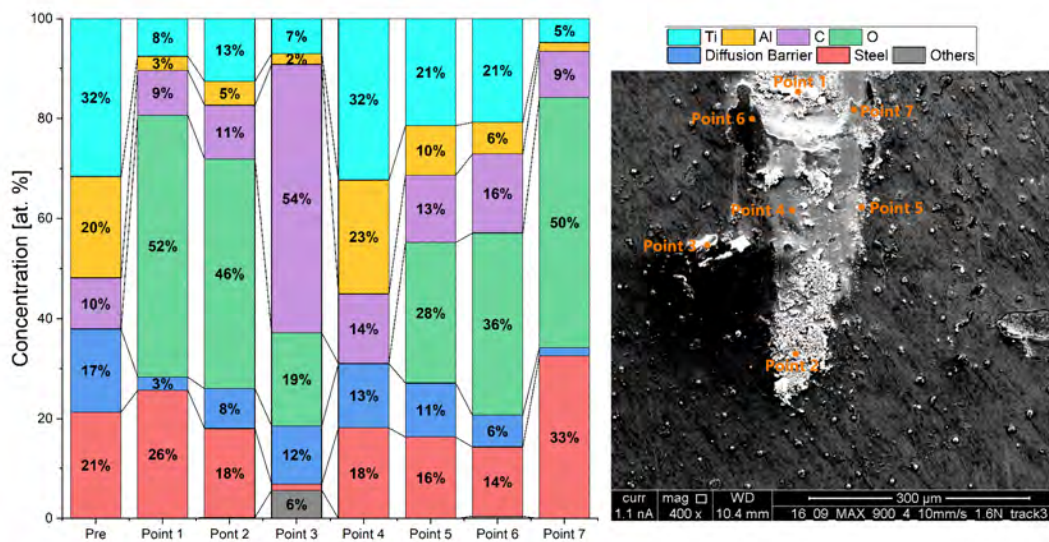


Figure 3.38: EDX points analysis on the scanning electron microscopy (SEM) images of Ti_3AlC_2 wear particles around a wear track at 10 mm s^{-1} and 1.6 N.

Conclusions and Recommendations

The current study shows a characterization of the MAX phase coating on steel, which has not been previously described in the literature. While prior work with silicon as a substrate revealed that Ti_2AlC had a lower COF around 0.2-0.4 (Quispe et al. 2022), the current thesis found that Ti_3AlC_2 had a COF around 0.14 which was lower COF than previously reported in literature (0.7-0.9) superior on steel. In general, the successful formation of Ti_2AlC and Ti_3AlC_2 coatings was verified by XRD and EDS. Throughout the various test periods, the values of the friction coefficient Ti_3AlC_2 remained consistent despite the changes on speed and normal force applied. When the experiments were carried out at low speeds (2 mm s^{-1}), the COF of Ti_2AlC increased in response to an increase in force. This is the opposite of what is mentioned for iron. On the contrary, the behavior of Ti_2AlC remained consistent, independent of force, as speed increased.

Although initially it was observed that the coefficient of friction of steel was occasionally lower, it was discovered that when the velocity was increased,

Ti_2AlC had a better long-term behavior (after 3 m). Ti_3AlC_2 had the lowest COF, but also had the least visible tracks with less variations in the composition linescan. The particles that were accumulated at the borders of the tracks were mostly oxides. On the other hand, the observed elements representing steel most probably came from the ball counterparts instead of the substrate. This supports the hypothesis of MAX phases Ti_2AlC and Ti_3AlC_2 coatings worked good as protective coating providing additionally a low COF.

In the future, it would be beneficial to assess not just with a ball-on-flat tribometer, which

simplifies wear, but also with a pin-on-disk tribometer, which can replicate friction in a spherical joint better (Scholes and Unsworth 2009; Shen, Fang, and Kang 2018). These additional tests should be included in a broader review of a tribocorrosive test. This tribocorrosive test allows the measurement of not only the effect of mechanical friction, but also the influence of the electrolytic solutions to which the hip implant is subjected (Davim 2013). However, the biocompatibility of the MAX phase coating and its wear particles must be confirmed. Cell proliferation with human cell lines can be used to measure biocompatibility. Osseointegration testing would also be possible. This assays should be performed before and after the friction test.

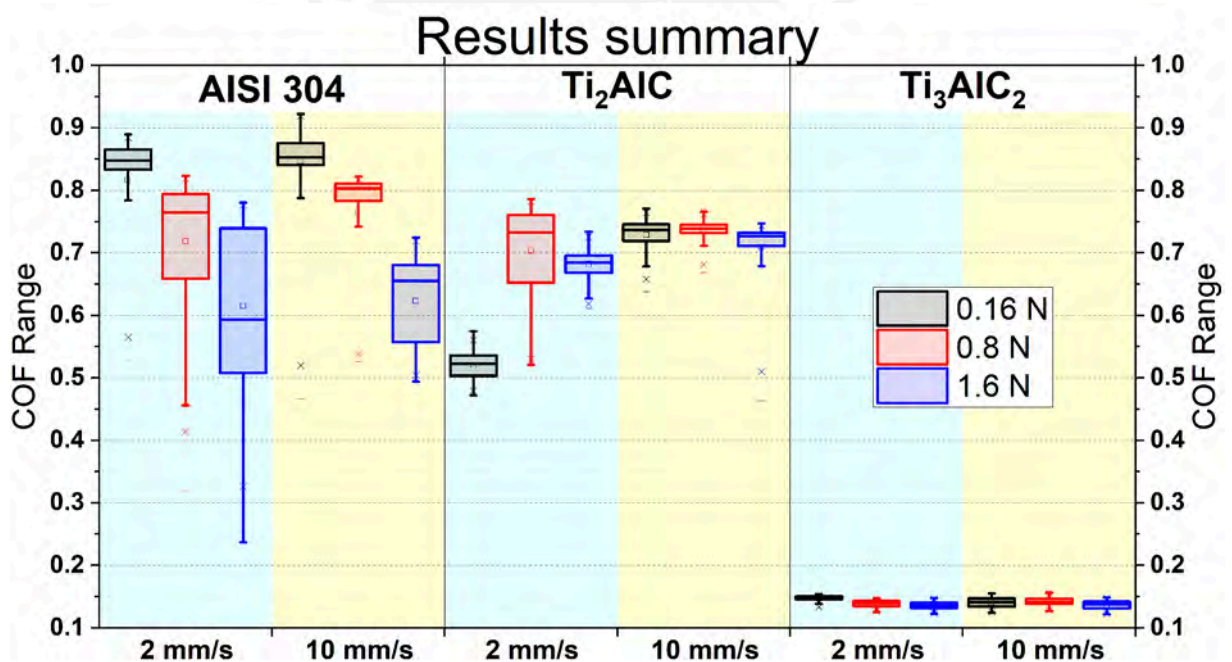


Figure 3.39: Comparison of COFs analysis for Steel, Ti_2AlC and Ti_3AlC_2 at each speed and force combination.

Bibliography

- [AAOS (2021)] AAOSAAOS (2021). *Annual Report AJRR 2021*. Reporte Anual 8. Rosemont: American Academy of Orthopaedic Surgeons, p. 124.
- [Abdo, Hany S. et al. (Dec. 2021)] Abdo, Hany S. et al.— (Dec. 2021). «Tribo-Behavior and Corrosion Properties of Welded 304L and 316L Stainless Steel». In: *Coatings* 11.12, p. 1567. ISSN: 2079-6412. DOI: 10.3390/coatings11121567.
- [Aherwar, Amit et al. (2015)] Aherwar, Amit et al.— (2015). «Current and Future Biocompatibility Aspects of Biomaterials for Hip Prosthesis». In: *AIMS Bioengineering* 3.1, pp. 23–43. ISSN: 2375-1495. DOI: 10.3934/bioeng.2016.1.23.
- [AlHazaa, Abdulaziz and Nils Haneklaus (May 2020)] AlHazaa, Abdulaziz and Nils Haneklaus— (May 2020). «Diffusion Bonding and Transient Liquid Phase (TLP) Bonding of Type 304 and 316 Austenitic Stainless Steel—A Review of Similar and Dissimilar Material Joints». In: *Metals* 10.5, p. 613. ISSN: 2075-4701. DOI: 10.3390/met10050613.
- [Ansari, Shakeel and Qayyum Husain (July 2011)] Ansari, Shakeel and Qayyum Husain— (July 2011). «Immobilization of Kluyveromyces Lactis β Galactosidase on Concanavalin A Layered Aluminium Oxide Nanoparticles—Its Future Aspects in Biosensor Applications». In: *Journal of Molecular Catalysis B-enzymatic - J MOL CATAL B-ENZYM* 70, pp. 119–126. DOI: 10.1016/j.molcatb.2011.02.016.

- [Arash, Valiollah et al. (July 2015)] Arash, Valiollah et al. Arash, Valiollah et al. (July 2015). «The Effects of Silver Coating on Friction Coefficient and Shear Bond Strength of Steel Orthodontic Brackets: Friction and Shear Bond of Silver Coated Orthodontic Brackets». In: *Scanning* 37.4, pp. 294–299. ISSN: 01610457. DOI: 10.1002/sca.21212.
- [Awad, A.M. et al. (Mar. 2012)] Awad, A.M. et al.— (Mar. 2012). «Electropolishing of AISI-304 Stainless Steel for Protection against SRB Biofilm». In: *Surface and Coatings Technology* 206.14, pp. 3165–3172. ISSN: 02578972. DOI: 10.1016/j.surfcoat.2011.11.046.
- [Bayliss, Lee E et al. (Apr. 2017)] Bayliss, Lee E et al.— (Apr. 2017). «The Effect of Patient Age at Intervention on Risk of Implant Revision after Total Replacement of the Hip or Knee: A Population-Based Cohort Study». In: *The Lancet* 389.10077, pp. 1424–1430. ISSN: 01406736. DOI: 10.1016/S0140-6736(17)30059-4.
- [Bergmann, G. et al. (Apr. 2001)] Bergmann, G. et al.— (Apr. 2001). «Frictional Heating of Total Hip Implants, Part 1: Measurements in Patients». In: *Journal of Biomechanics* 34.4, pp. 421–428. ISSN: 00219290. DOI: 10.1016/S0021-9290(00)00188-3.
- [Borba, Antônio Pereira et al. (2020)] Borba, Antônio Pereira et al.— (2020). «Microstructural Analysis of Corrosion of Welded Joints in Stainless Steel Used in Manufacture of Bioreactors». In: 0 Bytes. DOI: 10.6084/M9.FIGSHARE.12317492.
- [Borjali, A., K. Monson, and B. Raeymaekers (Nov. 2018)] Borjali, A., K. Monson, and B. Raeymaekers— (Nov. 2018). «Friction between a Polyethylene Pin and a Microtextured CoCrMo Disc, and Its Correlation to Polyethylene Wear, as a Function of Sliding Velocity and Contact Pressure, in the Context of Metal-on-Polyethylene Prosthetic Hip Implants». In: *Tribology International* 127, pp. 568–574. ISSN: 0301-679X. DOI: 10.1016/j.triboint.2018.07.005.

- [Borjali, A., K. Monson, and B. Raeymaekers (May 2019)] Borjali, A., K. Monson, and B. Raeymaekers (May 2019). «Predicting the Polyethylene Wear Rate in Pin-on-Disc Experiments in the Context of Prosthetic Hip Implants: Deriving a Data-Driven Model Using Machine Learning Methods». In: *Tribology International* 133, pp. 101–110. ISSN: 0301679X. DOI: 10.1016/j.triboint.2019.01.014.
- [Boutrand, Jean-Pierre, ed. (2019)] Boutrand, Jean-Pierre, ed.— ed. (2019). *Biocompatibility and Performance of Medical Devices*. Waltham: Elsevier. ISBN: 978-0-08-102643-4.
- [Bozic, Kevin J et al. (July 2009)] Bozic, Kevin J et al.— (July 2009). «The Epidemiology of Bearing Surface Usage in Total Hip Arthroplasty in the United States:» in: *The Journal of Bone and Joint Surgery-American Volume* 91.7, pp. 1614–1620. ISSN: 0021-9355. DOI: 10.2106/JBJS.H.01220.
- [Buck, Edgar (Nov. 2017)] Buck, Edgar— (Nov. 2017). *Electron Microscopy Characterization of Suspended Solids from Hanford Tank 241-AP-105 Direct Feed Waste*. Tech. rep. PNNL–27065, 1598866, PNNL–27065, 1598866. DOI: 10.2172/1598866.
- [Cai, Leping et al. (2017)] Cai, Leping et al.— (2017). «Fabrication, Mechanical Properties, and Tribological Behaviors of Ti₂AlC and Ti₂AlSn_{0.2}C Solid Solutions». In: *Journal of Advanced Ceramics* 6.2, pp. 90–99. ISSN: 22278508. DOI: 10.1007/s40145-017-0221-9.
- [Cao, Jun et al. (2018)] Cao, Jun et al.— (2018). «Tribological and Mechanical Properties of Ti₂AlC Coating at Room Temperature and 800 °C». In: *Ceramics International* 44.1, pp. 1046–1051. ISSN: 02728842. DOI: 10.1016/j.ceramint.2017.10.045.
- [Çelebi Efe, Gözde et al. (July 2021)] Çelebi Efe, Gözde et al.— (July 2021). «Characterization of UHMWPE- HAp Coating Produced by Dip Coating Method on Ti6Al4V Alloy». In: *Surface and Coatings Technology* 418, p. 127091. ISSN: 02578972. DOI: 10.1016/j.surfcoat.2021.127091.

- [Chandra, A. et al. (Nov. 2011)] Chandra, A. et al. Chandra, A. et al. (Nov. 2011). «Life Expectancy of Modular Ti6Al4V Hip Implants: Influence of Stress and Environment». In: *Journal of the Mechanical Behavior of Biomedical Materials* 4.8, pp. 1990–2001. ISSN: 17516161. DOI: 10.1016/j.jmbbm.2011.06.018.
- [Chowdhury, Mohammad et al. (Dec. 2013)] Chowdhury, Mohammad et al.— (Dec. 2013). «Experimental Investigation of Friction Coefficient and Wear Rate of Stainless Steel 304 Sliding against Smooth and Rough Mild Steel Counterfaces». In: *Tribology in Industry* 35, pp. 286–296.
- [Cohen, D. (May 2012)] Cohen, D.— (May 2012). «How Safe Are Metal-on-Metal Hip Implants?» In: *BMJ* 344.feb28 1, e1410–e1410. ISSN: 1756-1833. DOI: 10.1136/bmj.e1410.
- [Cuao-Moreu, C.A. et al. (Oct. 2020)] Cuao-Moreu, C.A. et al.— (Oct. 2020). «Characterization of a Duplex Coating (Boriding + Sputter-Deposited AlCrON) Synthesized on an ASTM F-75 Cobalt Alloy». In: *Thin Solid Films* 712, p. 138318. ISSN: 00406090. DOI: 10.1016/j.tsf.2020.138318.
- [D'Andrea, Danilo et al. (2021)] D'Andrea, Danilo et al.— (2021). «Tribological Characterization of a Hip Prosthesis in Si3N4-TiN Ceramic Composite Made with Electrical Discharge Machining (EDM)». In: *Procedia Structural Integrity* 33, pp. 469–481. ISSN: 24523216. DOI: 10.1016/j.prostr.2021.10.054.
- [Davim, J. Paulo, ed. (2013)] Davim, J. Paulo, ed.— ed. (2013). *Biomaterials and Medical Tribology: Research and Development*. Woodhead Publishing Series in Biomaterials number 65. Oxford ; Philadelphia: Woodhead Publishing. ISBN: 978-0-85709-017-1.
- [Dib, J. et al. (May 2020)] Dib, J. et al.— (May 2020). «Influence of Load, Surface Finish and Lubrication on Friction Coefficient of AISI 304 Stainless Steel». In: *J. of Materi Eng and Perform* 29.5, pp. 2739–2747. ISSN: 1059-9495, 1544-1024. DOI: 10.1007/s11665-020-04768-z.

- [Doche, Marie-Laure et al. (2022)] Doche, Marie-Laure et al. Doche, Marie-Laure et al. (2022). «Electropolishing of 316L Stainless Steel Parts Elaborated by Selective Laser Melting: From Laboratory to Pilot Scale». In: *Procedia CIRP* 108, pp. 722–727. ISSN: 22128271. DOI: 10.1016/j.procir.2022.04.080.
- [Dogan, Halit, Fehim Findik, and Ahmet Oztarhan (Apr. 2003)] Dogan, Halit, Fehim Findik, and Ahmet Oztarhan— (Apr. 2003). «Comparative Study of Wear Mechanism of Surface Treated AISI 316L Stainless Steel». In: *Industrial Lubrication and Tribology* 55.2, pp. 76–83. ISSN: 0036-8792. DOI: 10.1108/00368790310470903.
- [Dowson, Duncan (2012)] Dowson, Duncan— (2012). «Bio-Tribology». In: *Faraday Discussions* 156, pp. 9–30. ISSN: 13596640. DOI: 10.1039/c2fd20103h.
- [Dunlap, Michael and J.E. Adaskaveg (1997)] Dunlap, Michael and J.E. Adaskaveg— (1997). *Introduction to the Scanning Electron Microscope*.
- [Eklund, Per et al. (2010)] Eklund, Per et al.— (2010). «The Mn + 1AX_n Phases: Materials Science and Thin-Film Processing». In: *Thin Solid Films* 518.8, pp. 1851–1878. ISSN: 00406090. DOI: 10.1016/j.tsf.2009.07.184.
- [Eliaz, Noam (Jan. 2019)] Eliaz, Noam— (Jan. 2019). «Corrosion of Metallic Biomaterials: A Review». In: *Materials* 12.3, p. 407. ISSN: 1996-1944. DOI: 10.3390/ma12030407.
- [Fellah, M. et al. (2014)] Fellah, M. et al.— (2014). «Tribological Behavior of Biomaterial for Total Hip Prosthesis». In: *Matériaux & Techniques* 102.6-7, p. 601. ISSN: 0032-6895, 1778-3771. DOI: 10.1051/mattech/2014027.
- [Ferguson, Rory J et al. (Nov. 2018)] Ferguson, Rory J et al.— (Nov. 2018). «Hip Replacement». In: *The Lancet* 392.10158, pp. 1662–1671. ISSN: 01406736. DOI: 10.1016/S0140-6736(18)31777-X.

- [Gnanavel, S. et al. (Mar. 2018)] Gnanavel, S. et al. Gnanavel, S. et al. (Mar. 2018). «In Vitro Corrosion Behaviour of Ti–6Al–4V and 316L Stainless Steel Alloys for Biomedical Implant Applications». In: *J Bio Tribo Corros* 4.1, p. 1. ISSN: 2198-4220, 2198-4239. DOI: 10.1007/s40735-017-0118-8.
- [Goldstein, Joseph I. et al. (2018)] Goldstein, Joseph I. et al.— (2018). *Scanning Electron Microscopy and X-Ray Microanalysis*. New York, NY: Springer New York. ISBN: 978-1-4939-6674-5 978-1-4939-6676-9. DOI: 10.1007/978-1-4939-6676-9.
- [Goodman, Robert (2021)] Goodman, Robert— (2021). «Calidad de Vida de Pacientes Operados de Artroplastia de Cadera». PhD thesis. Lima: Universidad Científica del Sur.
- [Gupta, S. et al. (2008)] Gupta, S. et al.— (2008). «Tribological Behavior of Select MAX Phases against Al₂O₃ at Elevated Temperatures». In: *Wear* 265.3-4, pp. 560–565. ISSN: 00431648. DOI: 10.1016/j.wear.2007.11.018.
- [Haftani, Mohammad et al. (Dec. 2016)] Haftani, Mohammad et al.— (Dec. 2016). «Studying the Oxidation of Ti₂AlC MAX Phase in Atmosphere: A Review». In: *International Journal of Refractory Metals and Hard Materials* 61, pp. 51–60. ISSN: 02634368. DOI: 10.1016/j.ijrmhm.2016.07.006.
- [Haider, Hani et al. (Sept. 2017)] Haider, Hani et al.— (Sept. 2017). «Why Coating Technologies for Hip Replacement Systems, and the Importance of Testing Them In Vitro». In: *Operative Techniques in Orthopaedics* 27.3, pp. 152–160. ISSN: 10486666. DOI: 10.1053/j.oto.2017.05.003.
- [Ul-Hamid, Anwar (2018)] Ul-Hamid, Anwar— (2018). *A Beginners' Guide to Scanning Electron Microscopy*. Cham: Springer International Publishing. ISBN: 978-3-319-98481-0 978-3-319-98482-7. DOI: 10.1007/978-3-319-98482-7.

- [Herbster, Maria et al. (Dec. 2020)] Herbster, Maria et al. (Dec. 2020). «Retrieval Study of Commercially Available Knee Implant Coatings TiN, TiNbN and ZrN on TiAl6V4 and CoCr28Mo6». In: *Journal of the Mechanical Behavior of Biomedical Materials* 112, p. 104034. ISSN: 17516161. DOI: 10.1016/j.jmbbm.2020.104034.
- [Hopfeld, Marcus et al. (2014)] Hopfeld, Marcus et al.— (2014). «Tribological Behavior of Selected Mn+1AX_n Phase Thin Films on Silicon Substrates». In: *Surface and Coatings Technology* 257, pp. 286–294. ISSN: 02578972. DOI: 10.1016/j.surfcoat.2014.08.034.
- [Huang, Zhenying, Hao Xu, et al. (2015)] Huang, Zhenying, Hao Xu, et al.— (2015). «Strengthening and Tribological Surface Self-Adaptability of Ti₃AlC₂ by Incorporation of Sn to Form Ti₃Al(Sn)C₂ Solid Solutions». In: *Ceramics International* 41.3, pp. 3701–3709. ISSN: 02728842. DOI: 10.1016/j.ceramint.2014.11.042.
- [Huang, Zhenying, Hongxiang Zhai, et al. (2014)] Huang, Zhenying, Hongxiang Zhai, et al.— (2014). «Friction Behaviors and Effects on Current-Carrying Wear Characteristics of Bulk Ti₃AlC₂». In: *Tribology Transactions* 57.2, pp. 300–307. ISSN: 1547397X. DOI: 10.1080/10402004.2013.871377.
- [Hughes, Richard E., Aditi Batra, and Brian R. Hallstrom (June 2017)] Hughes, Richard E., Aditi Batra, and Brian R. Hallstrom— (June 2017). «Arthroplasty Registries around the World: Valuable Sources of Hip Implant Revision Risk Data». In: *Curr Rev Musculoskelet Med* 10.2, pp. 240–252. ISSN: 1935-9748. DOI: 10.1007/s12178-017-9408-5.
- [Hutchings, Ian and Philip Shipway (2017a)] Hutchings, Ian and Philip Shipway— (2017a). *Friction and Wear of Engineering Materials*. ISBN: 978-0-08-100910-9. DOI: 10.1016/B978-0-08-100910-9.00003-9.
- [— (2017b)] Hutchings, Ian and Philip Shipway— (2017b). «Introduction». In: *Tribology*, pp. 1–5. DOI: 10.1016/B978-0-08-100910-9.00001-5.

- [Jamari, J. et al. (July 2022)] Jamari, J. et al. Jamari, J. et al. (July 2022). «In Silico Contact Pressure of Metal-on-Metal Total Hip Implant with Different Materials Subjected to Gait Loading». In: *Metals* 12.8, p. 1241. ISSN: 2075-4701. DOI: 10.3390/met12081241.
- [Jiang, Feng et al. (2011)] Jiang, Feng et al.— (2011). «High Temperature Wear of Ti3AlC2 Sliding against Al2O3». In: *Advanced Materials Research* 177, pp. 118–120. ISSN: 10226680. DOI: 10.4028/www.scientific.net/AMR.177.118.
- [Karachalios, Theofilos, George Komnos, and Antonios Koutalos (May 2018)] Karachalios, Theofilos, George Komnos, and Antonios Koutalos— (May 2018). «Total Hip Arthroplasty». In: *EFORT Open Rev* 3.5, pp. 232–239. ISSN: 2058-5241. DOI: 10.1302/2058-5241.3.170068.
- [Karunakaran, Chockalingam, Premkumar Anilkumar, and Paramasivan Gomathisankar (June 2011)] Karunakaran, Chockalingam, Premkumar Anilkumar, and Paramasivan Gomathisankar— (June 2011). «Photoproduction of Iodine with Nanoparticulate Semiconductors and Insulators». In: *Chemistry Central journal* 5, p. 31. DOI: 10.1186/1752-153X-5-31.
- [Kilgour, A. and A. Elfick (Sept. 2008)] Kilgour, A. and A. Elfick— (Sept. 2008). «Design and Test of Novel Tribometer: Investigation into Wear Performance of Materials Used in Total Hip Replacements». In: *Tribology - Materials, Surfaces & Interfaces* 2.3, pp. 161–168. ISSN: 1751-5831, 1751-584X. DOI: 10.1179/175158309X408324.
- [Kretzer, J. Philippe (2013)] Kretzer, J. Philippe— (2013). «Biotribology of Total Hip Replacement: The Metal-on-Metal Articulation». In: *Biotribology*, pp. 1–49. DOI: 10.1002/9781118557969.ch1.
- [Lee, Myeongkyu (2016)] Lee, Myeongkyu— (2016). *X-Ray Diffraction for Materials Research: From Fundamentals to Applications*. Oakville, ON, Canada ; Waretown, NJ, USA: Apple Academic Press. ISBN: 978-1-77188-298-9.

- [Li, Yueming et al. (July 2018)] Li, Yueming et al. (July 2018). «Deposition and Characterization of Phase-Pure Ti₂AlC and Ti₃AlC₂ Coatings by DC Magnetron Sputtering with Cost-Effective Targets». In: *Vacuum* 153, pp. 62–69. ISSN: 0042207X. DOI: 10.1016/j.vacuum.2018.04.001.
- [Link, Jarrett M. et al. (2019)] Link, Jarrett M. et al.— (2019). «The Tribology of Cartilage: Mechanisms, Experimental Techniques, and Relevance to Translational Tissue Engineering». In: *Clinical Biomechanics* December 2018. ISSN: 18791271. DOI: 10.1016/j.clinbiomech.2019.10.016.
- [Loganathan, Archana et al. (2018)] Loganathan, Archana et al.— (2018). «Multi-Scale Tribological and Nanomechanical Behavior of Cold Sprayed Ti₂AlC MAX Phase Coating». In: *Surface and Coatings Technology* 334. November 2017, pp. 384–393. ISSN: 02578972. DOI: 10.1016/j.surfcoat.2017.11.067.
- [Ma, Jiqiang et al. (2013)] Ma, Jiqiang et al.— (2013). «Tribological Behavior of Ti₃AlC₂ Against SiC at Ambient and Elevated Temperatures». In: *Tribology Letters* 50.3, pp. 323–330. ISSN: 10238883. DOI: 10.1007/s11249-013-0126-x.
- [Mang, Theo and Wilfried Dresel (2007)] Mang, Theo and Wilfried Dresel— (2007). *Lubricants and Lubrication*. Elsevier Ltd. ISBN: 978-3-527-31497-3. DOI: 10.1002/9783527610341.
- [Menezes, Pradeep L. et al., eds. (2013)] Menezes, Pradeep L. et al., eds.— eds. (2013). *Tribology for Scientists and Engineers: From Basics to Advanced Concepts*. New York: Springer. ISBN: 978-1-4614-1944-0.
- [Mihalko, William M. et al. (2020)] Mihalko, William M. et al.— (2020). «New Materials for Hip and Knee Joint Replacement: What’s Hip and What’s in Kneed?» In: *Journal of Orthopaedic Research* 38.7, pp. 1436–1444. ISSN: 1554-527X. DOI: 10.1002/jor.24750.
- [Mozafari, Masoud (2020)] Mozafari, Masoud— (2020). *Handbook of Biomaterials Biocompatibility*. Duxford: Woodhead Publishing. ISBN: 978-0-08-102968-8.

- [Myhra, S., J. W.B. Summers, and E. H. Kisi (1999)] Myhra, S., J. W.B. Summers, and E. H. Kisi (1999). «Ti₃SiC₂ - a Layered Ceramic Exhibiting Ultra-Low Friction». In: *Materials Letters* 39.1, pp. 6–11. ISSN: 0167577X. DOI: 10.1016/S0167-577X(98)00206-7.
- [Naeem, M. et al. (Aug. 2022)] Naeem, M. et al.— (Aug. 2022). «Wear and Corrosion Studies of Duplex Surface-Treated AISI-304 Steel by a Combination of Cathodic Cage Plasma Nitriding and PVD-TiN Coating». In: *Ceramics International* 48.15, pp. 21473–21482. ISSN: 0272-8842. DOI: 10.1016/j.ceramint.2022.04.115.
- [Naguib, Michael et al. (Oct. 2011)] Naguib, Michael et al.— (Oct. 2011). «Two-Dimensional Nanocrystals Produced by Exfoliation of Ti₃AlC₂.» In: *Advanced materials (Deerfield Beach, Fla.)* 23.37, pp. 4248–4253. ISSN: 1521-4095 (Electronic). DOI: 10.1002/adma.201102306.
- [Nowak, Paulina, Karolina Kucharska, and Marian Kamiński (Aug. 2019)] Nowak, Paulina, Karolina Kucharska, and Marian Kamiński— (Aug. 2019). «Ecological and Health Effects of Lubricant Oils Emitted into the Environment». In: *International journal of environmental research and public health* 16.16, p. 3002. ISSN: 1660-4601. DOI: 10.3390/ijerph16163002.
- [Pabinger, Christof et al. (Sept. 2018)] Pabinger, Christof et al.— (Sept. 2018). «Projections of Hip Arthroplasty in OECD Countries up to 2050». In: *HIP International* 28.5, pp. 498–506. ISSN: 1120-7000. DOI: 10.1177/1120700018757940.
- [Palomino, Lourdes et al. (Jan. 2016)] Palomino, Lourdes et al.— (Jan. 2016). «Fractura de Cadera En El Adulto Mayor: La Epidemia Ignorada En El Perú». In: *Acta Médica Peruana* 33.1, pp. 15–20. ISSN: 1728-5917.

- [Patnaik, Lokeswar, Saikat Ranjan Maity, and Sunil Kumar (Jan. 2021)] Patnaik, Lokeswar, Saikat Ranjan Maity, and Sunil Kumar (Jan. 2021). «DLC/CrN or AlCrN/CrN Composite Films: The Better Candidate in Terms of Anti-Wear Performance and Lesser Ion Release in Hip Implant». In: *Materials Today: Proceedings*. International Conference on Materials, Processing & Characterization 44, pp. 1214–1220. ISSN: 2214-7853. DOI: 10.1016/j.matpr.2020.11.242.
- [Paul, Subir and Chandranath Mandal (Oct. 2013)] Paul, Subir and Chandranath Mandal— (Oct. 2013). «Biocompatibly Coated 304 Stainless Steel as Superior Corrosion-Resistant Implant Material to 316L Steel». In: *J. of Materi Eng and Perform* 22.10, pp. 3147–3154. ISSN: 1059-9495, 1544-1024. DOI: 10.1007/s11665-013-0590-3.
- [Platon, F, P Fournier, and S Rouxel (2001)] Platon, F, P Fournier, and S Rouxel— (2001). «Tribological Behaviour of DLC Coatings Compared to Different Materials Used in Hip Joint Prostheses». In: *Wear* 250.1, pp. 227–236. ISSN: 0043-1648. DOI: 10.1016/S0043-1648(01)00651-2.
- [Presser, Volker et al. (Jan. 2012)] Presser, Volker et al.— (Jan. 2012). «First-Order Raman Scattering of the MAX Phases: Ti_2AlN , $Ti_2AlC_{0.5}N_{0.5}$, Ti_2AlC , $(Ti_{0.5}V_{0.5})_2AlC$, V_2AlC , Ti_3AlC_2 , and Ti_3GeC_2 : First-order Raman Scattering of Selected 312 and 211 MAX Phases». In: *J. Raman Spectrosc.* 43.1, pp. 168–172. ISSN: 03770486. DOI: 10.1002/jrs.3036.
- [Pruitt, Lisa A. and Ayyana M. Chakravartula (2011)] Pruitt, Lisa A. and Ayyana M. Chakravartula— (2011). *Mechanics of Biomaterials: Fundamental Principles for Implant Design*. Cambridge Texts in Biomedical Engineering. Cambridge ; New York: Cambridge University Press. ISBN: 978-0-521-76221-2.
- [Qin, Wenbo et al. (Sept. 2018)] Qin, Wenbo et al.— (Sept. 2018). «Tribological Behavior of the 316L Stainless Steel with Heterogeneous Lamella Structure». In: *Materials* 11.10, p. 1839. ISSN: 1996-1944. DOI: 10.3390/ma11101839.

- [Quan, Cheng and Yedong He (May 2015)] Quan, Cheng and Yedong He (May 2015). «Properties of Nanocrystalline Cr Coatings Prepared by Cathode Plasma Electrolytic Deposition from Trivalent Chromium Electrolyte». In: *Surface and Coatings Technology*. Special Issue on Plasma Electrolysis: Progress in Science, Technology and Applications of Electrolytic Plasma Surface Treatments and Coatings 269, pp. 319–323. ISSN: 0257-8972. DOI: 10.1016/j.surfcoat.2015.02.001.
- [Quispe, Roger et al. (June 2022)] Quispe, Roger et al.— (June 2022). «Tribological and Mechanical Performance of Ti₂AlC and Ti₃AlC₂ Thin Films». In: *Adv Eng Mater*, p. 2200188. ISSN: 1438-1656, 1527-2648. DOI: 10.1002/adem.202200188.
- [El-Raghy, Tamer, Peter Blau, and Michel W Barsoum (2000)] El-Raghy, Tamer, Peter Blau, and Michel W Barsoum— (2000). «Effect of Grain Size on Friction and Wear Behavior of Ti₃SiC₂». In: *Wear* 238.2, pp. 125–130. ISSN: 0043-1648. DOI: 10.1016/S0043-1648(99)00348-8.
- [Rao, Rahul, Neal Pierce, and Archi Dasgupta (Aug. 2014)] Rao, Rahul, Neal Pierce, and Archi Dasgupta— (Aug. 2014). «On the Charge Transfer between Single-Walled Carbon Nanotubes and Graphene». In: *Applied Physics Letters* 105. DOI: 10.1063/1.4893698.
- [Ratner, B. D., ed. (2013)] Ratner, B. D., ed.— ed. (2013). *Biomaterials Science: An Introduction to Materials in Medicine*. 3rd ed. Amsterdam ; Boston: Elsevier/Academic Press. ISBN: 978-0-12-374626-9.
- [Ren, Shufang et al. (2010)] Ren, Shufang et al.— (2010). «Tribocorrosion Behavior of Ti₃SiC₂ in the Dilute and Concentrated Sulfuric Acid Solutions». In: *Wear* 269.1-2, pp. 50–59. ISSN: 00431648. DOI: 10.1016/j.wear.2010.03.007.
- [Revell, Peter (2021)] Revell, Peter— (2021). *Joint Replacement Technology*. 3rd. Woodhead Publishing Series in Biomaterials. S.I.: WOODHEAD PUBLISHING UK. ISBN: 978-0-12-821082-6.

- [Roy, M. (2017)] Roy, M. Roy, M. (2017). *Protective Hard Coatings for Tribological Applications*. Elsevier Inc. ISBN: 978-0-12-801442-4. DOI: 10.1016/B978-0-12-801300-7.00008-5.
- [Royhman, Dmitry et al. (Sept. 2016)] Royhman, Dmitry et al.— (Sept. 2016). «Fretting-Corrosion Behavior in Hip Implant Modular Junctions: The Influence of Friction Energy and pH Variation». In: *Journal of the Mechanical Behavior of Biomedical Materials* 62, pp. 570–587. ISSN: 17516161. DOI: 10.1016/j.jmbbm.2016.05.024.
- [Ruggiero, Alessandro, Roberto D’Amato, and Emilio Gómez (Dec. 2015)] Ruggiero, Alessandro, Roberto D’Amato, and Emilio Gómez— (Dec. 2015). «Experimental Analysis of Tribological Behavior of UHMWPE against AISI420C and against TiAl6V4 Alloy under Dry and Lubricated Conditions». In: *Tribology International* 92, pp. 154–161. ISSN: 0301-679X. DOI: 10.1016/j.triboint.2015.06.005.
- [Ruggiero, Alessandro, Roberto D’Amato, Emilio Gómez, and Massimiliano Merola (Apr. 2016)] Ruggiero, Alessandro, Roberto D’Amato, Emilio Gómez, and Massimiliano Merola— (Apr. 2016). «Experimental Comparison on Tribological Pairs UHMWPE/TiAl6V4 Alloy, UHMWPE/AISI316L Austenitic Stainless and UHMWPE/AL2O3 Ceramic, under Dry and Lubricated Conditions». In: *Tribology International* 96, pp. 349–360. ISSN: 0301-679X. DOI: 10.1016/j.triboint.2015.12.041.
- [Ruggiero, Alessandro and Alessandro Sicilia (Feb. 2020)] Ruggiero, Alessandro and Alessandro Sicilia— (Feb. 2020). «Lubrication Modeling and Wear Calculation in Artificial Hip Joint during the Gait». In: *Tribology International* 142, p. 105993. ISSN: 0301679X. DOI: 10.1016/j.triboint.2019.105993.
- [Sanati, Alireza, Keyvan Raeissi, and Hossein Edris (Sept. 2017)] Sanati, Alireza, Keyvan Raeissi, and Hossein Edris— (Sept. 2017). «Investigation of the Corrosion Behavior of Cathodic Arc Evaporated Stainless Steel Coating in 3.5% NaCl». In: *Prot Met Phys Chem Surf* 53.5, pp. 902–909. ISSN: 2070-206X. DOI: 10.1134/S2070205117050197.

- [Sanders, Anthony P. and Rebecca M. Brannon (Nov. 2011)] Sanders, Anthony P. and Rebecca M. Brannon (Nov. 2011). «Assessment of the Applicability of the Hertzian Contact Theory to Edge-Loaded Prosthetic Hip Bearings». In: *Journal of Biomechanics* 44.16, pp. 2802–2808. ISSN: 00219290. DOI: 10.1016/j.jbiomech.2011.08.007.
- [Sarkar, D. et al. (2005)] Sarkar, D. et al.— (2005). «Tribological Properties of Ti 3SiC 2». In: *Journal of the American Ceramic Society* 88.11, pp. 3245–3248. ISSN: 00027820. DOI: 10.1111/j.1551-2916.2005.00569.x.
- [Scharf, T. W. and S. V. Prasad (2013)] Scharf, T. W. and S. V. Prasad— (2013). «Solid Lubricants: A Review». In: *Journal of Materials Science* 48.2, pp. 511–531. ISSN: 00222461. DOI: 10.1007/s10853-012-7038-2.
- [Scholes, S. C. and A. Unsworth (Jan. 2009)] Scholes, S. C. and A. Unsworth— (Jan. 2009). «Wear Studies on the Likely Performance of CFR-PEEK/CoCrMo for Use as Artificial Joint Bearing Materials». In: *J Mater Sci: Mater Med* 20.1, pp. 163–170. ISSN: 0957-4530, 1573-4838. DOI: 10.1007/s10856-008-3558-3.
- [Seyfert, Christian (2014)] Seyfert, Christian— (2014). «Tribometers, Rotational, for Sliding Wear and Friction». In: *Encyclopedia of Lubricants and Lubrication*. Ed. by Theo Mang. Berlin, Heidelberg: Springer Berlin Heidelberg, pp. 2138–2155. ISBN: 978-3-642-22646-5 978-3-642-22647-2. DOI: 10.1007/978-3-642-22647-2_144.
- [Shen, Gang, Fengzhou Fang, and Chengwei Kang (June 2018)] Shen, Gang, Fengzhou Fang, and Chengwei Kang— (June 2018). «Tribological Performance of Bioimplants: A Comprehensive Review». In: *Nanotechnology and Precision Engineering* 1.2, pp. 107–122. ISSN: 2589-5540. DOI: 10.13494/j.npe.20180003.

- [Sin, J. Rituerto, X. Hu, and N. Emami (Mar. 2013)] Sin, J. Rituerto, X. Hu, and N. Emami (Mar. 2013). «Tribology, Corrosion and Tribocorrosion of Metal on Metal Implants». In: *Tribology - Materials, Surfaces & Interfaces* 7.1, pp. 1–12. ISSN: 1751-5831. DOI: 10.1179/1751584X13Y.0000000022.
- [Smirnov, A. et al. (Feb. 2018)] Smirnov, A. et al.— (Feb. 2018). «Tribological Behaviour of a 3Y-TZP/Ta Ceramic-Metal Biocomposite against Ultrahigh Molecular Weight Polyethylene (UHMWPE)». In: *Ceramics International* 44.2, pp. 1404–1410. ISSN: 0272-8842. DOI: 10.1016/j.ceramint.2017.09.186.
- [Souchet, Alexandra et al. (2005)] Souchet, Alexandra et al.— (2005). «Tribological Duality of Ti₃SiC₂». In: *Tribology Letters* 18.3, pp. 341–352. ISSN: 1573-2711. DOI: 10.1007/s11249-004-2761-8.
- [Spanier, Jonathan E. et al. (Jan. 2005)] Spanier, Jonathan E. et al.— (Jan. 2005). «Vibrational Behavior of the $M_{n+1}A_nX_n$ Phases from First-Order Raman Scattering ($M = Ti, V, Cr, A = Si, X = C, N$)». In: *Phys. Rev. B* 71.1, p. 012103. ISSN: 1098-0121, 1550-235X. DOI: 10.1103/PhysRevB.71.012103.
- [Stavlid, Nils (Oct. 2020)] Stavlid, Nils— (Oct. 2020). «On the Formation of Low-Friction Tribofilms in Me-DLC – Steel Sliding Contacts». In.
- [Swaminathan, Viswanathan and Jeremy L. Gilbert (Aug. 2012)] Swaminathan, Viswanathan and Jeremy L. Gilbert— (Aug. 2012). «Fretting Corrosion of CoCrMo and Ti6Al4V Interfaces». In: *Biomaterials* 33.22, pp. 5487–5503. ISSN: 01429612. DOI: 10.1016/j.biomaterials.2012.04.015.
- [Tang, Yee-Chin et al. (Nov. 2006)] Tang, Yee-Chin et al.— (Nov. 2006). «Electrochemical Study of Type 304 and 316L Stainless Steels in Simulated Body Fluids and Cell Cultures». In: *Acta Biomaterialia* 2.6, pp. 709–715. ISSN: 17427061. DOI: 10.1016/j.actbio.2006.06.003.

- [Torres, Carlos et al. (Jan. 2021)] Torres, Carlos et al. Torres, Carlos et al. (Jan. 2021). «Development of the Phase Composition and the Properties of Ti₂AlC and Ti₃AlC₂ MAX-phase Thin Films – A Multilayer Approach towards High Phase Purity». In: *Applied Surface Science* 537, p. 147864. ISSN: 01694332. DOI: 10.1016/j.apsusc.2020.147864.
- [Tribology Laboratory at Lehigh University: (Oct. 2012)] Tribology Laboratory at Lehigh University: (Oct. 2012). <https://www.lehigh.edu/~intribos/tribology.html>.
- [Vakis, A. I. et al. (2018)] Vakis, A. I. et al.— (2018). «Modeling and Simulation in Tribology across Scales: An Overview». In: *Tribology International* 125, pp. 169–199. ISSN: 0301679X. DOI: 10.1016/j.triboint.2018.02.005.
- [Vandenabeele, Peter (2013)] Vandenabeele, Peter— (2013). *Practical Raman Spectroscopy: An Introduction*. The Atrium, Southern Gate, Chichester, West Sussex, United Kingdom: Wiley. ISBN: 978-0-470-68319-4 978-0-470-68318-7.
- [Vento, Renee (2016)] Vento, Renee— (2016). «Factores pronósticos asociados a mala evolución en pacientes mayores de 65 años internados por fractura de cadera en el Hospital Central de la Fuerza Aérea». PhD thesis. Lima: Universidad Ricardo Palma.
- [Virtanen, Sannakaisa (2012)] Virtanen, Sannakaisa— (2012). «Degradation of Titanium and Its Alloys». In: *Degradation of Implant Materials*. Ed. by Noam Eliaz. New York, NY: Springer New York, pp. 29–55. ISBN: 978-1-4614-3941-7 978-1-4614-3942-4. DOI: 10.1007/978-1-4614-3942-4_2.
- [Volkman, R. (Aug. 2009)] Volkman, R.— (Aug. 2009). «Implantatrevisionen am Hüftgelenk: Fehlervermeidung und Risikomanagement». In: *Orthopäde* 38.8, pp. 718–728. ISSN: 0085-4530, 1433-0431. DOI: 10.1007/s00132-009-1427-5.

- [Wadhwa, Anmol, Sushama Talegaonkar, and Harvinder Popli (Nov. 2019)] Wadhwa, Anmol, Sushama Talegaonkar, and Harvinder Popli (Nov. 2019). «A Regulatory Overview of Hip And Knee Joint Replacement Devices». In: *ACCTRA* 6.3, pp. 212–230. ISSN: 2213476X. DOI: 10.2174/2213476X06666190823142403.
- [Wang, Lixia and Juncai Sun (Mar. 2013)] Wang, Lixia and Juncai Sun— (Mar. 2013). «Molybdenum Modified AISI 304 Stainless Steel Bipolar Plate for Proton Exchange Membrane Fuel Cell». In: *Journal of Renewable and Sustainable Energy* 5.2, p. 021407. DOI: 10.1063/1.4798437.
- [Wang, Shuai et al. (2016)] Wang, Shuai et al.— (2016). «Frictional Properties of Ti3AlC2 Ceramic against Different Counterparts in Deionized Water and Artificial Seawater». In: *Ceramics International* 42.3, pp. 4578–4585. ISSN: 02728842. DOI: 10.1016/j.ceramint.2015.11.153.
- [Wang, Xishi et al. (June 2005)] Wang, Xishi et al.— (June 2005). «THE HIP STRESS LEVEL ANALYSIS FOR HUMAN ROUTINE ACTIVITIES». In: *Biomed. Eng. Appl. Basis Commun.* 17.03, pp. 153–158. ISSN: 1016-2372, 1793-7132. DOI: 10.4015/S101623720500024X.
- [Wang, Yansong and Q Jane Wang (2013)] Wang, Yansong and Q Jane Wang— (2013). «Stribeck Curves». In: *Encyclopedia of Tribology*. Ed. by Q Jane Wang and Yip-Wah Chung. Boston, MA: Springer US, pp. 3365–3370. ISBN: 978-0-387-92897-5. DOI: 10.1007/978-0-387-92897-5_148.
- [Wäsche, Rolf and Mathias Woydt (2014)] Wäsche, Rolf and Mathias Woydt— (2014). «Stribeck Curve BT - Encyclopedia of Lubricants and Lubrication». In: ed. by Theo Mang. Berlin, Heidelberg: Springer Berlin Heidelberg, pp. 1998–2005. ISBN: 978-3-642-22647-2. DOI: 10.1007/978-3-642-22647-2_274.
- [Wood, R. J.K. (2006)] Wood, R. J.K.— (2006). *Understanding Surface Wear in Engineering Materials*. Woodhead Publishing Limited. ISBN: 978-1-85573-767-9. DOI: 10.1533/9781845691561.1.

- [Wu, Ling et al. (2009)] Wu, Ling et al. (2009). «Reciprocating Friction and Wear Behavior of Ti₃AlC₂ and Ti₃AlC₂/Al₂O₃ Composites against AISI52100 Bearing Steel». In: *Wear* 266.1-2, pp. 158–166. ISSN: 00431648. DOI: 10.1016/j.wear.2008.06.009.
- [Xu, Zengshi et al. (2015)] Xu, Zengshi et al.— (2015). «Sliding Speed and Load Dependence of Tribological Properties of Ti₃SiC₂/TiAl Composite». In: *Tribology Transactions* 58.1, pp. 87–96. ISSN: 1547397X. DOI: 10.1080/10402004.2014.951748.
- [Zanabria, Jorge Chávez (2020)] Zanabria, Jorge Chávez— (2020). «TRATAMIENTO REHABILITADOR PRECOZ EN PACIENTES POSOPERADOS DE ARTROPLASTIA TOTAL DE CADERA HOSPITAL NACIONAL LUIS NICASIO SÁENZ POLICÍA NACIONAL DEL PERÚ 2015-2016». PhD thesis. Lima: Universidad San Martín de Porres.
- [Zandrahimi, Morteza et al. (Sept. 2007)] Zandrahimi, Morteza et al.— (Sept. 2007). «The Formation of Martensite during Wear of AISI 304 Stainless Steel». In: *Wear*. 16th International Conference on Wear of Materials 263.1, pp. 674–678. ISSN: 0043-1648. DOI: 10.1016/j.wear.2007.01.107.
- [Zardiackas, Lyle D. (Apr. 2006)] Zardiackas, Lyle D.— (Apr. 2006). «Stainless Steels for Implants». In: *Wiley Encyclopedia of Biomedical Engineering*. Ed. by Metin Akay. Hoboken, NJ, USA: John Wiley & Sons, Inc., ebs1136. ISBN: 978-0-471-74036-0. DOI: 10.1002/9780471740360.ebs1136.
- [Zhou, Z.R. and Z.M. Jin (2015)] Zhou, Z.R. and Z.M. Jin— (2015). «Biotribology: Recent Progresses and Future Perspectives». In: *Biosurface and Biotribology* 1.1, pp. 3–24. ISSN: 24054518. DOI: 10.1016/j.bsbt.2015.03.001.